Measurement of the Charge Asymmetry and the W Boson Helicity in Top- Antitop Quark Events with the CDF II Experiment

Dominic Hirschbühl

Zur Erlangung des akademischen Grades eines
DOKTORS DER NATURWISSENSCHAFTEN
von der Fakultät für Physik der
Universität Karlsruhe(TH)

genehmigte

Dissertation

von

Dipl.-Phys. Dominic Hirschbühl
aus Neuenbürg

Tag der mündlichen Prüfung: 23.12.2005

Referent: Prof. Dr. Th. Müller, Institut für Experimentelle Kernphysik

Korreferent: Prof. Dr. G. Quast, Institut für Experimentelle Kernphysik

Preface

In 1995 the heaviest elementary particle, top quark, was discovered at the Tevatron collider in top-antitop quark pair production [1, 2]. Since the top quark mass is of the same order as the electroweak symmetry breaking scale, measurements of the properties of the top quark like mass, charge, spin or the production mechanism, offer a good opportunity to test the Standard Model at such high energies.

Top quarks at the Tevatron are predominantly pair-produced through light quark-antiquark annihilation. Higher order perturbative QCD calculations predict a sizeable asymmetry between the number of top quarks and antitop quarks produced in forward direction. This asymmetry is induced through radiative corrections. A measurement of the asymmetry can check the perturbative QCD predictions.

Due to the high mass of the top quark, nearly the mass of a gold nucleus, the life time of the top quark is much shorter than the hadronization time-scale. This means that the top quark decays before it has a chance to form a bound state. The Standard Model predicts that the top quark decays in nearly 100% of the cases into a W boson and a b quark via a charge-current weak interaction. The measurement of the W boson helicity probes the V-A structure of the weak interaction and differences to the expectation would give evidence for new physics.

Until the start of the Large Hadron Collider at CERN, the Tevatron is the only experiment where top quarks can be directly produced and their properties be measured. The Tevatron reaches a center-of-mass energy of 1.96 TeV in proton antiproton collisions. The data used in this analysis were taken in Run II of the Tevatron with the Collider Detector at Fermilab (CDF) in the years 2001 - 2004 and represent an integrated luminosity of 319 pb^{-1}.

The thesis is organized in the following way:
In the first chapter a short overview of the Standard Model is given. The theoretical aspects of the top quark decay are described with particular emphasis on the different helicities of the W boson. The second focus lies on the production

process and the higher order QCD effect causing the charge asymmetry.

In the following three chapters the experimental techniques of the CDF detector, hardware and the used software are introduced as well as.

In this thesis $t\bar{t}$ candidates are selected in the decay mode $t \to bl\nu$, $\bar{t} \to bjj$ and the charge conjugated state. An important ingredient for this measurement is the complete reconstruction of the top-antitop partonic process. The reconstruction of the partonic process requires the assignment of reconstructed objects, such as jets, the charged lepton and the missing transverse energy to parton level objects. This assignment implies a certain number of possible permutations and ambiguities. To achieve the optimal reconstruction of the event all combinations have to be considered and evaluated. To measure a $t\bar{t}$-quantity one hypothesis has to be chosen. In chapter five we present a novel technique to fully reconstruct $t\bar{t}$ events. The technique is investigated in great detail by comparing to the Monte Carlo truth information.

In the sixth chapter the background estimation is given. The identification and selection procedure on data is checked with Monte Carlo samples.

Chapter seven describes the measurement of the W boson helicity in the top quark decay. The helicity of the W boson is measured via the angle between the W boson momentum in the top quark rest frame and the lepton momentum in the W boson rest frame. After correcting for acceptance and reconstruction effects the different helicity fractions are extracted by fitting the theoretical expected distribution. The systematic error is determined using the technique of pseudo experiments.

In chapter eight the measurement of the charge asymmetry in top-pair production is presented. The measurement of the asymmetry is performed by using the difference of the top quark rapidities times the charge of the lepton, to distinguish between top and anti-top quarks.

The results and an outlook are given in the last chapter.

Contents

List of Figures

List of Tables

Chapter 1

Theory

In this chapter a brief introduction of the theoretical framework of particle physics - the Standard Model - is given. We will introduce the production mechanism and the decay of the heaviest elementary particle known, the top quark. The theoretical basis of our measurement of the charge asymmetry in top - anti-top quark production and of the W boson helicity in the decay of the top quark is also described.

1.1 The Standard Model

The Standard Model of Elementary Particle Physics describes the fundamental particles of matter and their interactions. The Standard Model provides a very elegant theoretical framework [3]. All matter in the Standard Model is composed of particles with spin $\frac{1}{2}$, called fermions, the leptons and quarks. All interactions between the fermions are mediated by spin 1 particles known as gauge bosons. Up to now there are six different quark flavors known, up (u), down (d), strange (s), charm (c), bottom (b) and top (t) quark. Quantum numbers like the electric charge q or the spin s are used to describe elementary particles. Since quarks partake in both the electroweak and the strong interaction they have an additional quantum number, the color, which can be of three types. Since color is not seen detectors, the quarks must be confined into colorless particles, which are classified into baryons and mesons. The baryons are made up of three quarks, as for instance the proton, $p = uud$. The mesons are made of a quark-antiquark pair like pions, $\pi^+ = u\bar{d}$. There are also six particles which do not have strong interaction, the leptons, and hence do not carry color charge. These are the electron, the muon and the tau and the corresponding neutral neutrinos.
All fundamental particles are ordered in families or generations. The masses of the quarks and leptons are not predicted by the standard model. For each particle, there exists an antiparticle of opposite charge but identical mass, lifetime and spin. Table 1.1 shows the three generations of fundamental particles and

Name	Symbol	El. charge(e)	Mass
Down quark	d	$-\frac{1}{3}$	$4-8$ MeV/c^2
Up quark	u	$+\frac{2}{3}$	$1.5-4$ MeV/c^2
Electron	e	-1	511 keV/c^2
Electron neutrino	ν_e	0	<3 eV/c^2
Strange quark	s	$-\frac{1}{3}$	$80-130$ MeV/c^2
Charm quark	c	$+\frac{2}{3}$	$1.15-1.35$ GeV/c^2
Muon	μ	-1	106 MeV/c^2
Muon neutrino	ν_μ	0	<190 keV/c^2
Bottom quark	b	$-\frac{1}{3}$	$4.1-4.4$ GeV/c^2
Top quark	t	$+\frac{2}{3}$	174.3 ± 5.1 GeV/c^2
Tau	τ	-1	1.777 GeV/c^2
Tau neutrino	ν_τ	0	<18.2 MeV/c^2

Table 1.1: The fundamental spin-$\frac{1}{2}$ particles. The electric charge is in units of the positron charge. The masses are not predicted by the standard model, the values shown here reflect measurements made by experiment. [4]

their masses.

Three of the four fundamental forces, the electromagnetic force, the weak force and the strong force are described by the Standard Model. Gravitation is described by the Theory of General Relativity. The forces described by the Standard Model are transmitted by specific particles. As the theories of the forces are gauge theories, the transmitting particles are called gauge bosons.
The Standard Model contains two quantum field theories. The electroweak (EW) and quantum chromodynamic (QCD) field theories govern the electroweak and strong interactions, respectively. Table 1.2 summarizes the properties of the gauge bosons for each force. In a gauge theory the Lagrange function that describes a physical system is invariant under gauge transformations. According to the Noether theorem[5] such an invariance implies a conserved current, to which the charges of the forces correspond. Just as in quantum electrodynamics (QED), where the gauge symmetry of the theory implies the existence of a massless photon (γ), the $SU(2)\times U(1)$ and $SU(3)$ gauge symmetries of EW and QCD lead to the presence of the $\gamma, W^{\pm}, Z$, and g gauge bosons in the Standard Model. The masses of the quarks and the gauge bosons can not be explained with the Lagrangian of the electroweak theory. As the gauge fields have to be invariant under local or global transformations, the local gauge invariance forces the gauge bosons to be massless. Any mass term in the Lagrangian would destroy the local gauge invariance. The solution for this dilemma is to introduce

Force	Boson name	Symbol	Charge(e)	Spin	Mass (GeV/c^2)
Strong	gluon	g	0	1	0
Electromagnetic	photon	γ	0	1	0
Weak (charged)	W boson	$W^{\pm}$	± 1	1	80.425 ± 0.038
Weak (neutral)	Z boson	Z^0	0	1	91.1876 ± 0.0021

Table 1.2: Properties of the gauge bosons. The electric charge is in units of the electron charge, the mass is in units of GeV/c^2 [4].

an additional scalar field, the Higgs-field [6]. With this method the Lagrangian remains invariant under gauge transformations, but the ground state is interacting with this background field. The masses of the three massive gauge boson $W^{\pm}, Z$ are acquired through this Higgs mechanism, whereby the massless scalar and vector fields of the Lagrangian are spontaneously broken. In this theory the massive scalar η is know as the "Higgs boson". The fermions also get their masses also by the Higgs-field, the coupling is called Yukawa-coupling.

1.2 The Top Quark

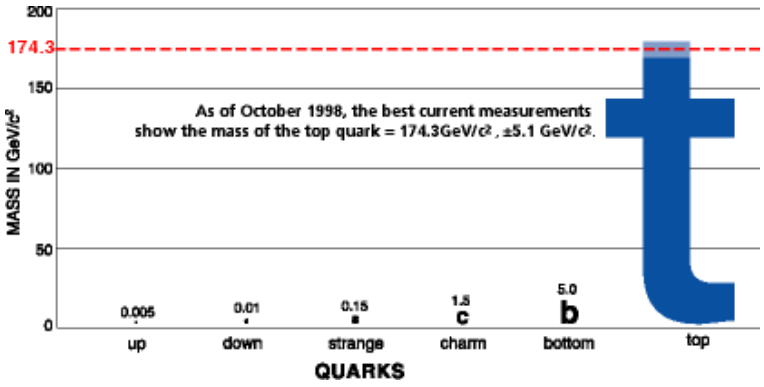

Figure 1.1: Masses of the different quarks.

The discovery of the top quark by the CDF [1] and the DØ [2] collaboration in 1995 revealed that this was the so far heaviest known elementary particle. Weighing about ~ 175 GeV/c^2, nearly the mass of a gold nucleus and almost 40 times the mass of the next heaviest quark, see figure 1.1, it is close to the scale of the electroweak symmetry breaking in the Standard Model. As mentioned before, the Higgs mechanism is responsible for the top quark mass, and according to the Standard Model theory top's Yukawa coupling, g_{ttH}, is ~ 1.

$$g_{ttH} = \frac{\sqrt{2}m_t}{v} = \frac{\sqrt{2}m_t}{246\ \text{GeV}} \sim 1, \tag{1.1}$$

where v denotes the vacuum expectation value of the Higgs potential. Therefore precise measurements of the top quark properties and comparison to Standard Model expectations are important for understanding the electroweak symmetry breaking and can be a probe for new physics.
At the Tevatron, top quarks are most often produced in $t\bar{t}$ pairs via the strong interaction. Approximately 85% of the total $t\bar{t}$ production cross section at the Tevatron stems from quark-antiquark annihilation, the remaining fraction is from gluon-gluon fusion. The leading order Feynman diagrams of the relevant graphs are shown in figure 1.2. The current theoretical calculation of the $t\bar{t}$ production cross section at center of mass energy of $\sqrt{s} = 1.96$ GeV, with a top quark mass of 175 GeV/c^2, is approximately 6.7 ± 0.9 pb [7].

1.2.1 Charge asymmetry in $t\bar{t}$-production

It has been shown, that the top quarks produced through light quark - anti-quark annihilation will exhibit a sizeable charge asymmetry induced through radiative corrections involving either virtual or real gluon emission. This leads to a difference between the differential $t\bar{t}$ production processes which could be

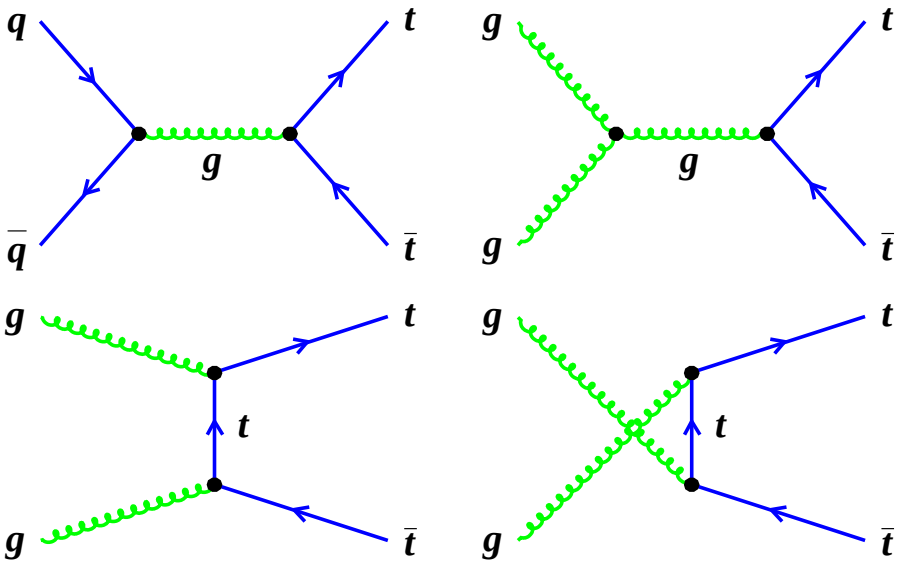

Figure 1.2: Leading order Feynman diagrams of top-anti-top pair productions at the Tevatron. The most important production process is through quark-antiquark annihilation.

accessible experimentally [8].
This asymmetry has its origin in two different production processes: radiative corrections to quark-antiquark-fusion, see figure 1.3, and heavy flavor production involving interference terms of different amplitudes contributing to gluon-quark scattering ($g + q \rightarrow t + \bar{t} + q$). At the Tevatron gluon-quark scattering can be neglected, therefore we only consider radiative corrections. We have to consider terms of order α_s^3 as leading order terms are of order α_s^2 where no asymmetry can be seen. The asymmetry between the charge-conjugated states can be explained by considering the C-parity states of the incoming and the outgoing partons. The same effect is well known in QED [9]. We know that the intrinsic C-parity of the gluon is -1, therefore we can state that for the Born diagram the incoming as well as the outgoing partons have to have even parity. If we radiate a gluon in the final state we change the sign for the parity for the corresponding state. We can consider the same arguments for the box diagram, figure 1.3c). As both gluons have odd C-parity both the initial and final state have to have even C-parity. As mentioned before the asymmetry can be explained by the interference of these diagrams. We can define the asymmetry A as the difference of the cross-section σ between the charged conjugated processes divided by the sum:

$$A = \frac{\sigma(q\bar{q} \rightarrow t\bar{t}) - \sigma(\bar{q}q \rightarrow \bar{t}t)}{\sigma(q\bar{q} \rightarrow t\bar{t}) + \sigma(\bar{q}q \rightarrow \bar{t}t)} \tag{1.2}$$

We have to consider two parts. On the one hand the interference between the initial (f_{isr}) and final state radiation (f_{fsr}), on the other hand the interference between the box (f_{box}) and the Born diagram (f_{born}). We can then express the

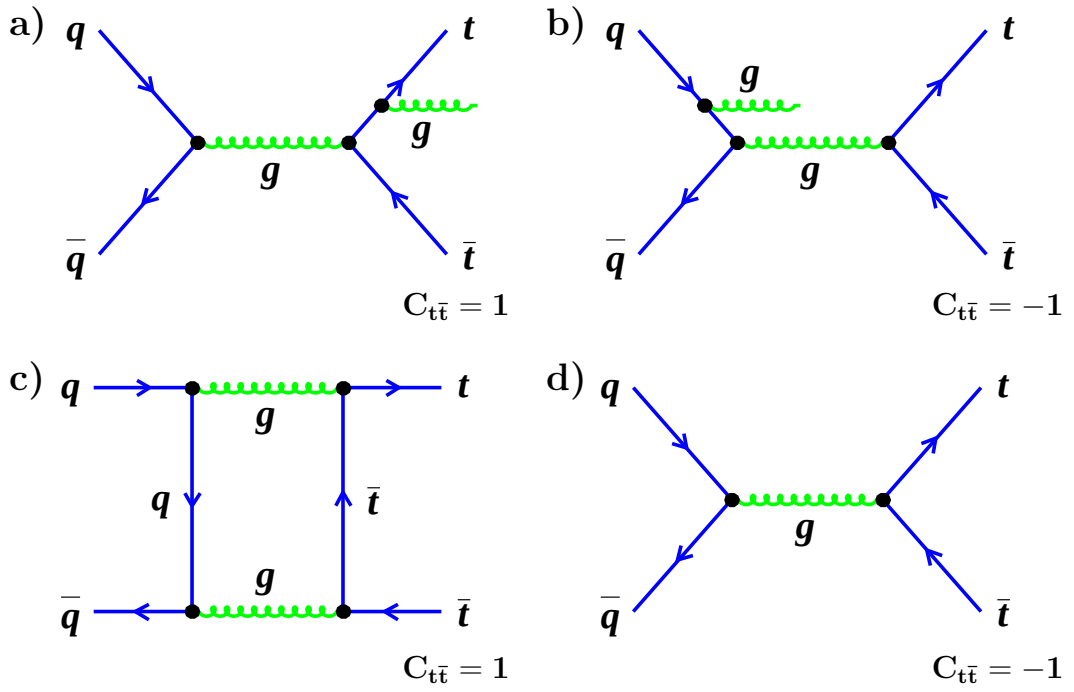

Figure 1.3: Origin of the QCD charge asymmetry in hadroproduction of heavy quarks: interference of final state (a) with initial state (b) gluon bremsstrahlung plus interference of the box (c) with the Born diagram (d). $C_{t\bar{t}}$ indicates the C-parity of the $t\bar{t}$ state. Only representative diagrams are shown.

calculation of the cross section as follows. We only consider diagrams up to the order of α_s^3.

$$\sigma \sim f_{born}^2 + f_{box} \cdot f_{born} + f_{isr} \cdot f_{fsr} + f_{isr}^2 + f_{fsr}^2$$

If we consider the charged conjugated process the interference terms change their sign, since the parity is a multiplicative quantum number (C(interference term) = $1 \cdot (-1) = -1$). Then we can give the asymmetry calculation as:

$$A = \frac{2(f_{box} \cdot f_{born} + f_{isr} \cdot f_{fsr})}{|f_{born}^2| + |f_{isr}^2| + |f_{fsr}^2|} \tag{1.3}$$

The asymmetry can be calculated either in the partonic center of mass system or in the proton - anti-proton rest frame by folding the angular distributions with the structure functions. The theoretically calculated asymmetry for both quantities are given in figure 1.4. The integrated forward-backward asymmetry measured in the lab frame is given by equation 1.4, where $N_t, N_{\bar{t}}$ denote the number of top and anti-top quarks, respectively, and α denotes the scattering angle.

$$A = \frac{N_t(\cos\alpha \geq 0) - N_{\bar{t}}(\cos\alpha \geq 0)}{N_t(\cos\alpha \geq 0) + N_{\bar{t}}(\cos\alpha \geq 0)} \tag{1.4}$$

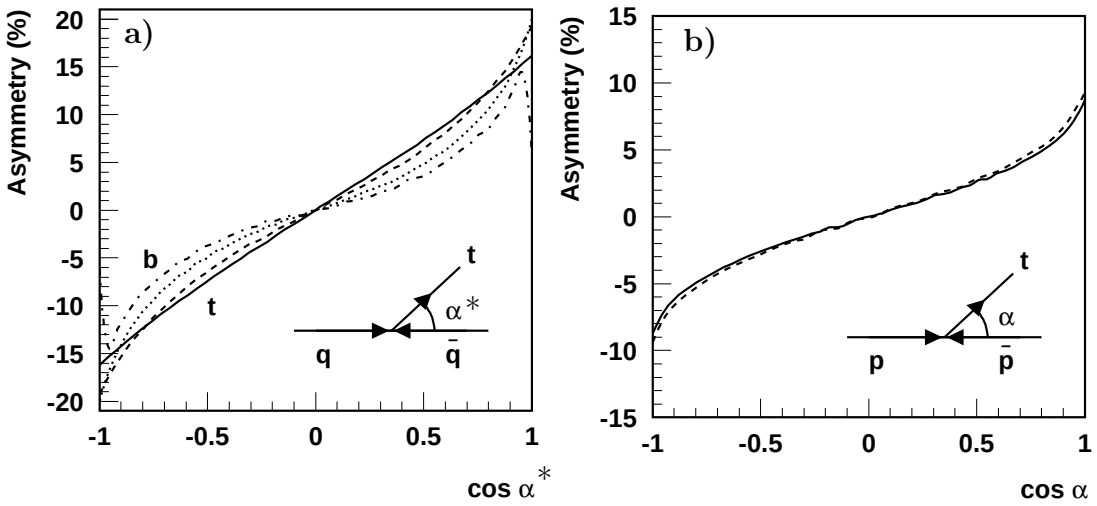

Figure 1.4: a) Differential charge asymmetry in top quark pair production for fixed partonic center of mass energy $\sqrt{\hat{s}} = 400$ GeV (solid), 600 GeV (dashed) and 1 TeV (dotted). Typical values of $\sqrt{\hat{s}}$ are between 400 GeV and 800 GeV for the Tevatron. b) In the proton - anti-proton rest frame.

A is assumed to be 4-5 % at the Tevatron with $\sqrt{s} = 1.96$ GeV.

1.2.2 The Decay of Top Quarks

The top quark has a lifetime of about 0.4×10^{-24}s, much shorter than any other quark. In fact, the top quark's lifetime is less than the QCD hadronization time-scale, which means that it decays before it has a chance to hadronize. Since the top quark does not hadronize, studying the top quark is about as close as one can get to studying a bare quark. Unlike in the decays of lighter quarks, where the quark spin information is lost during hadronization, the top quark spin is passed directly to its decay products in a manner which is explicitly understood [10].
The top quark decays predominantly via charged-current weak interaction $t \to W^+b$, $\bar{t} \to W^-\bar{b}$, see figure 1.5. There are several other possible decays of the top quark, but they are exceptionally rare. The charged-current weak decays $t \to W^+d$ and $t \to W^+s$ are suppressed due to the small values of the Cabibbo-Kobayashi-Maskawa (CKM) matrix[11] elements $|V_{td}|$ and $|V_{ts}|$. Additional flavor-changing neutral-current modes are very rare in the Standard Model. Since the top quark is heavier than the combined masses of the W boson and the b quark, it will decay into a real W boson, whereas lighter quarks will decay into a virtual W boson. Because the top quark is so heavy, and the other quarks are so light, top decay is the only significant source of longitudinal W bosons. The reason for this is given by the gauge theory.
W bosons decay into a lepton-neutrino pair, or into a quark - anti-quark pair.

The branching ratios of a W boson into the various lepton-neutrino or quark - anti-quark pairs is shown in table 1.3. $t\bar{t}$ events can be categorized based on the way in which the two W bosons in the event will decay. These are: dilepton, in which both W bosons decay into a lepton-neutrino pair, all-jets (hadronic), in which both W's decay into a quark - anti-quark pair, and lepton+jets, when one W decays into a lepton neutrino pair and the other W boson decays into a quark - anti-quark pair. We will focus in this thesis on the lepton+jets channel. The advantages of this channel are that the branching fraction is higher than the fraction of di-lepton events and of the same value compared to the hadronic channel combinations, see table 1.4. In the di-lepton channel the combinatorics would be smaller than for the other channels but one would have to deal with two produced neutrinos which can only be measured as missing energy in the CDF detector. In the hadronic channel six jets have to be reconstructed and combined to two top quarks, so the combinatorics and the difficulties with the jet reconstruction makes this channel difficult to analyze. As a middle course we use the lepton + jets channel.

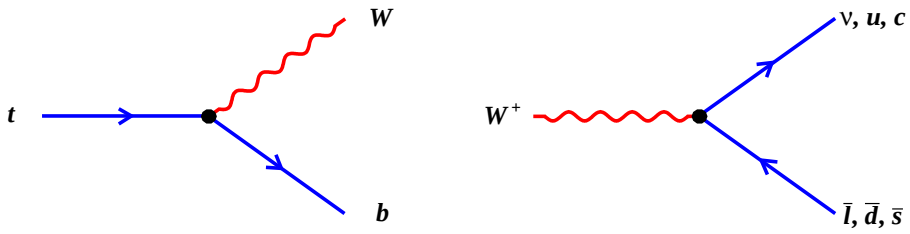

Figure 1.5: Top and W-decay vertices

W decay	Branching ratio
$e^+\nu_e$	$1/9 \sim 11.1\%$
$\mu^+\nu_\mu$	$1/9 \sim 11.1\%$
$\tau^+\nu_\tau$	$1/9 \sim 11.1\%$
$u\bar{d}$	$3/9 \sim 33.3\%$
$c\bar{s}$	$3/9 \sim 33.3\%$

Table 1.3: Branching ratio for the W boson to decay into the various combinations.

W_1 decay	W_2 decay	Branching ratio
Dilepton channel		
$e^+\nu_e$	$e^+\nu_e$	$1/81 \sim 1.2\%$
$e^+\nu_e$	$\mu^+\nu_\mu$	$2/81 \sim 2.4\%$
$e^+\nu_e$	$\tau^+\nu_\tau$	$2/81 \sim 2.4\%$
$\mu^+\nu_\mu$	$\mu^+\nu_\mu$	$1/81 \sim 1.2\%$
$\mu^+\nu_\mu$	$\tau^+\nu_\tau$	$2/81 \sim 2.4\%$
$\tau^+\nu_\tau$	$\tau^+\nu_\tau$	$1/81 \sim 1.2\%$
Hadronic channel		
$q\bar{q}$	$q\bar{q}$	$36/81 \sim 44.4\%$
Lepton + jets channel		
$e^+\nu_e$	$q\bar{q}$	$12/81 \sim 14.8\%$
$\mu^+\nu_\mu$	$q\bar{q}$	$12/81 \sim 14.8\%$
$\tau^+\nu_\tau$	$q\bar{q}$	$12/81 \sim 14.8\%$

Table 1.4: Branching ratios of $t\bar{t}$ events for the two W bosons to decay into the possible combinations.

1.2.3 W helicity in top quark decays

The weak interaction comes in two varieties : neutral-current and charged - current interactions. The top quark decays via the charged-current weak interaction. If one considers W^+ decay into leptons, see figure 1.5 b), we can immediately write down the Feynman rules for such a vertex, where γ^μ denotes the Dirac matrices, γ^5 the chirality operator and g the coupling constant of the electro-weak interaction:

$$-i\frac{g}{\sqrt{2}}\gamma^\mu\frac{1}{2}(1-\gamma^5) \tag{1.5}$$

Above expression is what is known as the vector $(\bar{\psi}\gamma^\mu\psi)$ minus axial vector $(\bar{\psi}\gamma^\mu\gamma^5\psi)$ form, or $V-A$ form of the weak current. The chirality is introduced by the following projection operators :

$$P_- = \frac{1}{2}(1-\gamma^5) \quad \text{left-handed projection} \tag{1.6}$$

$$P_+ = \frac{1}{2}(1+\gamma^5) \quad \text{right-handed projection} \tag{1.7}$$

This combination of vector and axial vector means that parity is violated, as this operator only projects out left-handed fermions or right-handed anti-fermions. The helicity operator $\vec{\sigma}\cdot\hat{p}$ acting on some state will return helicity eigenvalues. Effectively, helicity is the dot product of the spin and the unit-momentum vectors for a given particle. For a spin $\frac{1}{2}$ particle with its spin aligned parallel to the direction of motion, it could have helicity eigenvalues of $+\frac{1}{2}$ when the spin vector points in the direction of motion (right-handed), and $-\frac{1}{2}$ when the spin vector points in the direction opposite the motion of the particle (left-handed). In the extreme relativistic limit, the chirality operator γ^5 is equal to the helicity operator. Because the W boson is much more massive than its decay products, the chirality of the daughters will be nearly equivalent to their helicity. It can further be seen that the $V-A$ structure of the charged weak interaction only permits leptonic W^+-boson decay into left-handed leptons or right-handed anti-leptons. Assuming that only left-handed neutrinos are permitted in nature, we can draw the same conclusion regarding the charged-lepton handedness simply by considering conservation of total angular momentum, see figure 1.6a). In the W^+-boson rest frame, we may choose the z-axis such that the entire spin 1 of the W^+ boson points along it in the positive direction. For the leptonic decay into a left-handed electron-neutrino and a positron, the total angular momentum along the z-axis is only conserved if the positron is right-handed.
We are able to reach similar conclusions regarding the weak decay of the top quark. Using the Feynman rules, we can write down the mathematical representation of its decay vertex:

$$-i\frac{g}{\sqrt{2}}|V_{tb}|\gamma^\mu\frac{1}{2}(1-\gamma^5) \tag{1.8}$$

and note that it contains the same $V-A$ structure as the leptonic W^+ decay. Neglecting the b quark mass in comparison to that of the t quark and the W boson, we deduce that, like the neutrino in the W decay, the b quark in the top decay must be left-handed. We can use the same total angular momentum arguments as before, but this time we boost into the top quark rest frame and choose the z-axis such that the spin $\frac{1}{2}$ of the top quark is aligned in the positive direction, see figure 1.6b)-d). As one can see that of the three possible W^+ helicity states, only two are realizable due to the $V-A$ structure of the weak interaction. When polarization of the W^+ boson is completely orthogonal to its direction of motion (helicity ± 1), we denote this as W_R^+ or W_L^+ for the left or right helicity states and label these states "transversely polarized". If the polarization of the W^+ is parallel to it's direction of motion (helicity 0 state), we denote this as W_0^+ and name it "longitudinally polarized".

The Standard Model gives a specific prediction for the fraction F_0 of longitudinally polarized W bosons in top quark decay as a function of top and W masses, m_t and M_W [12].

$$F_0 = \frac{\Gamma(t \to W_0^+ b)}{\Gamma(t \to W_L^+ b) + \Gamma(t \to W_0^+ b) + \Gamma(t \to W_R^+ b)} = \frac{\frac{1}{2}(m_t/M_W)^2}{1 + \frac{1}{2}(m_t/M_W)^2} \quad (1.9)$$

where $\Gamma(t \to W_R^+ b)$ is set to zero. Using a top mass of 174.3 ± 5.1 GeV/c^2 in the formula above, the Standard Model predicts $F_0 = 0.701 \pm 0.012$. As mentioned before, the fraction of right-handed W^+-bosons is heavily suppressed and in the limit of a massless b quark exactly zero. With $m_t = 175$ GeV/c^2 and $m_b = 5$ GeV/c^2, the fraction of right-handed W^+-bosons in top decay is less than one-tenth of a percent [12].
The W boson helicity amplitudes are well-known, and the square of the amplitude $|\mathcal{M}|$, which determines the angular distributions is written as a function of the quantity $\cos\theta^*$ [12] :

$$\text{left-handed}: \quad |\mathcal{M}(W_L^+)|^2 = |\mathcal{M}(W_R^-)|^2 \sim \frac{1}{4}(1-\cos\theta^*)^2 \quad (1.10)$$

$$\text{longitudinal}: \quad |\mathcal{M}(W_0^+)|^2 = |\mathcal{M}(W_0^-)|^2 \sim \frac{1}{2}(1-\cos^2\theta^*) \quad (1.11)$$

$$\text{right-handed}: \quad |\mathcal{M}(W_R^+)|^2 = |\mathcal{M}(W_L^-)|^2 \sim \frac{1}{4}(1+\cos\theta^*)^2 \quad (1.12)$$

where, in the case of leptonic decays of the W boson, θ^* is defined as the angle between the charged-lepton momentum in the W rest-frame and the W momentum in the top quark rest-frame, see figure 1.7a). Note that the angular distribution for the W_L^+ and W_R^- helicity amplitudes are identical, as are the W_R^+ and W_L^-. Throughout this thesis, we will use "left-handed" to denote the W_L^+ and W_R^- transverse state, "right-handed" to denote the W_R^+ and W_L^- states, and "longitudinal" to signify both W_0^+ and W_0^-.

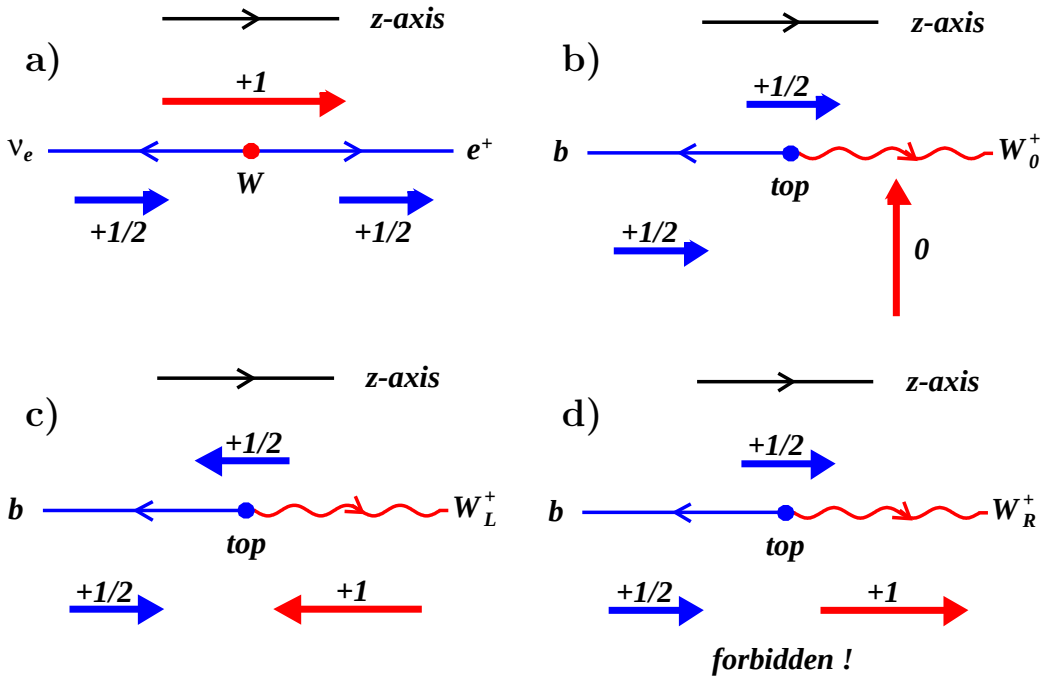

Figure 1.6: Figures depicting the total angular momentum along the z-axis after W^+ and t quark decay. a) W^+ boson decays into a left-handed neutrino and a right handed positron. The sum of angular momentum along the z-axis in figures b) and c) equals $+\frac{1}{2}$, identical to the angular momentum of the parent top quark along the axis, hence these decay modes are allowed. d) Conservation of total angular momentum forbids the decay of a t quark into a left-handed b quark and a right-handed W^+ boson.

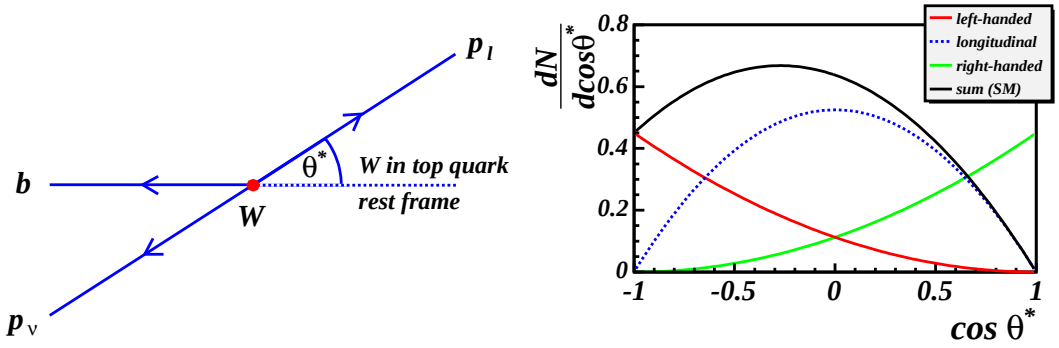

Figure 1.7: a) Schematic view of the helicity angle $\cos\theta^*$ in the W boson rest frame. b) Theoretically calculated $\cos\theta^*$ distribution for left-handed (red), longitudinal (blue dashed) and right-handed W bosons. The solid black line indicates the $\cos\theta^*$ distribution expected in the Standard Model.

Chapter 2

The Experiment

In this chapter we will present the experiment facility, the Fermi National Accelerator Laboratory, abbreviated Fermilab, and the different accelerators needed to reach a center-of-mass energy $\sqrt{s}$ of the colliding protons and anti-protons of 1960 GeV. We will then describe the CDF experiment, one of the two experiments located at the Fermilab, which delivers the data used for our measurement. The Fermi National Accelerator Laboratory is located approximately 40 miles west of Chicago in the State of Illinois. More than 2.500 scientists from 34 states and 25 countries use Fermilab facilities to carry out research in particle physics. In figure 2.1 an aerial shot of the Fermilab is shown.

Figure 2.1: Aerial shot of the Fermilab. The gray circle in front is the outer maintenance road of the Main Injector, the rear circle is the inner maintenance road of the Tevatron.

2.1 The Accelerator System

To reach the center-of-mass energy of 1960 GeV achieved at the Tevatron, a system of different accelerators is needed. A schematic overview of the accelerators is shown in figure 2.2.

The first stage of acceleration is provided by the Cockcroft-Walton pre-accelerator.

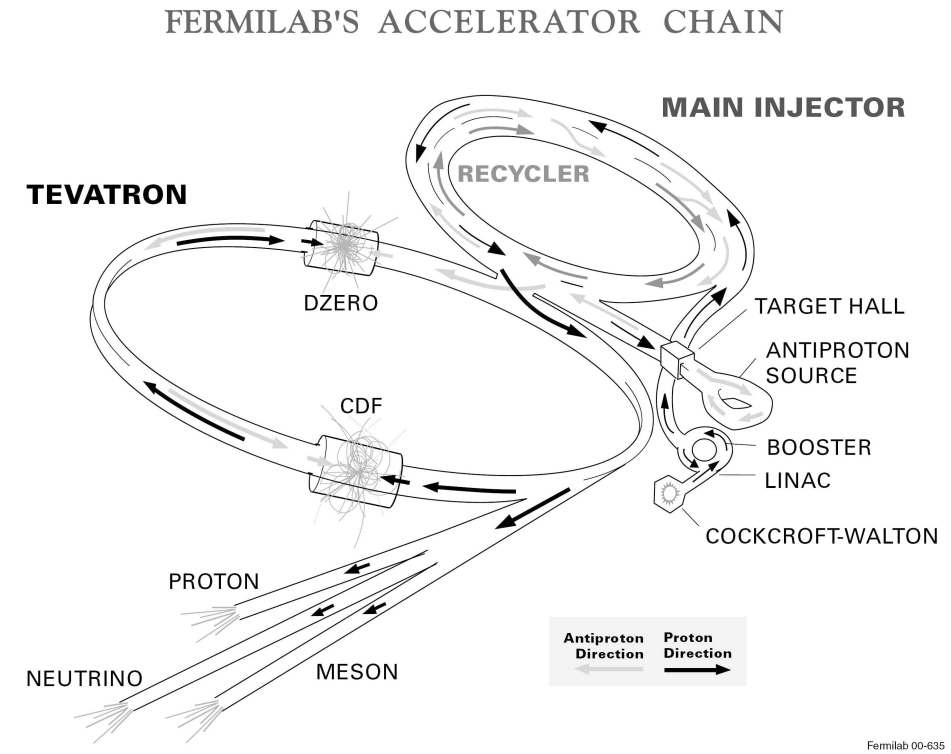

Figure 2.2: Diagram of Fermilab's accelerators for Run II

Inside this device, hydrogen gas is ionized to create negative ions. These ions are accelerated by a positive voltage and reach an energy of 750 keV.

Next, the negative hydrogen ions enter a linear accelerator (LINAC), approximately 130 meters long. Oscillating electric field accelerate the ions to 400 MeV. Before entering the third stage, the ions pass through a carbon foil, which strips the electrons.

The third stage, the booster, is a circular accelerator that uses magnets to bend the beam of protons in a circular path. The protons leave the booster with an energy of 8 GeV.

The next stage is the Main Injector. The Main Injector has four functions. It accelerates the protons up to 150 GeV, produces 120 GeV protons for the antiproton production, accelerates the antiproton to 150 GeV and injects protons and anti-protons into the Tevatron.

To produce anti-protons, the Main Injector sends 120 GeV protons to the Antiproton Source, where the protons collide with a nickel target. The collisions

produce a wide range of secondary particles including many anti-protons, which are collected, focused and then stored in the Accumulator Ring. When a sufficient number of anti-protons has been produced, they are sent to the Main Injector.
The final acceleration is done in the Tevatron, a collider with a circumference of about six kilometers. There, the protons and anti-protons get a final energy of nearly 1 TeV. During Run II, started in June 2001, the two beams collide with a center-of-mass energy of 1.96 TeV with 36 bunches per beam and a bunch spacing of 396 ns.

Another quantity characterizing a collider is the luminosity. The luminosity $\mathcal{L}$ is the product of incident beam flux with the mean target density. The event rate n for a certain process with cross section σ is given by the product $n = \mathcal{L} \cdot \sigma$. For Run II the integrated luminosity should be between 4.4 fb^{-1} (base line goal) and 8.5 fb^{-1} by the end of 2009 [13]. Unfortunately, the instantaneous luminosities achieved by the Tevatron have not met the design goal of $\mathcal{L} = 20 \text{ x } 10^{31}\text{cm}^{-2}\text{s}^{-1}$ [14], however, they are steadily increasing. This can be seen in figure 2.3 presenting the instantaneous peak luminosities of every store of Run II. Figure 2.4 displays the increase of the integrated luminosity delivered by the Tevatron and stored to tape at CDF since the start of Run II. The data used in this analysis are taken from march 2002 to september 2004.

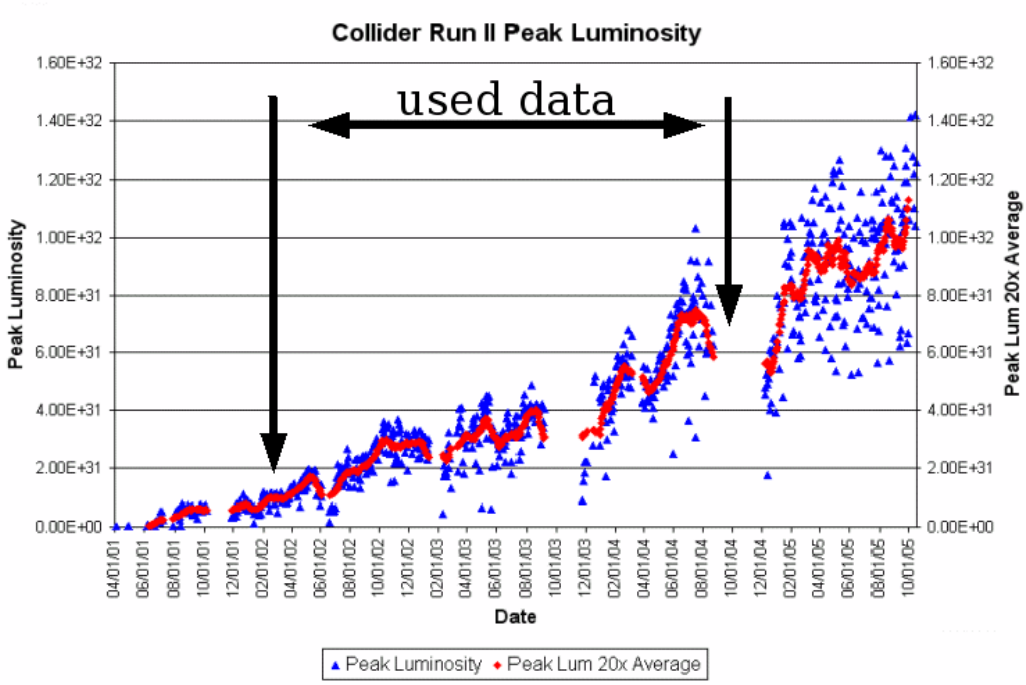

Figure 2.3: Peak luminosity per store since the start of Run II.

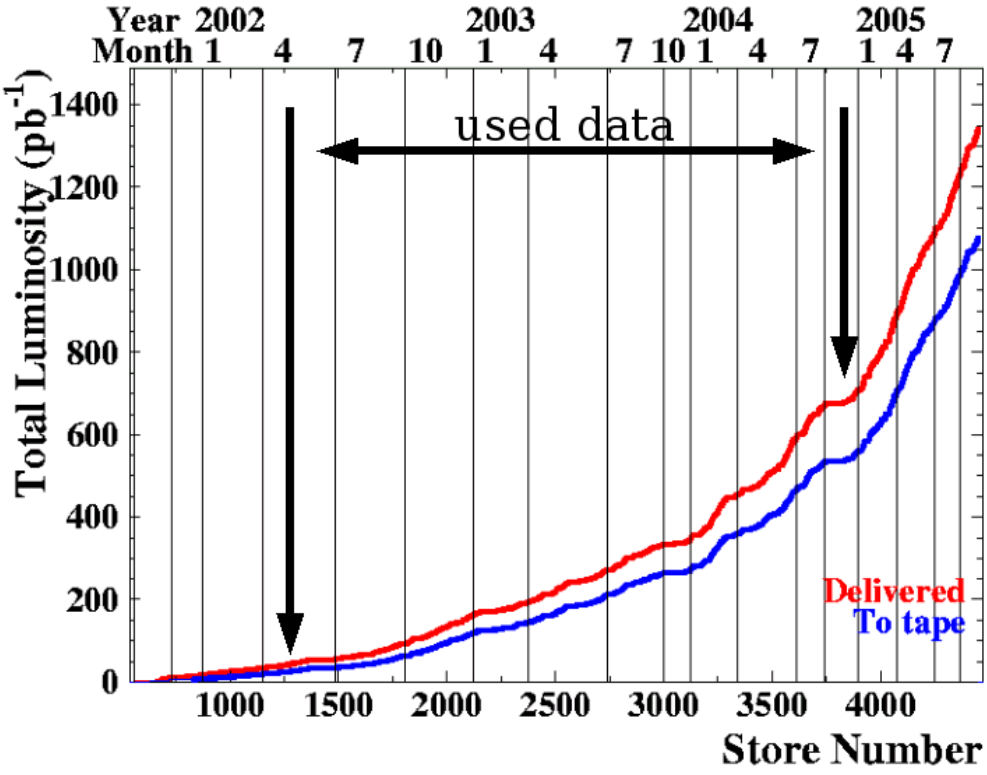

Figure 2.4: Delivered (upper curve) and recorded (lower curve) integrated luminosity since the start of Run II. The data taken from March 2002 to September 2004 was used for the analysis presented in this thesis.

2.2 CDF Detector

One of the two multipurpose detectors located at the Tevatron is the CDF experiment. The task of the detectors is to track charged particles and measure the momentum and energy of both the charged and neutral particles.
The CDF detector in Run II (CDF II) is a general purpose solenoidal detector

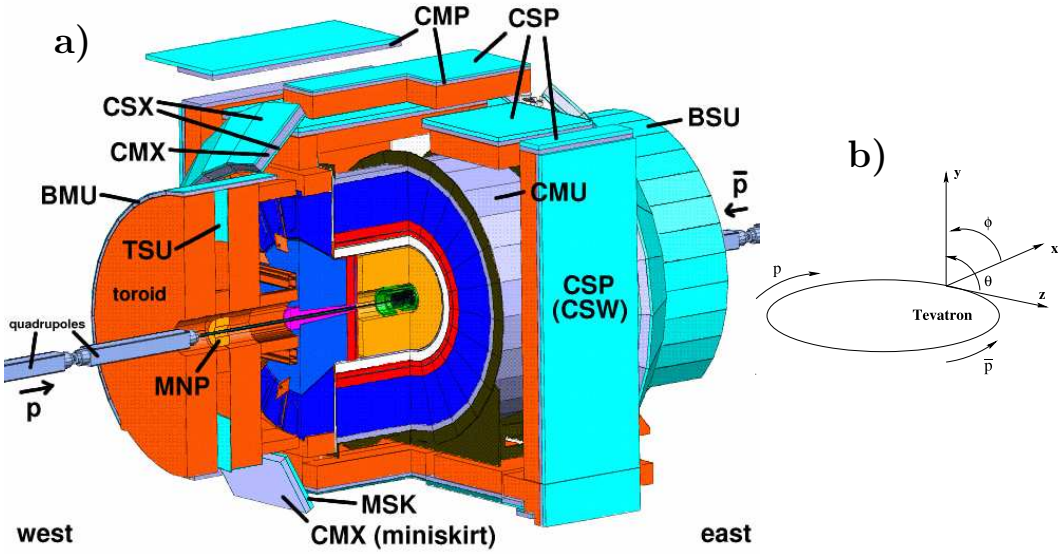

Figure 2.5: a) Isometric view of CDF in Run II with the abbreviations of the different components of the muon system. The inner green and orange parts represents the tracking system and the blue one the calorimeters. b) The coordinate system of the CDF II detector.

combining charged particle tracking, fast projective calorimetry and fine grained muon detection. The detector has both azimuthal and forward-backward symmetry. In figure 2.5 a solid cutaway view is shown. The coordinate system for CDF is defined as: The polar angle θ in cylindrical coordinates is measured from the proton beam axis (z-axis) and the azimuthal angle ϕ is measured from the plane, defined by the Tevatron ring. Throughout this thesis, longitudinal means parallel to the proton beam and transverse means perpendicular to the proton beam. The pseudorapidity is defined by $\eta = -ln(tan\frac{\theta}{2})$. The CDF II detector is built and maintained by a collaboration of more than 50 institutes in eleven countries. The only German institute in the collaboration is the *Institut für Experimentelle Kernphysik* in Karlsruhe.
Figure 2.6 shows an elevation view of one half of the CDF II detector. The tracking system is surrounded by a superconducting solenoid, 1.5m in radius and 4.8 m in length, generating a 1.4 T magnetic field parallel to the beam axis. The calorimeter and the muon system are outside the magnet.
The detector components important for the measurement of this thesis are described in more detail.

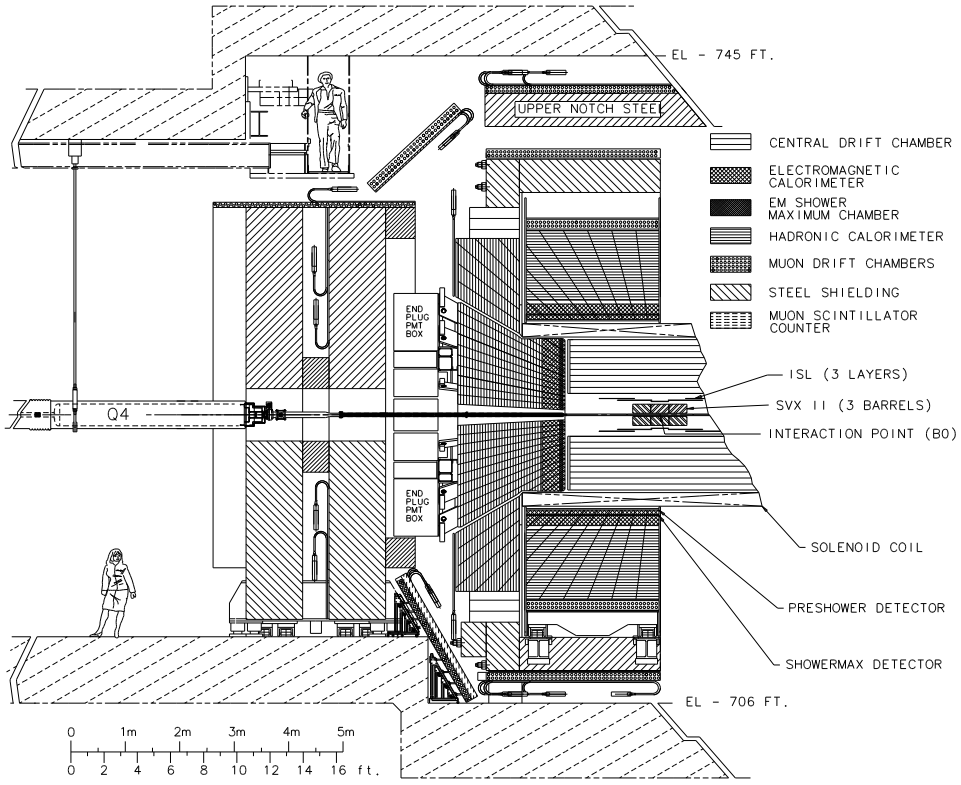

Figure 2.6: Elevation view of one half of the CDF II detector

2.2.1 Tracking

The Tracking System in Run II consists of 3 parts. The SVXII, a *Silicon VerteX detector* [15], the ISL, *Intermediate Silicon Layers* [16] and the COT, the *Central Outer Tracker*, an open drift chamber [17]. A schematic overview is given in figure 2.7.

Closest to the beam pipe is the SVX II. The detector design is driven by the high Run II luminosity, the Tevatron short bunch spacing of 396 ns, and the physics requirements of b decay vertex identification within collimated high-p_T jets. The SVX II is comprised of three cylindrical barrels which cover $|z| <$ 0.43 m providing track information to pseudo-rapidity $|\eta| < 2$. Five layers of double sided silicon sensors at radii from 2.4 to 10.7 cm supply $r - \phi$ as well as 3 $r - z$ and 2 small angle stereo measurements. The results provide good pattern recognition and 3-d vertex reconstruction with an impact parameter resolution $\sigma_\phi < 30\,\mu$m and $\sigma_{z_0} < 70\,\mu$m for central high momentum tracks [14]. The impact parameter is the distance of closest approach of the track helix to the beam axis, measured in the plane perpendicular to the beam. Since SVX II provides coverage up to $|\eta| \sim 2$, in the region $|\eta| < 1$ the combination of the SVX II and the COT can provide full 3D tracking, but the reconstruction will need to be anchored on COT tracks. For $|\eta| > 1$, SVX II can only provide 2D tracking. Therefore, as seen in figure 2.7, there are two additional silicon layers

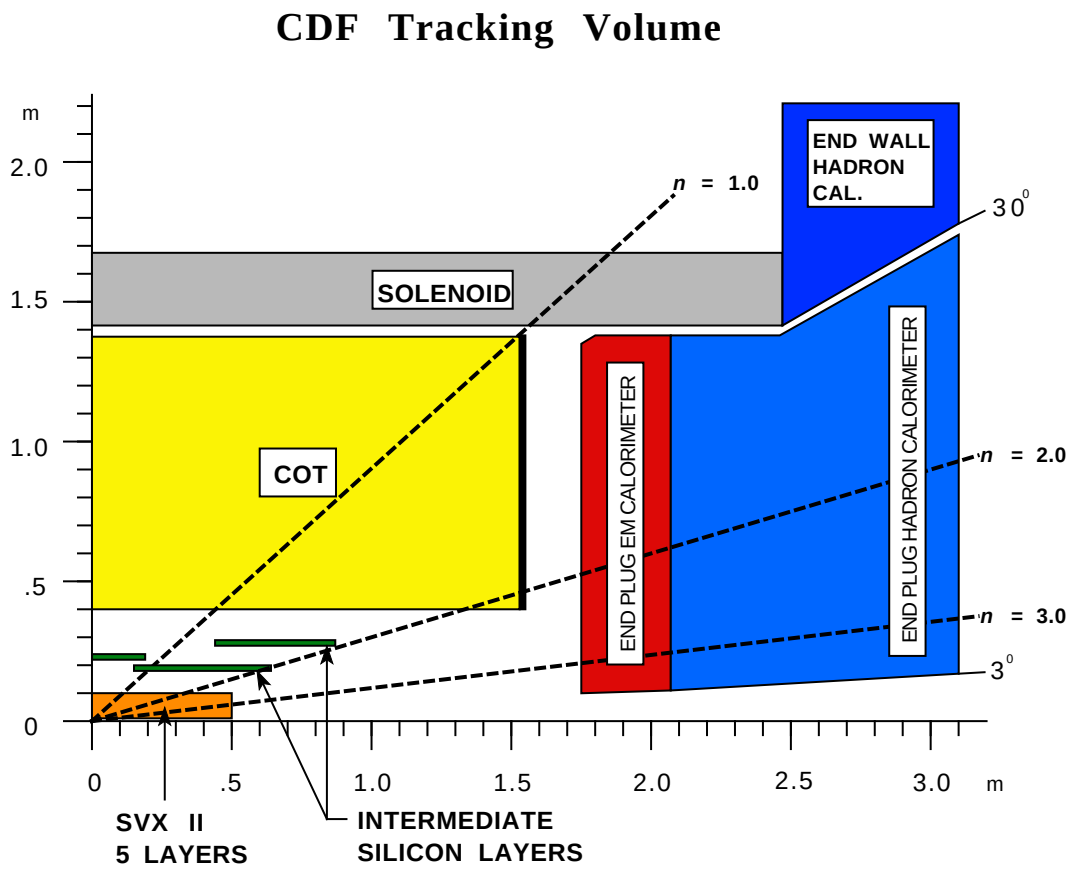

Figure 2.7: Longitudinal view of the CDF II tracking system

at radii of 20 cm and 28 cm. The third layer of the ISL, placed at radius of 22 cm, provides stand-alone tracking.

The third part of the tracking system is the COT, a 3.1m long cylindrical open drift chamber, which provides tracking at large radii in the region $|\eta| < 1.0$. The COT covers the radial range from 40 to 137 cm and provides 96 measurement layers organized into alternating axial and ± 2 stereo superlayers. The hit position resolution is approximately 140 μm and the momentum resolution $\sigma(p_T)/p_T^2 \sim 0.0015\,(\mathrm{GeV}/c)^{-1}$. Due to the high Luminosity and the short bunch spacing, the COT is designed to operate with a maximum drift of 100 nsec by reducing the maximum drift distance and by using a gas mixture with a faster drift velocity [14].

2.2.2 Calorimeter

The solenoid and tracking volume is surrounded by the calorimeters, designed to measure the energy of particles and jets by fully absorbing all particles except muons and neutrinos. There are, altogether, five calorimeter systems: CEM,*Central ElectroMagnetic calorimeter*, CHA, *Central HAdron calorimeter*,

WHA, *end-Wall HAdron calorimeters*, PEM *end-Plug ElectroMagnetic* and PHA *end-Plug HAdron calorimeter*, covering 2π in azimuth and $\eta = -3.6$ to $\eta = 3.6$ in pseudo-rapidity, see figure 2.6. Each calorimeter module is divided into projective towers, pointing to the nominal interaction point. The segmentation of the single modules is shown in table 2.1.
The calorimeters are sampling calorimeters. The active medium is a scintillator, the absorber is lead in the electromagnetic calorimeter and iron in the hadronic calorimeter. The different energy resolutions and $|\eta|$ ranges for the several calorimeters are given in table 2.2.

$\|\eta\|$ range	$\|\Delta\phi\|$	$\Delta\eta$	Calorimeter
$\|\eta\| < 1.3$	15^o	~ 0.1	Central and End Wall
$1.1 < \|\eta\| < 1.2$	7.5^o	~ 0.1	End-Plug Electromagnetic
$1.2 < \|\eta\| < 1.8$	7.5^o	~ 0.1	
$1.8 < \|\eta\| < 2.1$	7.5^o	~ 0.1	End-Plug Electromagnetic
$1.8 < \|\eta\| < 2.1$	7.5^o	~ 0.15	& Hadron
$2.1 < \|\eta\| < 3.6$	15^o	0.2 - 0.6	

Table 2.1: Calorimeter segmentation.

Calorimeter	$\|\eta\|$ range	Energy resolution
Central Electromagnetic (CEM)	$\|\eta\| < 1.1$	$13.5\%/\sqrt{E} \oplus 2\%$[18]
End-Plug Electromagnetic (PEM)	$1.1 < \|\eta\| < 3.6$	$16\%/\sqrt{E} \oplus 1\%$ [20]
Central Hadron (CHA)	$\|\eta\| < 0.9$	$75\%/\sqrt{E} \oplus 3\%$[19]
End Wall Hadron (WHA)	$0.9 < \|\eta\| < 1.3$	$75\%/\sqrt{E} \oplus 3\%$[19]
End-Plug Hadron (PHA)	$1.3 < \|\eta\| < 3.6$	$74\%/\sqrt{E} \oplus 4\%$[20]

Table 2.2: Overview of the CDF calorimeter properties.

2.2.3 Muon Chambers

Four systems of scintillators and drift tubes are used to detect muons with CDF [21]. The central calorimeters act as a hadron absorber for the *Central MUon Detector* (CMU). The CMU consists of four layers of drift chambers located outside the central hadronic calorimeter. It covers 84% of the solid angle for the pseudorapidity interval $|\eta| < 0.6$ and could be reached by muons

with transverse momenta greater than 1.4 GeV/c. Behind the CMU there are 0.6m of steel and additional four layers of drift chambers behind the steel. This system is called *Central Muon uPgrade* (CMP). For $|\eta| < 0.6$ the CMP covered 63% of the solid angle while both systems have an overlap of 53% of the solid angle. In addition the pseudorapidity range of $0.6 < |\eta| < 1.0$ was covered by the *Central Muon eXtension* (CMX) to 71% of the solid angle. Since Run II new chambers has been added to the CMP and CMX systems to close gaps in the azimuthal coverage and improve the shielding. The forward muon system has been replaced with the *Intermediate MUon system* (IMU) covering a range from $1.0 < |\eta| < 1.5$. Table 2.3 gives an overview of the different muon systems in Run II.

	CMU	CMP/CSP	CMX/CSX	IMU
coverage	$\|\eta\| < 0.6$	$\|\eta\| < 0.6$	$0.6 < \|\eta\| < 1.0$	$1.0 < \|\eta\| < 1.5$
drift tubes	2304	1076	2208	1728
counters		269	324	864
min p_T	1.4 GeV/c	2.2 GeV/c	1.4 GeV/c	1.4 - 2.0 GeV/c

Table 2.3: Design parameters of the CDF II muon detectors.

2.3 Data Acquisition and Monitoring

2.3.1 Trigger

The trigger plays an important role in efficiently extracting the most interesting physics events from the large number of minimum bias events, because the collision rate is equal to the crossing rate of 1.7 MHz while the tape writing speed is limited to an event rate of about 75 Hz at present. The CDF trigger is a three level system with each level providing a sufficient rate reduction for the processing of the next level [22], shown in figure 2.8.

The first two triggers are hardware triggers, the block diagram is shown in figure 2.9 the last one is a software trigger running on a Linux PC farm. Level-1 uses custom designed hardware to find physics object based on a subset of the detector. The hardware consists of three parallel synchronous processing streams, one finds calorimeter based objects, another finds muons while the third finds tracks in the COT using the *eXtremly Fast Tracker* (XFT). The decision is done by simple counting these objects (e.g. one electron with 12 GeV). If an event is accepted by the Level-1 trigger, the data are moved to one of the four on-board Level-2 buffers, to average out the rate fluctuations. The typical rate of the Level-1 triggers is at present 18 kHz accept rate.

The Level-2 trigger performs a limited event reconstruction using a custom designed hardware. The hardware consists of several asynchronous subsystems, e.g. the hardware cluster finder using calorimeter informations. In addition, data from the *CEntral Shower maximum detector* (CES) can be used to improve the identification of electrons and photons. The most challenging addition for the Level-2 trigger is the *Silicon Vertex Tracker* [23]. The SVT allows to select tracks with large impact parameter, which opens a complete new window for physics measurements at a hadron collider. The Level-2 trigger accepts 300 events per second, which are transferred to the Level-3 processor farm [24].

At the processor farm the events are reconstructed and filtered, using the algorithms run in the "offline" reconstruction, and are written to permanent storage with approximately 75 Hz at present. To facilitate the handling of the huge data volumes collected with the CDF detector, passing the Level-3 trigger, are currently split into eight different streams. The triggers, an event has passed, decide to which streams this event belongs e.g. all events passing any of the high energy lepton triggers end up in "stream B".

In figure 2.10 the Event Display of a W-boson candidate event with four jets is shown.

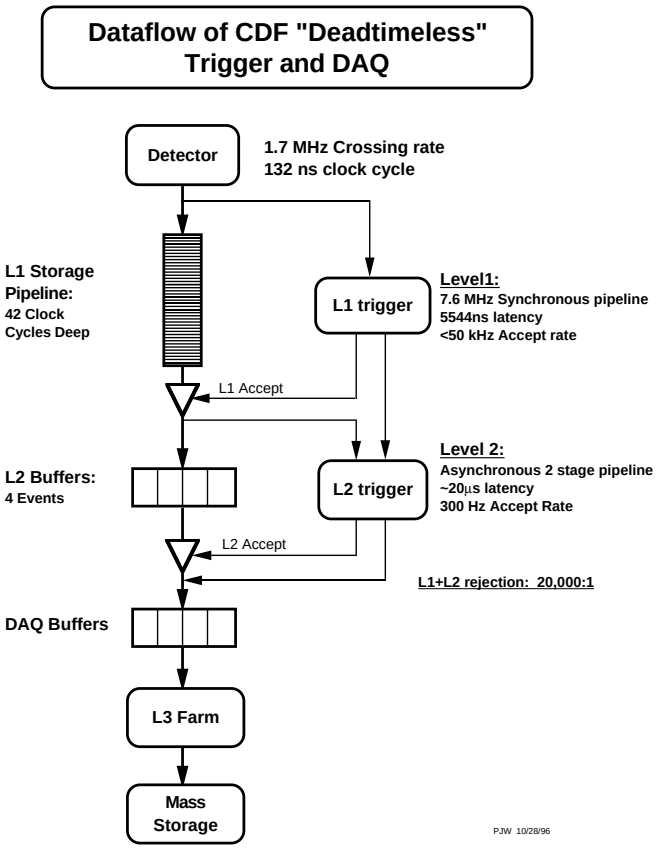

Figure 2.8: Block diagram of the CDF II data flow.

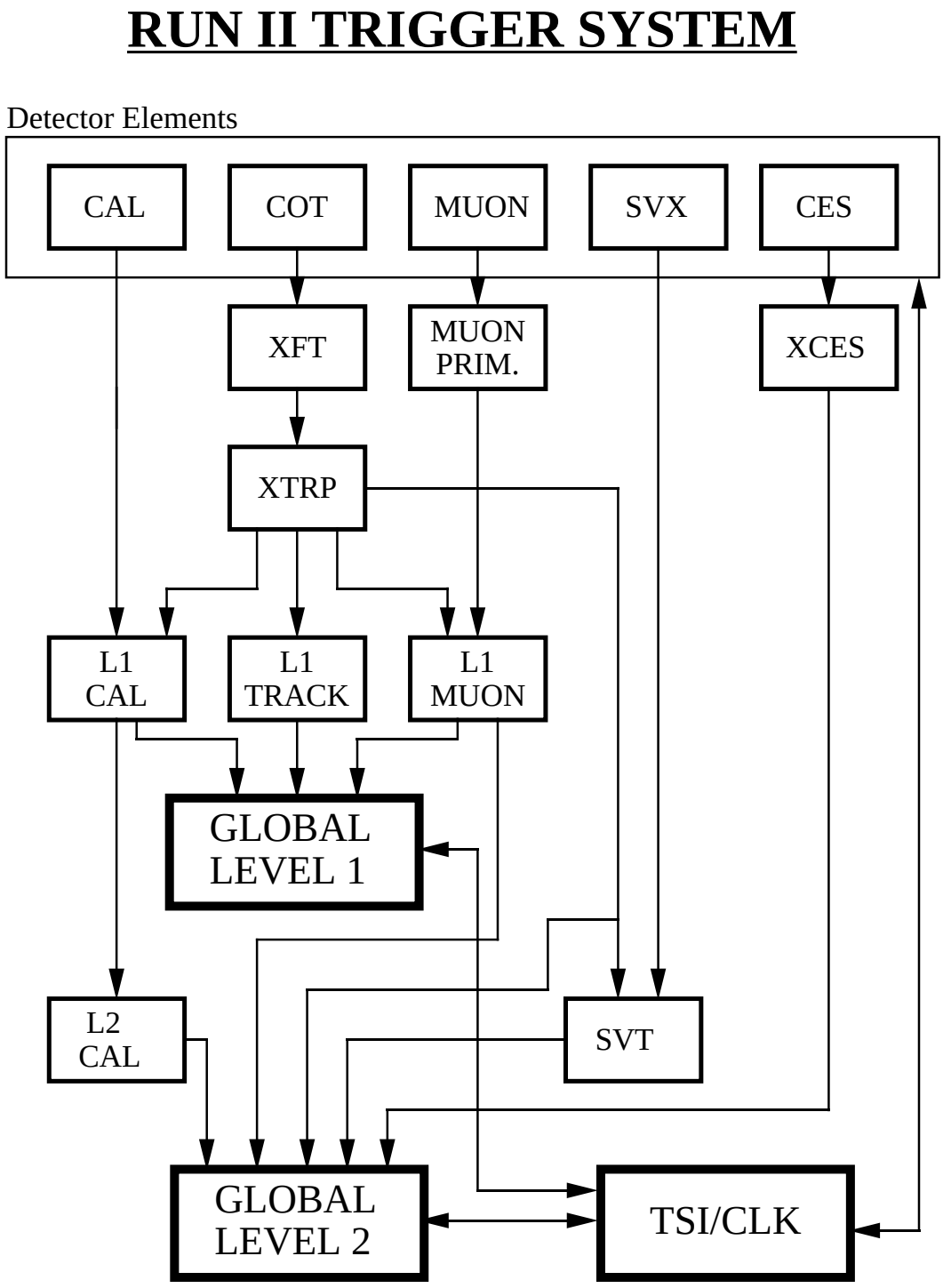

Figure 2.9: Block diagram of the CDF hardware trigger system in Run II.

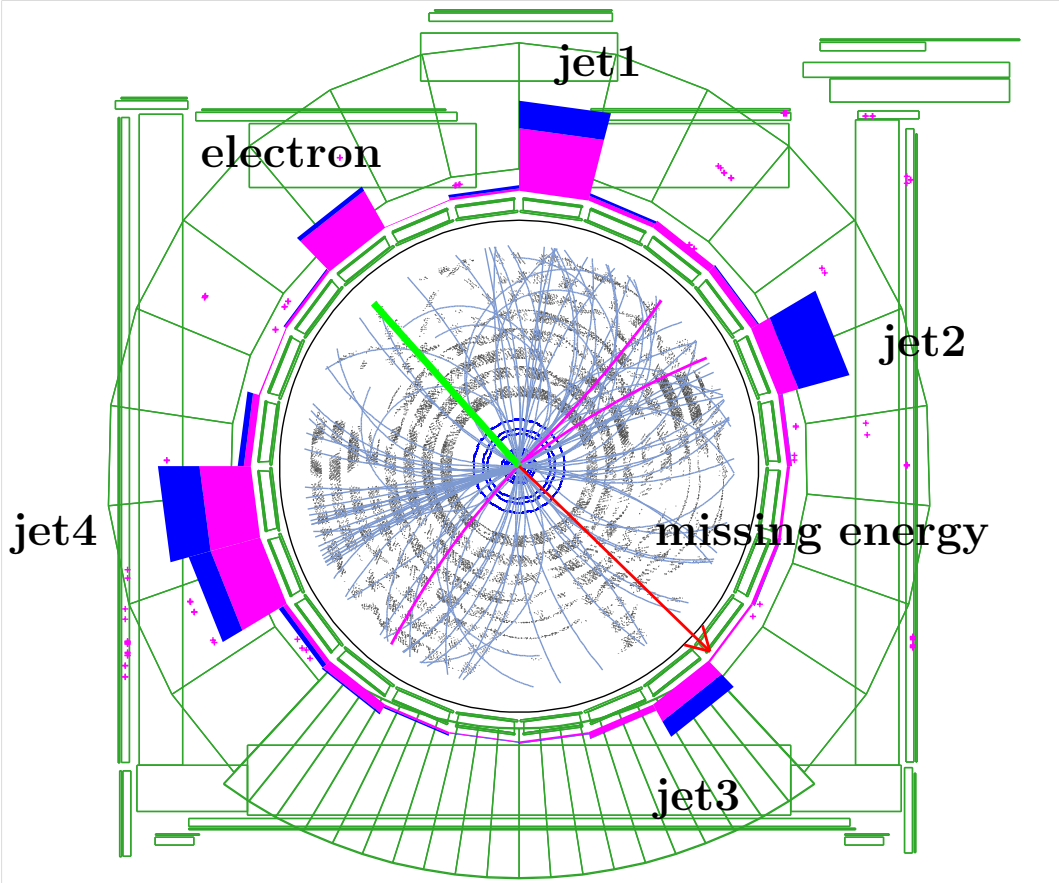

Figure 2.10: Event display of a $t\bar{t}$ candidate with four jets. The energy of the electro-magnetic calorimeter towers are drawn magenta, the energy of the hadronic calorimeter towers are drawn blue. The size of the cluster is proportional to the measured energy. The red arrow represents the direction of the missing energy. The inner part of the picture represents the tracking system. The gray points are hits in the COT, the blue points of the inner most rings are hits of the silicon vertex detector. The green line, a isolated track pointing to a calorimeter tower with energy deposition represents an electron.

2.3.2 Online Monitoring

A complex multi-purpose detector, like CDF, consists of many different detector systems. To take data with high efficiency and high quality it is necessary to quickly spot problems with one of the subdetectors. This can be achieved by monitoring the data during data taking. At CDF, all processes receiving data from the *Data AcQuisition* (DAQ) are called *consumers* [25].
For this purpose the so called *Consumer Framework* based on the ROOT package [26] was developed. A schematic view of the framework is shown in figure 2.11. The most important feature is that the part which displays the monitored results is separate from the actual consumer programs. The framework

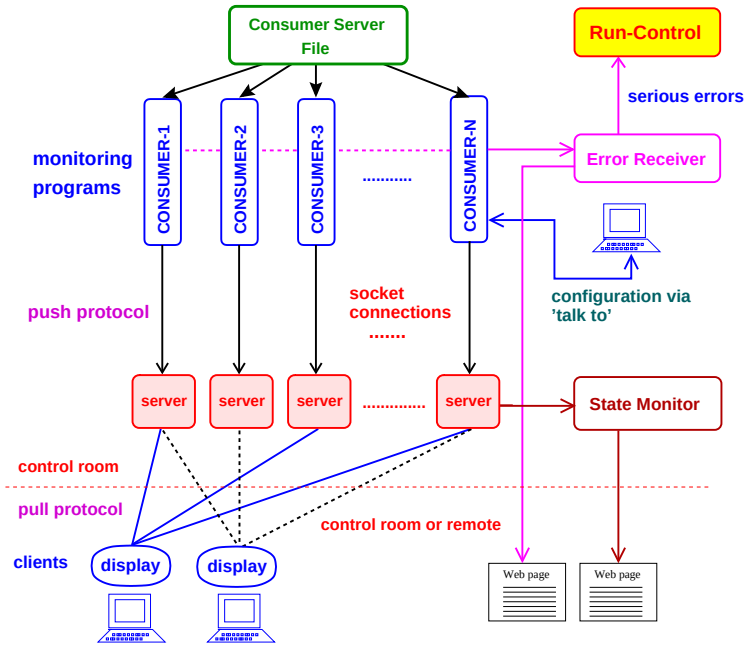

Figure 2.11: Overall design of the consumer framework

has three main components:

- **Consumers:** These are the modules which monitor and analyze objects in the event stream. They provide the connection to the rest of the CDF offline framework.
- **Display Server / Display Viewer:** The Display Server is a ROOT based program that allows the display viewer programs to connect to it as a client. Multiple display viewer programs can connect from anywhere in the world.
- **Error Handler:** This process receives the error messages from the different consumers and communicates with runcontrol so that the appropriate action can be taken (e.g. reset a SVX CHIP).

Chapter 3

Data and Monte Carlo Samples

In this chapter the data and Monte Carlo samples we used for the analysis are described. We give a short introduction to the functionality of Monte Carlo generators and describe them with a few words.

3.1 Data Samples

Since we will analyse the lepton+jets channel we will use the data stream including all inclusive high-p_T lepton samples. The data used in this analysis originates from the so called "stream b"of the CDF data taking [22]. Data are re-processed offline before being used by the different physics groups. During the re-processing calibrations used online are checked and corrected, silicon alignment is corrected, tracks are re-fit, cluster energies are checked, leptons are found, and algorithms which "tag" secondary vertices in jets are run. The data used in our analysis were re-processed with CDFSOFT2 version 5.3.3 and further on stripped into two datasets `bhel0d/bhmu0d` by the CDF lepton+jets group. The electron data (`bhel0d`) have to pass level 3 trigger `ELECTRON_CENTRAL_ET18`, the muon data (`bhmu0d`) have to pass level 3 trigger `MUON_CMUP18` or `MUON_CMX18`. The detailed trigger path is given in Appendix A.1. The main requirements of these trigger paths are a track in the COT and a matching signal in the corresponding detector component (CEM, CMUP, CMX).
Once the bunches of protons and anti-protons are injected into the Tevatron they collide until the instantaneous luminosity has fallen to the point at which it becomes difficult to collimate the two beams. This is a flexible end point, as determined by the Tevatron operations crew during running. This period of collisions is known as a store. Each store is broken up into several smaller chunks called runs. Runs begin with data taking online and are ended typically due to a detector subsystem pulling an error line, making data collection temporarily impossible. Several runs may be taken during one store. Once data for an analysis has passed the online trigger requirements the good-run list is

applied as a check on data quality. Runs are examined both online and offline to verify the quality of data recorded. This is done for all subsystems separately. For our analysis we require a functional silicon detector, a functional COT and a functional calorimeter system with preshower detectors. Only those runs are included where these detector components were active and marked as good. The good run list is proposed by the CDF Top Group [27]. For the complete list see Appendix A.2. Additionally run 164844 was removed due to *Consumer Server Logger* problems, which is the central online hub through which all data taken during CDF Run II must pass. This good run list does not include runs taken between Feb. and May 2004, when the COT exhibited varying inefficiencies due to aging problems. CMX muons can first be analysed starting with run 150145 because of the non functional CMX detector components in the runs before. The chosen data sample corresponds to an integrated offline luminosity for CEM / CMUP of $318.5 \pm 18.8\, pb^{-1}$ and for CMX of $305.2 \pm 18.0\, pb^{-1}$ [28]. An overview of the used data samples and the corresponding run range is given in table 3.1.

Dataset	Trigger (Level 3)	Events	Run range
bhel0d	Electron_CENTRAL_ET18	1963238	138425 - 186598
bhmu0d	Muon_CMUP18	719401	138425 - 186598
	Muon_CMX18		150145 - 186598

Table 3.1: Used data samples with corresponding run range.

3.2 Monte Carlo Samples

Before describing the different Monte Carlo generators used to produce the different samples, we give a short overview of the main features of the processes which are simulated by these generators. It can be divided notionally into four components, corresponding roughly to increasing scales of distance and time:

1. **Elementary hard subprocess:** A pair of incoming beam particles or their constituents interact to produce one or more primary outgoing fundamental objects. This can be computed exactly to lowest order in perturbation theory. The hard momentum transfer scale Q together with the color flow of the subprocess set the boundary conditions for the initial and finalstate parton showers, if there are any.

2. **Initial and finalstate parton showers:** A parton constituent of an incident beam hadron with low spacelike virtuality can radiate timelike partons. In the process it decreases its energy to a fraction x of that of the

beam and increases its spacelike virtuality, which is bounded in absolute value by the scale Q of the hard subprocess. This initialstate emission process leads to the evolution of the structure function F(x; Q) of the incident hadron. On a similar time scale, an outgoing parton with large timelike virtuality can generate a shower of partons with lower virtuality. The amount of emission depends on the upper limit on the virtuality of the initiating parton, which is again controlled by the momentum transfer scale Q of the hard subprocess. Timelike partons from the initialstate emission may in turn initiate parton showering. The coherence of soft gluon emission from different parton showers is controlled by the color flow of the subprocess.

3. **Heavy object decays:** Massive produced objects such as top quarks or electroweak gauge bosons can decay on timescales that may be shorter than or comparable to that of the QCD parton showers. Depending on their nature and the decay mode, they may also initiate parton showers before and/or after decaying.

4. **Hadronization process:** In order to construct a realistic simulation one needs to transform the partons into hadrons. This applies to the constituent partons of incoming hadronic beams as well as to the outgoing products of parton showering, which give rise to hadronic jets. This hadronization process takes place at a low momentum transfer scale, for which the strong coupling is large and perturbation theory is not applicable. In the absence of a firm theoretical understanding of nonperturbative processes, it must be described by a phenomenological model, which can be different for the various generators.

3.2.1 Description of the different Monte Carlo generators

Herwig

HERWIG [30] is a general-purpose event generator for high energy processes, with particular emphasis on the detailed simulation of QCD parton showers. The program provides a full simulation of hard lepton-lepton, lepton-hadron and hadron-hadron scattering and soft hadron-hadron collisions in a single package, and has the following special features:

- Initial and finalstate QCD jet evolution with soft gluon interference taken into account via angular ordering.

- Color coherence of (initial and final) partons in all hard subprocesses, including the production and decay of heavy quarks and supersymmetric particles.

- Azimuthal correlations within and between jets due to gluon interference and polarization.

- A cluster model for jet hadronization based on nonperturbative gluon splitting and a similar cluster model for soft and underlying hadronic events.

- A spacetime picture of event development, from parton showers to hadronic decays, with an optional color rearrangement model based on spacetime structure.

The model adopted in HERWIG is intended to disrupt as little as possible the event structure established in the parton showering phase. Showering is terminated at a low scale, $Q < 1$GeV, and the preconfinement property of perturbative QCD is exploited to form colorneutral clusters which decay into the observed hadrons. Initialstate partons are incorporated into the incoming hadron beams through a soft, nonperturbative "forced branching" phase of spacelike showering. The remnants of an incoming hadron, i.e. these constituent partons which do not participate in the hard subprocess, undergo a soft "underlying event" interaction modeled on soft minimum bias hadronhadron collisions.

Pythia

PYTHIA [31] is a program for the generation of high-energy physics events, i.e. for the description of collisions at high energies between elementary particles such as e^+,e^-, p and $\bar{p}$ in various combinations. Together they contain theory and models for a number of physics aspects, including hard and soft interactions, parton distributions, initial and final state parton showers, multiple interactions, fragmentation and decay. They are largely based on original research, but also borrow many formulae and other knowledge from the literature.

Alpgen

ALPGEN [32] is a new event generator dedicated to the study of multiparton hard processes in hadronic collisions. The program performs, at the leading order QCD and electroweak interactions, the calculations of the exact matrix elements for a large set of parton-level processes. The current version describes among others W boson production associated with heavy and light quark jet production for up to six jets. The decay of W bosons includes spin correlations. Parton-level events are generated, providing full information on their color and flavor structure, enabling the evolution of the partons into fully hadronised final states.

3.2.2 Used samples

After generating events with the different Monte Carlo generators these events are sent through a GEANT3[1] detector simulation [33]. GEANT describes the passage of particles through matter. It allows for a full simulation of the detector response to particles created during collisions. The simulation was tuned to match the data. A detailed description can be found elsewhere [34]. Once processed by GEANT the simulated events can be manipulated in the same way as real data which has been collected by the detector.
The used Monte Carlo samples can be divided into three categories, signal and background samples and samples for systematic studies. To develop our analysis and verify the method we use about 1.1 million $t\bar{t}$ Monte Carlo events generated with PYTHIA (ttopel). Since the Monte Carlo samples were generated by the CDF lepton + jets group we use these samples for practical reasons. The background samples can not be generated with HERWIG or PYTHIA, therefore Alpgen was used to generate parton level events. These events are forwarded afterwards to HERWIG where the hadronization is done. For the background modeling two different processes are used. We use samples where a real W boson plus four partons was generated. There the W boson was forced to decay leptonically. One part of the events contains only light quarks among the four partons (atop7a / atopfb), the other part contains two b quarks among the four partons (atoppb / atopjb).

For systematic studies we use different $t\bar{t}$ samples. To study the effects of the event generation we also look into samples produced by PYTHIA. The influence of the modeling of initial (ISR) and final state radiation (FSR) is considered using several samples generated with PYTHIA with different settings. The effect of different top quark masses is studied with Herwig datasets, where the top quark mass was set to 172.5 GeV/c^2, 175 GeV/c^2 and 178 GeV/c^2, respectively. The last group of systematic samples are PYTHIA generated samples with different PDFs. As standard PDF for Monte Carlo production the CTEQ5L PDF is used. For systematic studies we use also samples with MRST72 and MRST75 PDFs.

All Monte Carlo samples used have realistic simulation based on run numbering [35]. The reconstruction behaves exactly the same on these samples as it does on data samples. The run range used for simulation is based on an early version of the DQM good run list.

A summary of the used samples with the name of the generator, the set top quark mass, special settings and the number of generated events is given in table 3.2

[1] Version 3.2113

Dataset	Process	Generator	Comment	Events
Signal sample				
ttopel	$t\bar{t}$, $m_t = 178$ GeV/c^2	PYTHIA 6.216		1150043
Background samples				
atop7a	$W \to e\nu$ + 4p	Alpgen 1.3/Herwig 6.504		243427
atopfb	$W \to \mu\nu$ + 4p	Alpgen 1.3/Herwig 6.504		287271
atoppb	$W \to e\nu$ + 2b + 2p	Alpgen 1.3/Herwig 6.504		235221
atopjb	$W \to \mu\nu$ + 2b + 2p	Alpgen 1.3/Herwig 6.504		239255
Systematic samples				
ttop0z	$t\bar{t}$, $m_t = 175$ GeV/c^2	PYTHIA 6.203		205999
ttophl	$t\bar{t}$, $m_t = 178$ GeV/c^2	Herwig 6.504		1267964
ttopvh	$t\bar{t}$, $m_t = 175$ GeV/c^2	Herwig 6.504		219479
ttopdh	$t\bar{t}$, $m_t = 172.5$ GeV/c^2	Herwig 6.505		233448
ttopbr	$t\bar{t}$, $m_t = 178$ GeV/c^2	PYTHIA 6.216	less ISR	930469
ttopdr	$t\bar{t}$, $m_t = 178$ GeV/c^2	PYTHIA 6.216	more ISR	924118
ttopfr	$t\bar{t}$, $m_t = 178$ GeV/c^2	PYTHIA 6.216	less FSR	932334
ttopkr	$t\bar{t}$, $m_t = 178$ GeV/c^2	PYTHIA 6.216	more FSR	466292
ttopir	$t\bar{t}$, $m_t = 178$ GeV/c^2	PYTHIA 6.216	MRST72	903057
ttopjr	$t\bar{t}$, $m_t = 178$ GeV/c^2	PYTHIA 6.216	MRST75	932381

Table 3.2: Used Monte Carlo samples for signal and background modeling and systematic studies. The top quark mass used in the production as well as the used Monte Carlo generator are given. For information the generated events are given in the last column.

Chapter 4

Analysis Techniques

Going from the raw data taken by the detector to "high level objects" usable for analysis is a great challenge and needs a lot of knowledge of the detector and reconstructing algorithms.
In this analysis the first step is done within the CDF Software Framework. The CDF Software Framework contains all algorithms needed to reconstruct the output of the detector or the simulation of objects usable for a physics analysis. It also contains top specific algorithms which create top specific objects and variables in a common way for a top quark related analysis. To analyse easily and independently from the CDF environment and decrease the event size, the data are converted into `TopNtuple`, a ROOT tree based data format. The analysis itself is done with the new analysis toolkit *Physics Analysis eXpert* (PAX). An schematic overview of the different stages of the first part of the analysis is given in figure 4.1.

4.1 The CDF Software Framework

The CDF Software Framework [36] is an application framework in the context of a HEP experiment. This "system" allows physicists to develop code which can be combined with code developed by other people and be used in both the online and offline environments, using either real or simulated data as input and allowing new data to be output. This output then forms the input in the next stage of a multistage data reduction environment. Therefore this framework is written in C++ to profit of the advantages of object oriented programming and is called AC++. The goals of this product is to provide a simple and straightforward means of combining any number of independent classes, called modules, into a single executable image and to provide a flexible system for specifying (either interactively or in batch mode) how these modules are run. A module is a fragment of code written by the physicist for a special purpose, e.g. clustering, and in general independent from other modules. A module has

a welldefined interface and performs a welldefined service inheriting from an abstract parent class. In a typical AC++ job these modules are connected in a way that the output of one module is the input of the next module, starting with the `InputModule`, which handles the reading of the data from disk, and finishing with the `OutputModule`, which handles the writing of the data back to disk. As this framework contains everything which is needed from the output of the detector to the reconstructing of high-level objects it is not usable for a physics analysis. We make only use of the CDF specific software to reconstruct all objects needed like electrons, muons, jets.

4.2 TopEventModule

After the processing and the reconstruction of the raw data or the simulated Monte Carlo data to get to the low level objects, e.g clusters, tracks, we run the `TopEventModule` [37]. The `TopEventModule` is the standard method of the Top and ElectroWeak physics groups at CDF for the selection of event samples and the classification of electrons, muons, jets and missing transverse energy. The `TopEventModule` is an AC++ module and uses the AC++ Run II objects (`EdmObjects`).
In order to find an efficient way of looking into data outside the AC++ framework of CDF, the `TopNtuple` has been introduced [38]. The `TopEventModule` writes the data out in an extended ntuple, the so called `TopNtuple`. In fact, the `TopNtuple` is a micro-DST CDF data format. The reconstructed data are written into several branches of a ROOT-Tree. To assist the user to access the data easily, the so-called `HighLevelObjects` are introduced. Using the `HighLevelObjects` the complete information of one event can be accessed via different classes. The CDF II framework uses a special Fermilab version of ROOT[1]. Being based on ROOT, the user can use all the power of ROOT analysis tools. Thus it is possible to run the whole analysis with ROOT on executing scripts that are compiled on the fly by the ROOT script compiler. Furthermore, the user profits from the knowledge of many existing analysis scripts, e.g. is able to fill histograms and to apply fits.

[1] Version 3.05/04

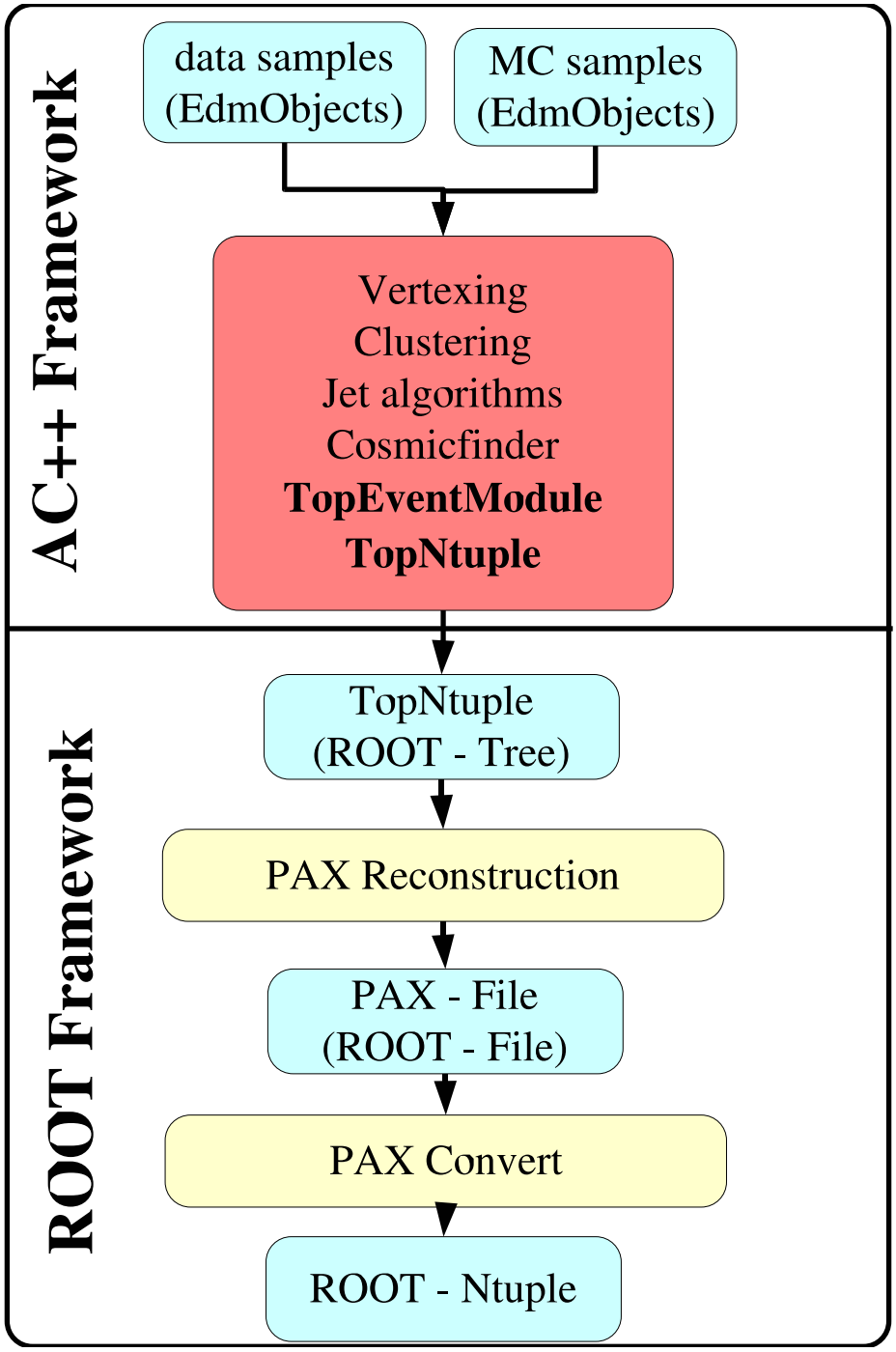

Figure 4.1: Different stages of reconstruction. Each event is forwarded from top to bottom. ROOT Framework means that different classes of ROOT package are used.

4.3 Physics Analysis eXpert (PAX)

PAX is a new C++ toolkit for the analysis of elementary particle interactions. It has been developed at University of Karlsruhe by M. Erdmann et al. and provides a new level of abstraction in particle physics analysis beyond detector reconstruction [39]. It helps large teams to reduce dependencies on the details of the underlying experiment specific software. This enables physicists to share analysis code among different experiment software environments easily. With this, the specific analysis code is protected against changes in the detector reconstruction and enables users to comparably quickly answer physics questions. If changes occur, only the interface needs to be updated while the actual analysis code remains untouched.

The idea of PAX is based on similar projects like H1PHAN [40] and ALPHA [41] of the H1 and the ALEPH experiment that have been developed in the past. They were used in experiments with e^+e^- and ep physics and were used to provide an almost complete view of the originating events.

Since the experiments for both the present and the near future in high energy physics are hadron colliders - either $p\bar{p}$ at Fermilab or pp at the future LHC - the challenge is to deal with many simultaneous collisions in one triggered event. This implies a large number of possible interpretations of the triggered events. Large event sizes require the analysis of dedicated regions of interest.

4.3.1 Design guidelines

The PAX toolkit is a data analysis utility designed to assist physicists in the tasks in the phase between detector reconstruction and physics interpretation of an event, see figure 4.2.

The design of this next generation physics analysis utility has been developed

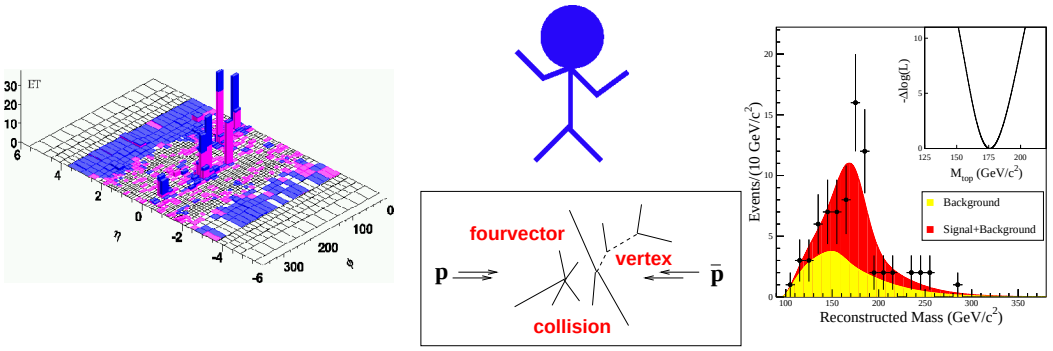

Figure 4.2: Application area of the PAX toolkit. Helping the user to go from detector output to physics interpretation of an event [42].

according to the following guidelines:

- The package is a utility tool box in a sense that the user has full control of every step in the program execution.
- The programming interface should be as simple and intuitive as possible. This minimizes the need to access the manual and thereby increases the acceptance in the community. Furthermore simplicity enables also physicists with limited time budget or limited knowledge of object oriented programming to carry out complex physics analysis.
- The package supports modular physics analysis structures and thus facilitates team work. The complexity of today's and future analyses makes team work of many physicists mandatory.
- Existing physics analyses can be connected. Examples are tools for dealing with fourvectors which are available in general form, other examples are histograming, fitting routines etc.
- The physics analysis package can be used consistently among different high energy physics experiments.
- Frequently used cases have already been taken care of. The following list is certainly not complete:
  - Access to the original data of the experiment is possible at each stage of the analysis.
  - When studying events of a Monte Carlo generator, relations between generated and reconstructed observables are accessible at any stage of the analysis.
  - Without significant code changes, a complete analysis chain can be tested with different input objects such as reconstructed tracks, generated particles, etc.
  - Relations between reconstructed physics objects (tracks, muons, etc.) and vertices are available, as well as hooks for separating multiple interactions.
  - The decay chain with secondary, tertiary etc. vertices can be handled in events with multiple interactions.
  - Information of different objects can be combined, e.g. tracks and calorimeter information.
  - A common challenge in data analysis are reconstruction ambiguities which need to be handled. Administration of this is supported.
  - The user finds assistance in developing analysis factories where multiple physics analyses are carried out simultaneously.

For the convenience of connecting to other packages, C++ was the language of choice for the realization of PAX.

4.3.2 Technical details

Basic unit of PAX

The basic unit in PAX is a class called `PaxEventInterpret`. Each `PaxEventInterpret` stores a distinct interpretation of the event currently analysed.

It contains three physical objects (see figure 4.3)

- fourvectors,
- vertices, and
- collisions.

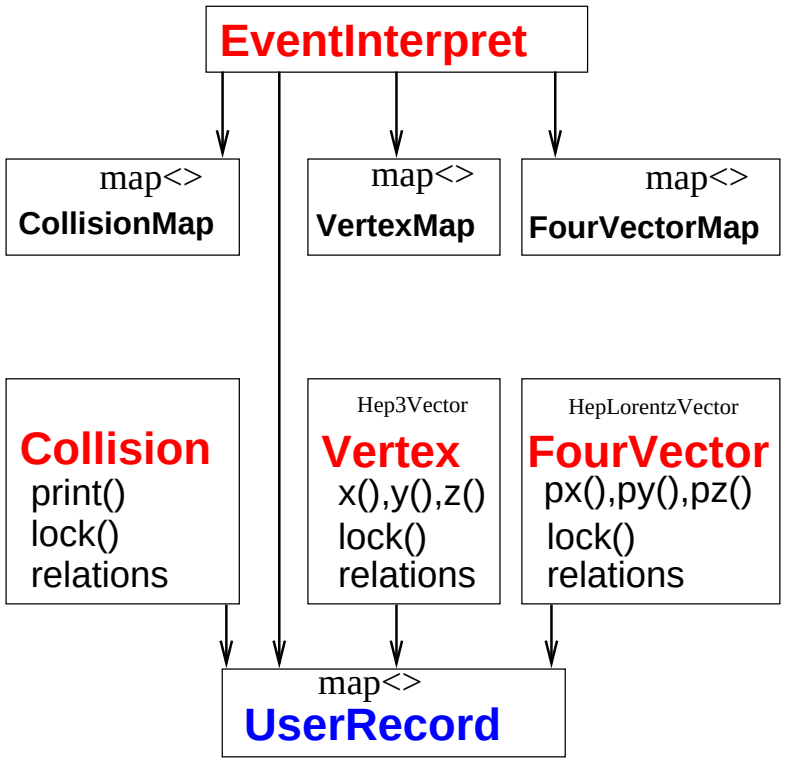

Figure 4.3: The basic unit in PAX, the `PaxEventInterpret` contains maps for PaxFourVectors, PaxVertices and PaxCollisions.

Three classes have been defined correspondingly. The class `PaxCollision` provides the hooks to handle multi-collision events. Vertices and fourvectors are defined through the classes `PaxVertex`, and `PaxFourVector`. Since the user may need to impose vector operations on them, both PAX classes inherit either from the CLHEP classes `Hep3Vector` and `HepLorentzVector`, respectively or from the ROOT classes `TVector3` and `TLorentzVector`, respectively depending on the chosen framework for the analysis. Changing between the two possibilities

is possible with a compiler switch. The `PaxVertex` and `PaxFourVector` classes contain additional functionality which mainly result from features proven to be useful in the previously mentioned H1PHAN package.
For all physics quantities the user can store additional values (data type double) needed by the analysis via the class `PaxUserRecord`. These values are registered together with a key (data type string functioning as a name), which must be given by the user.

The user books, fills, draws, copies, advances the event interpretation, and has the ultimate responsibility for deleting it. When the user finally deletes an instance of PaxEventInterpret, instances of objects which have been registered with this event interpretation - collisions, vertices, fourvectors, etc. - are also removed from the memory.

A copy of an event interpret is a physical copy of the memory. It is generated preserving all values of the original event interpretation, and with all relations between collisions, vertices and fourvectors corrected to remain within the copied event interpretation. In addition, the histories of the individual collisions, vertices and fourvectors are recorded. The copy functionality simplifies producing several similar event interpretations. This is advantageous typically in the case of many possible views of the event that differ in a few aspects only. Beside the features mentioned, the `PaxEventInterpret` also defines an interface to algorithms such as jet algorithms, missing transverse energy calculations etc. This eases the exchange of algorithms within or between analysis teams.

Relation management

The relations between the physics objects are managed by a separate class called `PaxRelationManager`. An illustration of the different relations between the objects is shown in figure 4.4. Here we followed the design pattern Mediator [43]. Examples for relations to be handled between physics quantities are fourvectors which originate from the primary vertex, an incoming fourvector to a secondary vertex, or connections between multiple collisions and their vertices etc.
If an object is copied, the relation manager stores a pointer to the original instance in the relations of the corresponding object. Thus it is possible to record both the decay tree and the history of the objects and to trace it back by iterating over the objects relations. Another sophisticated feature PAX provides is its lock mechanism. It allows to exclude parts of an event interpretation from the analysis. An example would be a lepton which needs to be preserved while applying a jet algorithm. This locking mechanism is build in the form of a tree structure which enables sophisticated exclusions of unwanted event parts. For example, locking a collision excludes the vertices and fourvectors connected to this collision (figure 4.5). In the case of locking the secondary vertex, PAX will

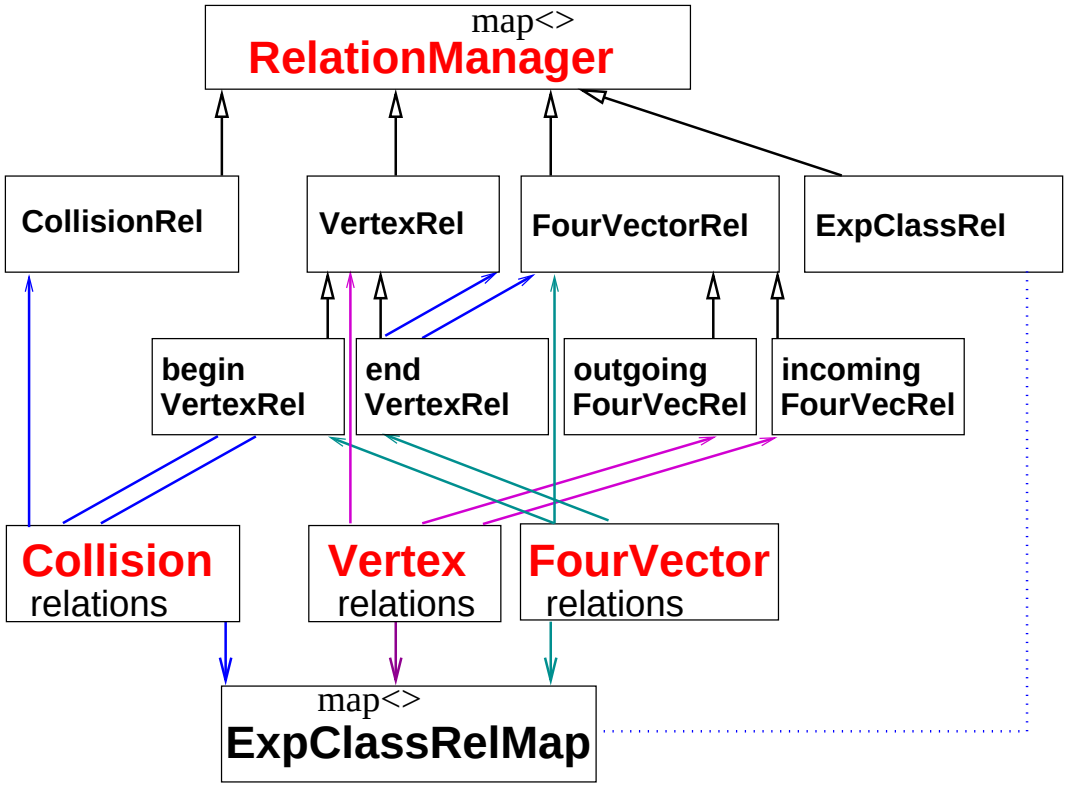

Figure 4.4: The relations in PAX enable storage of decay trees, records of analysis history, access to experiment specific classes, and exclusion of parts of the event from the analysis.

lock the decay tree starting at this vertex.

For some applications, the user may want to inquire additional information on a physics quantity which is only contained in an experiment specific class. An example is a `PaxFourVector` instance originating from a track of which the user wants to check the χ^2 probability of the track fit. The relation manager allows to register instances of experiment specific classes which led to a `PaxCollision`, `PaxVertex` or `PaxFourVector` instance. To enable such relations, a template class `PaxExperiment<>` has been defined which allows registering of arbitrary class instances. Applying the C++ *dynamic−cast* operator, the user can recover the original instance, and access all member functions of the experiment specific class.

The class design and documentation as well as further information and examples for the usage of PAX are available on a web page [44].

Container and Iterator

PAX uses the template class *map* <> from the Standard Template Library (STL) [45] to manage pairs of keys and items in a container. The user record

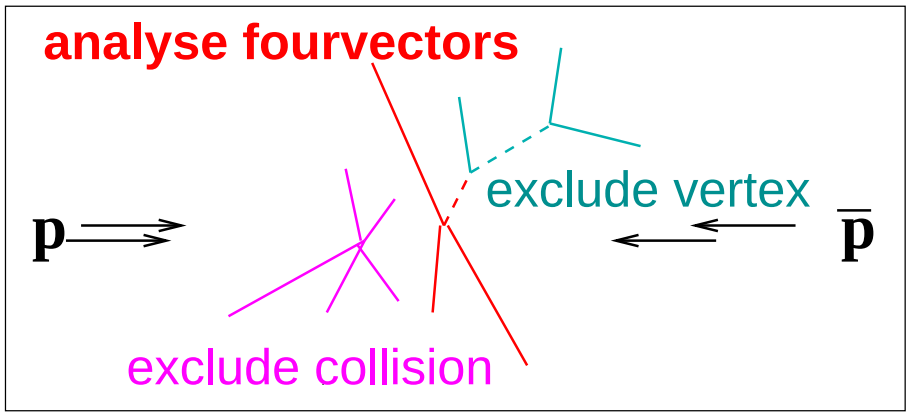

Figure 4.5: Excluding a collision (left) or a vertex (right) from an analysis using the lock mechanism excludes all vertices and fourvectors originating from the excluded object.

in figure 4.3 is an example of such a container for pairs of data type *string* and *double*. For accessing a certain item, optimized STL algorithms search the *map* for the corresponding key and provide access to the item.
All `PaxCollision`, `PaxVertex` and `PaxFourVector` instances carry a unique identifier of type `PaxId` which is used as the key in the `PaxCollisionMap`, `PaxVertexMap` and `PaxFourVectorMap` of an event interpretation. Pointers to the collision, vertex and fourvector instances are the corresponding items. In this way, fast and uniform access to the individual physics quantities is guaranteed.
For users not familiar with STL iterators, we provide the `PaxIterator` class which gives a simple and unified command syntax for accessing all containers in PAX.

Input/Output to/from disk files

One of the main advantages of PAX is the possibility to store PaxEventInterprets on hard disk. These objects can then be analyzed with a stand alone PAX analysis. This results in an enormous gain of speed, since the writing and the reading of Pax files is very fast, being based on the well approved ROOT I/O format. Furthermore, all the unused and time consuming interactions with the experiment specific software can be avoided. For example, it is possible to create a subset of events that pass certain cut criteria in a separate file and to proceed the analysis with this subset. In principle, the complete decay trees and analysis history including all relevant objects and their relations can be stored.
Storing all relevant PaxEventInterprets in a `PaxFile` opens an easy way to convert important data to a ROOT ntuple. By iterating over the PaxEventInterprets and their objects, important data for the analysis can be added to the ntuple. The ntuple then allows to test different cut scenarios on the stored vari-

ables interactively in the CINT environment of ROOT without reprocessing the complete events.

4.3.3 Complete Reconstruction of a partonic process in PAX

Having filled reconstructed data like tracks or calorimeter towers from the experiment's database into PAX, the actual analysis begins. Now, the different possibilities to interpret an event need to be considered. For complex analyses, where intermediate decay products have to be reconstructed, the number of interpretation alternatives may reach several hundreds. To handle this difficult task, a class called `PaxEventClass` implements the basic functionality of the reconstruction of an event. It is a generic class that manages the combinatorics in a way that every possible and reasonable combination of objects is stored in a `PaxEventInterpret`. The different interpretations are then stored in a map of the Standard Template Library (STL). In fact, the `PaxEventClass` is a map, i.e. it inherits from the STL map.
To each `PaxEventInterpret` that is created during the reconstruction of the `PaxEventClass` an event interpretation quality is assigned, depending both on the demands of the user and the physics process that is analyzed. It is possible to derive own event classes, inheriting from `PaxEventClass`.

In figure 4.6 one can see a schematic $W \rightarrow e\nu$ - reconstruction starting with electron identification and calculation of the missing transverse energy from calorimeter tower energies. In the first step we loop over all electron fourvectors getting from the reconstruction software and apply electron ID cuts. For each electron passing the cuts we loop over the track event interpretations and connect the appropriate track to the electron. Only electron fourvectors which passed the cuts are stored in the electron event interpretation common with the remaining calorimeter towers. The second step is creating jets by using a jet algorithm which uses the remaining calorimeter tower as input. The calorimeter tower belonging to the identified electron is locked, so that the jet algorithm does not use it. The third step is calculating the missing transverse energy ($\not\!\!E_T$). This is done by iterating through all jets and remaining calorimeter towers and summing up all fourvectors. With the $\not\!\!E_T$ and ϕ of the missing transverse fourvector one can get the p_z value of the neutrino using the W boson mass constraint, see Appendix B.1. The mass constraint leads to a quadratic equation. This ambiguity is reflected in two interpretations of the reconstructed W, meaning the two solutions are stored in parallel in different PaxEventInterpretations.

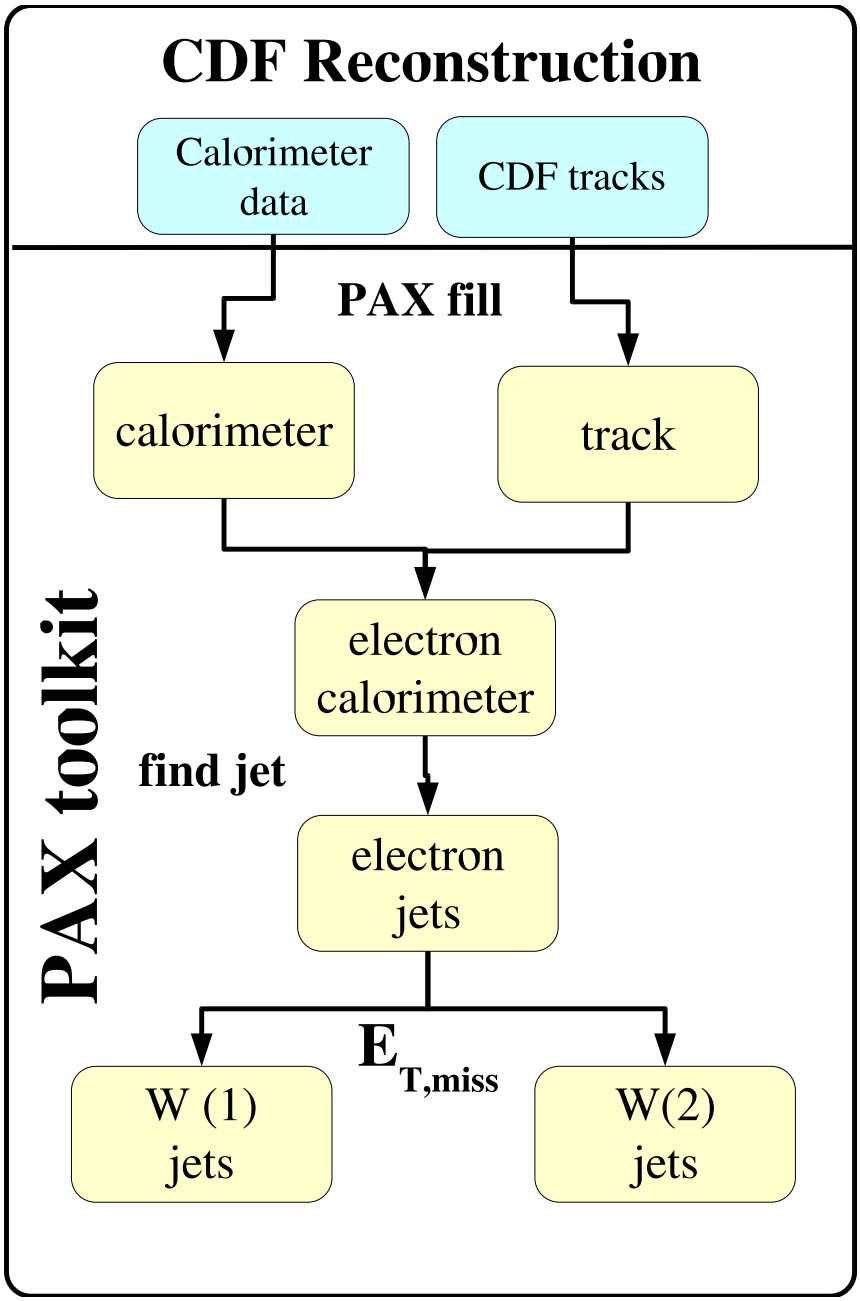

Figure 4.6: Example W reconstruction within PAX starting from tracks and calorimeter towers. Each button within PAX represents one `PaxEventInterpret`.

Chapter 5

Development and Verification of the Reconstruction of the $t\bar{t}$ process

In this chapter we will develop and verify our analysis method. We will first explain the event selection, which is common for the most $t\bar{t}$ analyses in the lepton plus jets channel within the CDF experiment. The event selection is based on the selection of high p_T leptons, jets, missing transverse energy, some global variables and vetoes, and follows the suggestion of the CDF lepton + jets group for CDFSOFT version 5.3.3. Having selected $t\bar{t}$ candidates we develop our reconstruction of the partonic $t\bar{t}$ process with a Monte Carlo sample. Since we have to deal with a lot of ambiguities during the reconstruction we have to develop a selection procedure. In the end we will compare our selection procedure with the standard one of the CDF Top Group, the kinematic fitter.

5.1 Event selection

Top quark events in the lepton plus jets channel are characterized by a high-momentum lepton and substantial missing energy due to the leptonic W decay, and a number of high-energy hadronic jets due to the hadronic W decay and the two b quarks from each top quark decay in the event.
In the electron channel both central (CEM) and plug electrons, called phoenix (PHX) electrons are identified. In the muon channel, we use CMUP and CMX muons. Given that all of the events will include a high-momentum lepton or muon, the data sample will be built from events that came in on CEM, CMUP or CMX triggers, explained in detail in section 3.1. The remaining selection criteria for leptons are listed in detail in section 5.1.1. Electron events where the primary electron is identified as a conversion, i.e. where a photon has converted into an electron and a positron, and muon events containing cosmic rays are removed.

The signal events should have only one single high-p_T lepton, backgrounds such as Z production and $t\bar{t}$ di-lepton production can produce two leptons. Therefore di-leptons are rejected by requiring that an event has more than one isolated lepton in the CEM, PEM, CMUP and CMX. In addition, to reduce the Z background, events where the tight lepton and a second object forms an invariant mass within a window of the Z mass will be removed. These general cuts are described in section 5.1.4. Jets are reconstructed using a cone algorithm and corrected for different effects which are described in section 5.1.2. Correcting the energy of the jets imply also a correction of the transverse missing energy, see 5.1.3. To ensure good quality event reconstruction, the difference between the event z-vertex, defined as the z-vertex closest to z_0 of the tight lepton is required to be small.

5.1.1 Lepton identification

The high-p_T lepton identification follows the suggestion of the lepton+jets group [46, 47].

Electron identification

The baseline cuts for CEM electrons are given in table 5.1 and cuts for phoenix electrons, which are only used to veto dilepton events, are given in table 5.2. The considered variables for **central electrons** are:

- $\mathbf{E_T}$: Transverse momentum of the calorimeter energy.
- $\mathbf{p_T}$: Transverse momentum of the associated track.
- $\mathbf{E_{had}/E_{em}}$: Ratio of the hadronic calorimeter energy to the electromagnetic calorimeter energy using all towers involved.
- $\mathbf{L_{shr}}$: The lateral shower profile is defined as $L_{shr} = 0.14\frac{\Sigma_i(M_i-P_i)}{\sqrt{(0.14\sqrt{E_{EM}})^2+\Sigma_i(\Delta P_i)^2}}$ where the sums are over the towers in the electromagnetic cluster adjacent to the seed tower and in the same wedge as the seed tower. M_i is the measured energy in an adjacent tower, P_i is the predicted energy deposit in the adjacent tower, E_{EM} is the total electromagnetic energy in the cluster, and ΔP_i is an estimate of the uncertainty in P_i.
- $\mathbf{E/P}$: Electromagnetic calorimeter energy divided by the momentum of the maximum p_T matched track.
- $|\mathbf{z_0}|$: Distance between z_0 of the maximum p_T matched track and the coordinate system origin.

- $|\mathbf{\Delta z}|$: Distance between z_0 of the maximum p_T matched track and the event z position.
- $\mathbf{Q \cdot \Delta x}$: Distance, signed by the track charge, between the x position of the CES wire cluster, and the x position of the extrapolation to the CES of the maximum p_T matched track. This is corrected for CES-COT misalignment.
- $\chi^2_{\mathbf{strip}}$: Quality of the match of the shower shape for the best matching CES strip cluster with that expected for an electron.
- **Isolation:** is defined as the energy in a cone with radius of 0.4 around the seed tower divided by the total energy of the cluster corrected by the leakage energy.
- **Good COT Axial Segments:** Number of track segments with at least 6 hits in the COT axial super-layers for the maximum p_T matched track
- **Good COT Stereo Segments:** Number of track segments with at least 6 hits in the COT stereo super-layers for the maximum p_T matched track
- **Hits for a good COT segment:** Number of required hits.
- **Fiducial:** means that the electron has to be within the fiducial volume of CEM towers. Tower 9 and chimney, the exhaust of the cabling in tower 7 are removed. Additionally a matched CES strip cluster and a matched CES wire cluster are required.
- **Conversion:** Check if the electron comes from a photon conversion. Conversions are oppositely charged electron-track pairs with similar directions and small separation in the x-y plane. Trident events, where electrons have radiated a photon which then converts, are kept as good electrons.

The cut variables for the plug electrons, called **phoenix electrons**, because of the special tracking in the forward region developed by the phoenix group, are:

- $\mathbf{E_T}$: This uses the energy and directions of the electromagnetic calorimeter cluster, where the z position is taken as that of the highest p_T good quality `ZVertex` object. The direction of any matched track is not used.
- $\mathbf{E_{had}/E_{em}}$: Ratio of the hadronic calorimeter energy to the electromagnetic calorimeter energy using all towers included.
- **Towers in χ^2 fit:** Calorimeter towers used in fit.
- **PEM 3 x 3 χ^2:** Quality of match of energy sharing in a 3x3 tower grid centered on the seed tower with that expected for an electron.

Central Electron Variable	Cut	`TNtuple`
E_T	≥ 20.0 GeV	`Et`
p_T	≥ 10.0 GeV	`TrkPt`
E_{had}/E_{em}	$\leq 0.055 + 0.00045 * E$	`Hadem`
L_{shr}	≤ 0.2	`LshrTrk`
E/P	≤ 2.0 unless $p_T \geq 50$ GeV	`EP`
$\|z_0\|$	≤ 60.0 cm	`TrkZ0`
$\|\Delta z\|$	≤ 3.0 cm	`DeltaZ`
$Q \cdot \Delta x$	≥ -3.0 cm and ≤ 1.5 cm	`Charge, DeltaX`
χ^2_{strip}	≤ 10.0	`StripChi2`
Isolation	≤ 0.1	`Isol`
Good COT Axial Segments	≥ 3	`TrkAxSeg`
Good COT Stereo Segments	≥ 2	`TrkStSeg`
Hits for a good COT segment	≥ 5	
Region	0	`Region`
Fiducial	Yes	`Fiducial`
Conversion	Veto	`Conversion`

Table 5.1: The baseline cuts for **central electrons**. Variables given in the `TNtuple` column are members of the `electron` class of the `HighLevelObjects`.

- **PES cluster 5 x 9 ratio:** In the PES, the seed strip of a cluster is the one with the most energy. By default clusters have 9 strips with the seed strip at the center. The 5/9 variable is defined as the energy in the middle 5 strips divided by the energy in all 9 strips of the cluster.
- **PES $|\eta|$:** η of pre-shower cluster.
- **Number PES clusters:** Number of pre-shower clusters.
- **ΔR PEM-PES:** Distance in the $\eta - \phi$ - plane ($\sqrt{\Delta\phi^2 + \Delta\eta^2}$) between the signal in the plug electromagnetic calorimeter cluster and the best matching pre-shower cluster.
- **Phoenix match:** Match between reconstructed phoenix track and calorimeter tower.
- **Track $|\mathbf{z_0}|$:** Distance between z_0 of the maximum p_T matched track and the coordinate system origin.

- **Isolation:** Total excess energy within a cone radius $\Delta R = 0.4$ about the electromagnetic centroid, divided by the electron transverse energy. Corrected for leakage if electron is near tower boundary.
- **Number PHX Si hits:** Number of collected hits of the track in the silicon detector.

Plug Electron Variable	Cut	`TNtuple`
E_T	≥ 20.0 GeV	`Et`
E_{had}/E_{em}	≤ 0.05	`Hadem`
Towers in χ^2 fit	≥ 1	`Pem3x3FitTow`
PEM 3 x 3 χ^2	≤ 10.0	`Pem3x3Chisq`
PES U cluster 5 x 9 ratio	> 0.65	`Pes2d5by9U`
PES V cluster 5 x 9 ratio	> 0.65	`Pes2d5by9V`
PES $\lvert\eta\rvert$	$1.2 < \lvert\eta\rvert < 2.0$	`Pes2dEta`
Number PES clusters	≥ 1	`NumPes2d`
ΔR PEM-PES	≤ 3 cm	`Pem3x3DetEta, Pem3x3Phi`
		`Pes2dX, Pes2dY`
Isolation	≤ 0.1	`Isol`
Phoenix match	Yes	
Track $\lvert z_0\rvert$	≤ 60.0 cm	`TrkZ0`
Number PHX Si hits	≥ 3	`TrkSiHits`
Region	PEM	`Region`
Fiducial		`Fiducial`

Table 5.2: The baseline cuts for **plug electrons** using the phoenix tracking. Variables given in the `TNtuple` column are members of the `electron` class of the `HighLevelObjects`.

Muon Identification

The baseline cuts for **muons** are given in table 5.3. The detailed description of the cut variables are:

- $\mathbf{p_T}$: Transverse momentum of the corresponding track.
- $\mathbf{E_{had}}$: Energy deposition in the hadronic calorimeter.

- $\mathbf{E_{em}}$: Energy deposition in the electromagnetic calorimeter.
- $|\mathbf{z_0}|$: Distance between z_0 of the maximum p_T matched track and the coordinate system origin.
- **CMU/ CMP / CMX $|\Delta\mathbf{x}|$:** Distance in $r\phi$ between the stub direction and the track extrapolation to the stub.
- $|\mathbf{d_0}|$**:** If track did not use silicon hits, this cut is applied on the 2-D impact parameter of best matched track with respect to the COT beam spot position, if track did use silicon hits with respect to the SVX beam spot position.
- **Isolation:** Total excess energy within a cone of radius $\Delta R = 0.4$ about the muon divided by the transverse momentum of the muon.
- **COT exit radius:** The COT exit radius check ensures that the muon passes through all 4 axial layers of the COT and could trigger the event.

Central Muon Variable	Cut	`TNtuple`
p_T	≥ 20.0 GeV	`PtCorr`
E_{had}	$\leq max(6; 6 + 0.0280(p - 100))$ GeV	`HadEnergy`
E_{em}	$\leq max(2; 2 + 0.0115(p - 100))$ GeV	`EmEnergy`
$\|z_0\|$	≤ 60.0 cm	`Z0`
CMU$\|\Delta x\|$	≤ 3.0 cm	`CmuDx`
CMP$\|\Delta x\|$	≤ 5.0 cm	`CmpDx`
CMX$\|\Delta x\|$	≤ 6.0 cm	`CmxDx`
$\|d_0\|$	≤ 0.2 cm if no Si hits	`D0`
$\|d_0\|$	≤ 0.02 cm if Si hits	`D0`
Isolation	≤ 0.1	Isol
Good COT Axial Segments	≥ 3	`TrkAxSeg`
Good COT Stereo Segments	≥ 2	`TrkStSeg`
Hits for a good COT segment	≥ 5	
Fiducial requirements		
CMUP	CMUFidX < 0 cm, CMUFidZ < 0 cm	`CmuFidX, CmuFidZ`
	CMPFidX < 0 cm, CMPFidZ < -3 cm	`CmpFidX, CmpFidZ`
CMX	CMXFidX < 0 cm, CMXFidZ < 0 cm	`CmxFidX, CmxFidZ`
	COT exit radius > 140 cm	`Eta, Z0`

Table 5.3: The baseline cuts for **CMUP and CMX muons**. Variables given in the `TNtuple` column are functions of the `muon` class of the `HighLevelObjects`.

5.1.2 Jet Reconstruction

Jets are identified by the JETCLU algorithm as a cluster of energy within a cone of R=0.4 in the $\eta - \phi$-plane using the event z vertex. Calorimeter towers belonging to any tight isolated electron are removed before clustering the jets. Jet corrections are required to have the energy scale in the data match the energy scale in the simulation. For counting purposes we correct all jets with level 4 with the CDF jet correction package[1] and accept jets with corrected $E_T > 15$ GeV and $|\eta| < 2.0$, called tight jets. For our analysis we require a minimum of four tight jets in the event. To estimate the energy of the underlying parton necessary for complete reconstruction of the top quark, jets forming a top quark are corrected with level 7 correction. In the following we will discuss the different correction levels in detail, where the higher levels include all previous levels [49]. A schematic view of detector jets originating from the scattered partons can be seen in figure 5.1.

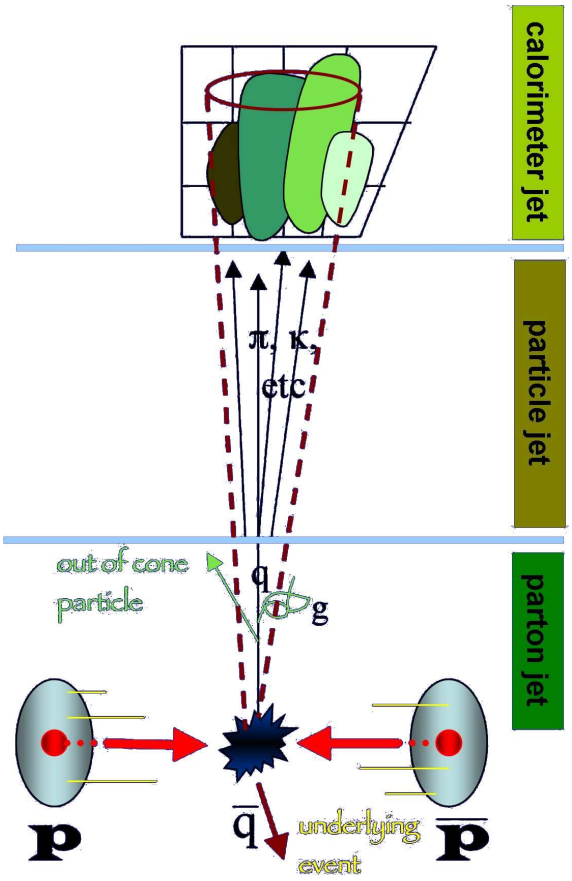

Figure 5.1: Schematic overview of jet reconstruction.

[1] JetUser package version 04b

L. 1: **Relative Energy Corrections (Make response uniform in η)** Since the central calorimeters are better calibrated and understood, this correction scales the forward-calorimeters to the central calorimeter scale. The transverse energy of the two jets or the energy of photon and jet in a $2 \rightarrow 2$ process should be equal. This property can be used to scale jets outside the $0.2 < |\eta| < 0.6$ region to jets inside this region. This region is used, because there are no cracks or un-instrumented regions. The calorimeter response before and after correction as a function of η is shown in figure 5.2. The cracks of the calorimeter at $\eta = 0$ and $|\eta| = 1$ can be easily seen. More details can be found in ref. [50].

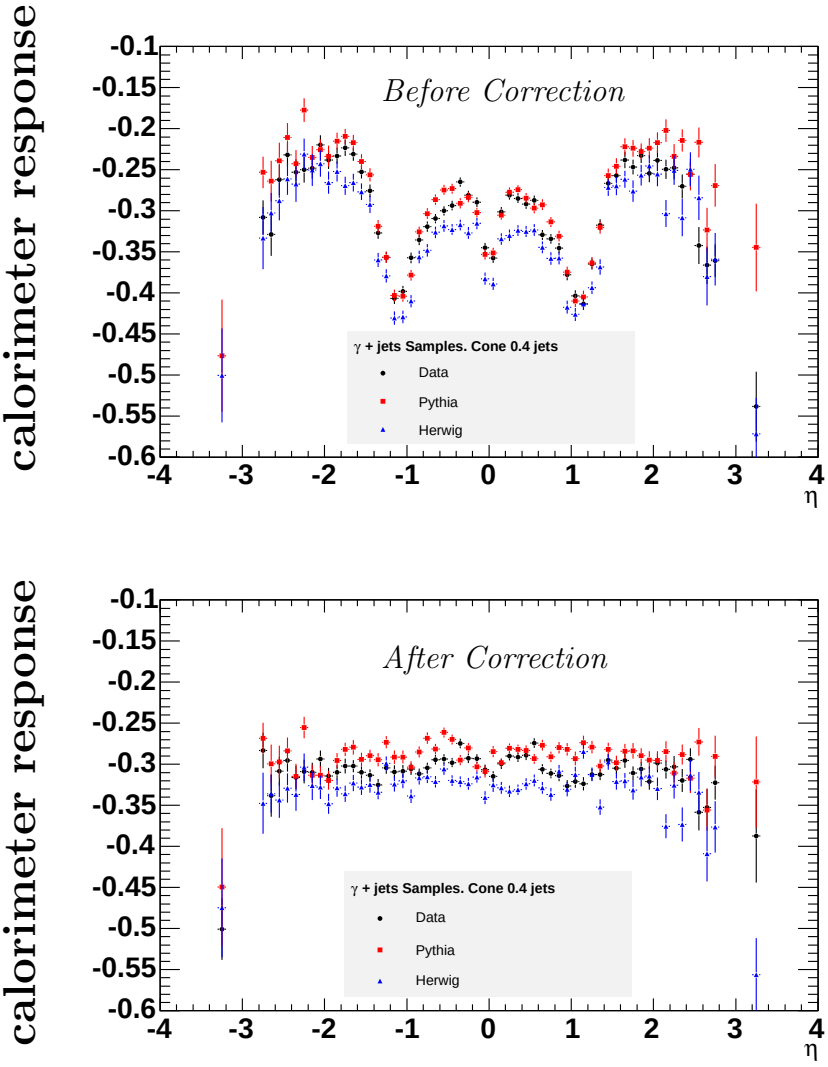

Figure 5.2: Calorimeter response of photon-jet events from data and Monte Carlo samples as a function of the pseudorapidity η before and after correction.

L. 2: **Not in use**

L. 3: **Not in use**

L. 4: **Multiple Interaction Corrections** All energies from different $p\bar{p}$ interactions during the same bunch crossing contribute to the same jet cluster, increasing the energy of the measured jet. The correction is parameterized as a function of the number of vertices in the event and derived from minimum bias data, see figure 5.3.

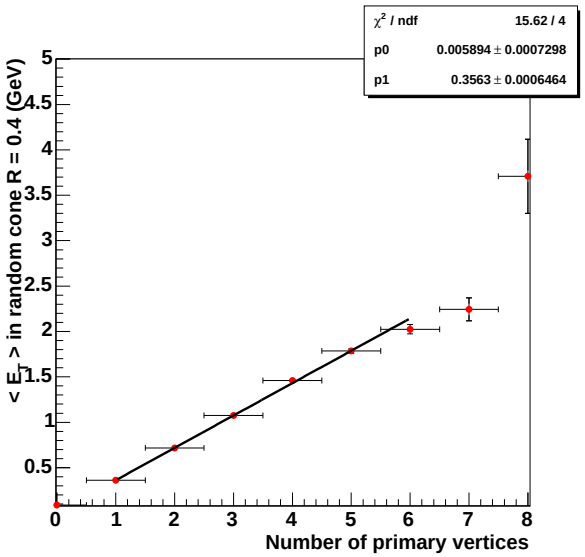

Figure 5.3: Average energy in a random cone with $R = 0.4$ as a function of number of primary vertices.

L. 5: **Absolute Energy Corrections (From calorimeter energy to particle energy)** They correct the jet energy observed in the calorimeter to the P_t sum of the particles within the cone of same size around the parton direction which matched the jet direction with $\Delta R < 0.5$. The correction factor is parameterized separately for jets below and above 100 GeV. (See figure 5.1: transition from calorimeter jet $\rightarrow$ particle jet.)

L. 6: **Underlying Energy Corrections** This correction subtracts the underlying energy from the particle-level jet energy. The underlying event energy was measured from minimum bias data and corrected for calorimeter response [51].

L. 7: **Out of Cone Corrections (From particle level-jet to parton energy)** This correction corrects the particle-level energy for the radiations outside the clustering cone, taking the "jet energy" back to "parent parton energy", the correction factor as a function of p_T of the jet is given in figure 5.4.

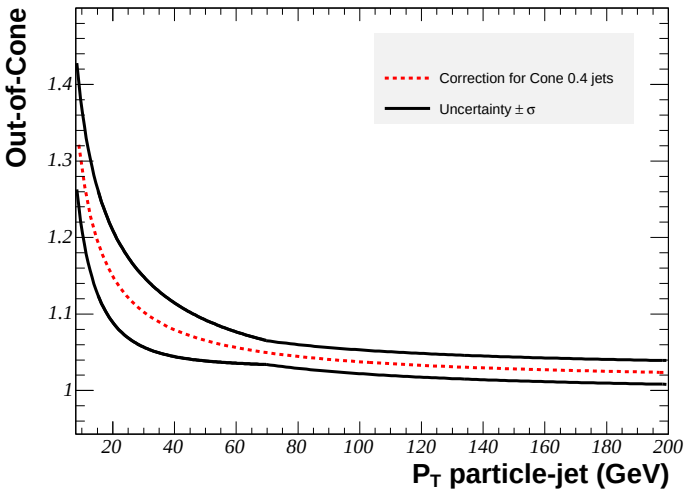

Figure 5.4: Out-of-cone correction for jets with cone of 0.4.

5.1.3 Missing Transverse Energy ($\not\!\!E_T$)

The $\not\!\!E_T$ variable provided in the `TopSummary` object [37] is re-calculated using the event z vertex. The missing transverse energy is corrected for any tight muons in the event in the following way: the muon p_x and p_y components are subtracted and, to avoid double-counting, the energy deposits left by the muon in calorimeter towers are added on a tower-by-tower basis. This is already done in the `TopEventModule`. For the identified isolated muon, the muon contribution to the $\not\!\!E_T$ is replaced by that from the muon track with the curvature correction for COT misalignment. During the analysis additional corrections have to be done. $\not\!\!E_T$ is also corrected for all jets with $|\eta| < 2.4$ and level-4-corrected jet energy > 8 GeV. This is done by adding the original (uncorrected) quantities $p_{T,jet,uncorr}$ back into the $\not\!\!E_T$, and then subtracting the new (corrected) quantities $p_{T,jet,corr}$.

$$E_{T,miss\,corr} = \sum_{i}^{Njets} (p_{T,jet,uncorr} - p_{T,jet,corr}) \tag{5.1}$$

For the event selection jets with level 4 correction are used to calculate the corrected $\not\!\!E_T$. We only accept events with $\not\!\!E_T > 15$ GeV. For top quark reconstruction the corrected $\not\!\!E_T$ is calculated with level 6 corrected jets.

5.1.4 Global Variables

Di-lepton veto

To ensure that there is exactly one tight lepton we reject events which have one primary (tight) lepton and one secondary (tight or loose) lepton. The loose

leptons are defined by the dipleton group [48].

Z boson veto

Events are removed if the tight lepton and a second object forms an invariant mass within a window of the Z mass. The default window is [76,106] GeV. For electrons, the other object can be an electromagnetic object, a reclustered jet or an opposite-signed track with various loose requirements on it. For muons, the other object can be an opposite-signed minimum-ionizing track with various loose requirements on it.

Event z position

The z vertices in the `ZVertexModule` are determined by the following algorithm. The inputs are pre-tracking vertices which have high efficiency but high fake rate. This seeds are "cleaned-up" by requiring a certain number of tracks with $p_T > 300MeV$ associated to them. A track is associated to a vertex if it is within 1 cm (5 cm) of silicon standalone vertices (COT standalone vertices). The position of the vertex is obtained by weighting the z_0 of the tracks (corrected for beamline offset) with their error. For data, we use the closest z vertex with at least two good COT tracks to the maximum-E_T tight lepton. If no good quality vertex exists, then we use the z_0 of the tight lepton.

5.1.5 b tagging

Since in the $t\bar{t}$ signal process two b quarks are produced, it is necessary to identify b quark jets effectively. We use two different tagging algorithm for different purpose. We need one very pure algorithm to reduce background. Therefore we use the so called *secondary vertex tagger* (SECVTX) [52], which gives a digital decision tag or no tag. This algorithm has very high purity but also reduces the event numbers of the signal sample significantly. We require at least one tagged jet in our event selection.
To deal with the ambiguities of the different assignments of the jets to the top quarks we make use of another algorithm. This algorithm called *jet probability* provides a continuous variable, which indicates the probability of a jet fitting to the primary vertex.

SECVTX tag

The idea behind the b tagging is that bottom quarks hadronize, and then travel an observable distance before decaying. The average track multiplicity of a B hadron decay is approximately 5. Due to the long B hadron lifetime, these

tracks will have a measurable impact parameter. b jets coming from top quark decays at the Tevatron have an average p_T of the jets of around 65 GeV/c. The lifetime of a B hadron is, on average, 1.5 picoseconds. Therefore, the average distance traveled before decaying is approximately 7.5 millimeters. As shown in figure 5.5, tracks in a secondary vertex will have a large impact parameter (d_0), or perpendicular point of closest approach, with respect to the primary vertex. For B hadrons this value is on average 450 μm. The b tagging algorithm, SECVTX, looks for tracks in the cone of each jet that are displaced from the primary vertex. Tracks must have a minimum number of silicon hits, and $|d_0| \leq 0.3$ cm to be considered "good". If there are at least two good tracks in the jet the jet is then labeled "taggable", because a minimum of two tracks are required to form an intersection, or displaced vertex. If there are at least two of these displaced tracks in the jet the tagging algorithm attempts to fit these tracks to a common vertex. As a final step the tagging algorithm examines the distance between the primary and secondary vertex in $r - \phi$ plane, L_{xy} . The L_{xy} cut requires the significance L_{xy}/σ_{xy} of the displacement to be ≥ 3. Jets having vertices which pass this L_{xy} requirement are b tagged.

The per-event efficiency to tag jets in $t\bar{t}$ events is taken from a Monte Carlo

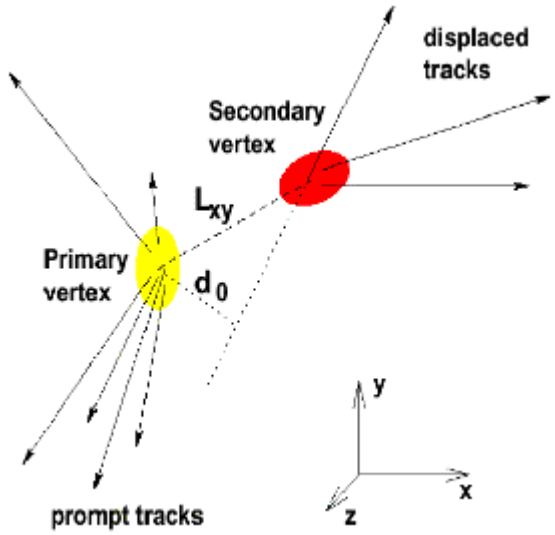

Figure 5.5: Schematic view of a secondary vertex with impact parameter $d0$ and decay length L_{xy}.

sample. Of primary interest, however, is the tagging efficency in $t\bar{t}$ data events. This can be measured in a b enriched data sample. Unfortunately, no data sample which can be used to model the b tagging efficiency in top quark events, where the p_T of the b jets is very high, is available. To determine the per-event tagging efficiency in $t\bar{t}$ data events the tagging efficiency is determined in a Monte Carlo and calibrated by a single multiplicative factor using the b enriched

data sample. A detailed description is given elsewhere [53]. In figure 5.6 the dependence of the b tag efficiency from p_T and η of the jet is shown. For softer jets with p_T values smaller than 40 GeV/c the efficiency is between 0.3 and 0.4. For jets with p_T values greater 40 GeV/c the efficiency is staying relatively stable at 40 %. The dependence on η is correlated with the acceptance of the silicon detector, which covers $|\eta| < 1$. The last important value concerning the

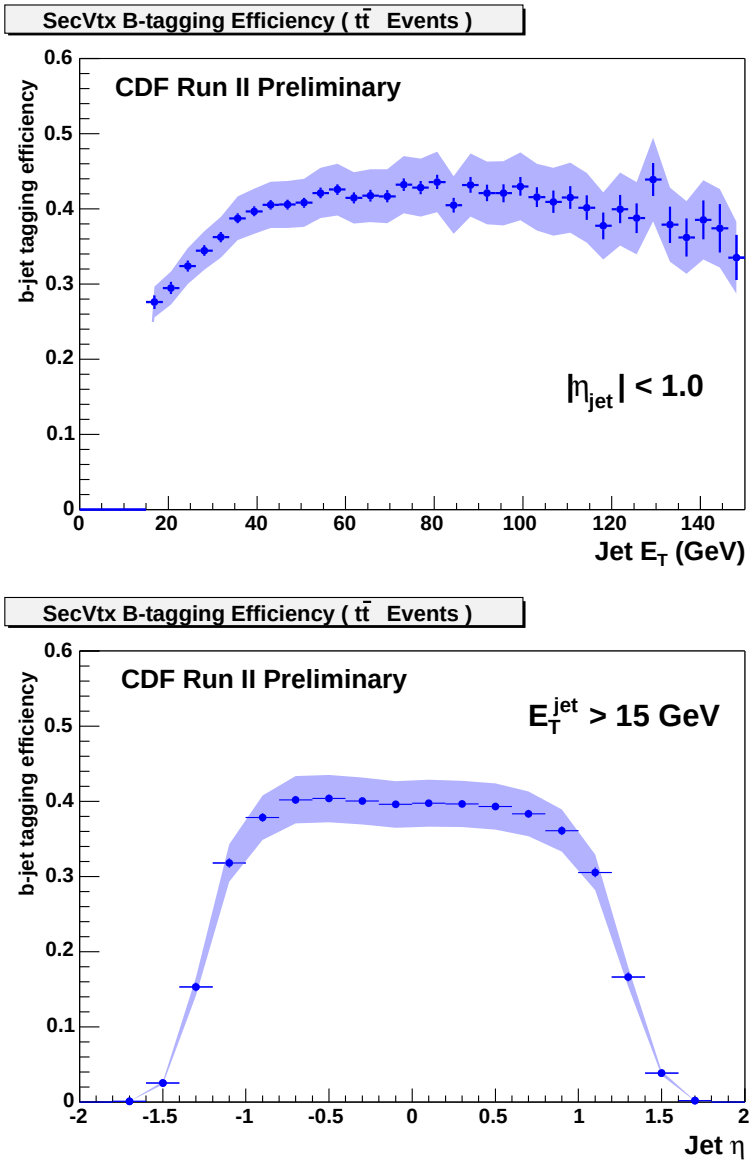

Figure 5.6: b tag efficency for p_T and η

b tagging is the mistag rate [54]. This gives the probability to tag a non b jet. The mistagged events are an important background for $t\bar{t}$ production because of the high cross section of QCD events. The mistag rate grows for jets between 15 GeV/c and 90 GeV/c nearly linearly from $\sim 0.1\%$ to $\sim 1\%$ and stays stable

at this level for p_T values greater than 90 GeV/c. Similar to the b tag efficiency, the mistag rate is correlated to the acceptance of the silicon detector. The mistag rate has the highest value at the border of the SVX around $|\eta| = 1$. The region is smeared out by the fluctuation of the primary vertex. The reason that the mistag rate is smaller in the central region is that the tracking efficiency is higher.

b jet probability

Jet Probability is an algorithm that is used to determine whether a jet is produced promptly at the primary interaction point or from the decay of a long-lived particle [55]. This algorithm makes use of the information of the tracks that are associated to a jet to determine the probability for this ensemble of tracks to be consistent with coming from the primary vertex. The probability distribution of a primary jet is by construction uniformly distributed between 0 and 1. For a long-lived jet the distribution peaks at 0, which means that the probability of such a jet to be primary is very small. Figure 5.7 illustrates the jet probability distributions JP from jets originating from light quark, charm, and bottom jets. This probability is based on the impact parameters and their uncertainties of the tracks in the jet.

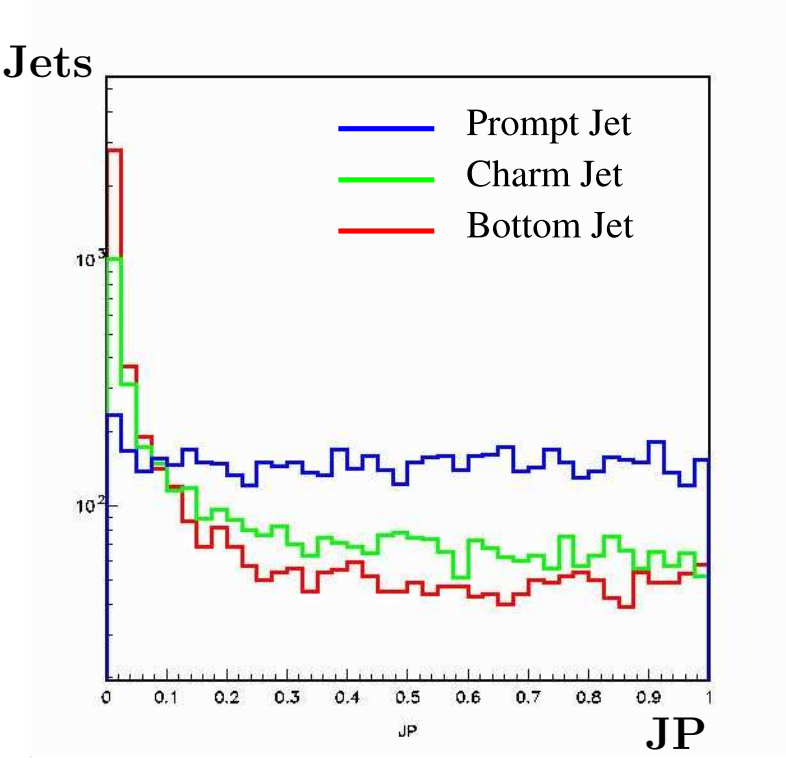

Figure 5.7: Jet probability distribution for prompt, charm and bottom jets

5.1.6 Summary

In table 5.4 we summarize the all cuts for the $t\bar{t}$ event selection and give the corresponding section, in which the cut has been introduced. Each event has to pass all selection cuts to be accepted in our further analysis. For the measurement of the helicity angle and the charge asymmetry a minimum of four tight jets is needed.

Cut	Comment / Ref.	
GoodRun	section 3.1	
Hight p_T lepton trigger	section 3.1	
Lepton ID cuts	section 5.1.1	
$\not\!\!E_T$	level 4 correction	> 20 GeV
di-lepton veto	section 5.1.4	
Z veto	section 5.1.4	
Conversion veto	section 5.1.4	
z vertex	section 5.1.4	$\lvert z_{vertex} - z_0^{lepton} \rvert < 5$ cm
SecVtx tag	section 5.1.5	> 0
tight jets	level 4 correction	$p_T > 15$ GeV/c and $\lvert\eta\rvert < 2.0$

Table 5.4: Summary of selection cuts.

5.2 Full reconstruction of $t\bar{t}$ events

In this section the reconstruction of the $t\bar{t}$ process will be developed and verified analyzing a PYTHIA sample. All events are simulated and reconstructed with the CDFSOFT version 5.3.3.

5.2.1 Complete Event Reconstruction with PAX

The feynman diagram in figure 5.8 shows the $t\bar{t}$ partonic process. In order to reconstruct the $t\bar{t}$ pairs different particles have to be reconstructed. Therefore we will describe step by step the procedure to get the complete partonic process.

The reconstruction starts after identifying jets, leptons and missing energy,

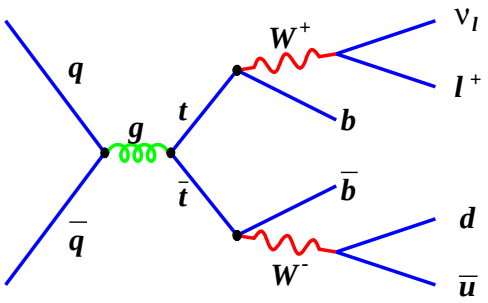

Figure 5.8: $t\bar{t}$ production feynman diagram for a semi-leptonic decay.

which is done by the `TopEventModule`. Combining all objects into one event interpretation, one can draw the different momentum vectors in a 3D-plot. This is shown in figure 5.9, where the lines represent the corresponding fourvectors. The length of the line corresponds to the absolute value of the momentum and the orientation to the direction of the three vector. During the evolution of the complete $t\bar{t}$ process all possible event interpretations are stored in their own `PaxEventInterpret`.

First step : $W \rightarrow \ell\nu$

The first step towards a complete reconstruction is reconstructing the leptonically decaying W boson. Therefore we need the fourvectors of the lepton and the neutrino. Only events which pass all selection cuts described in the last section are taken. Some kinematic distributions of the leptons can be seen in figure 5.10. As we require exactly one isolated high p_T lepton there are no ambiguities in the reconstruction. The p_T spectrum of the lepton shows a typical range of about 40 - 50 GeV/c. As we consider only central electrons and muons from the central muon systems, most of the measured $|\eta|$ values are smaller then one . The ϕ

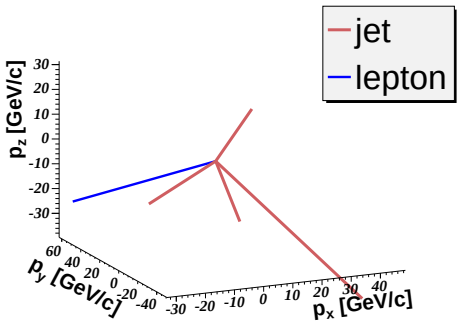

Figure 5.9: 3D view of a `PaxEventInterpret` with lepton (blue line) and jets (brown line). Each line represents the momentum three vector of the corresponding object.

distribution is uniform over the complete range. The difference between Monte Carlo true values and the measured values is shown in figure 5.11. As one can see the electron can be reconstructed almost perfectly. The resolution of the transverse momentum is determined by a double Gaussian fit to the difference between the Monte Carlo true value and the reconstructed one, see figure 5.11 a). We use a double Gaussian to account for tails. To understand the contribution of each single Gaussian we calculate the number of events within 2σ of the narrower peak f_{peak} and the quotient of both normalization constants f_{frac}. The resolution of p_T is about 1.3 GeV/c, taken from the narrower peak. About 82% of the events are within 2σ of the narrower peak. The resolution corresponds to the resolution of the calorimeter. The direction is also reconstructed very well. The difference in the $\eta - \phi$ - plane is always smaller than 0.02.

As the neutrino does not interact with the detector, only the missing transverse

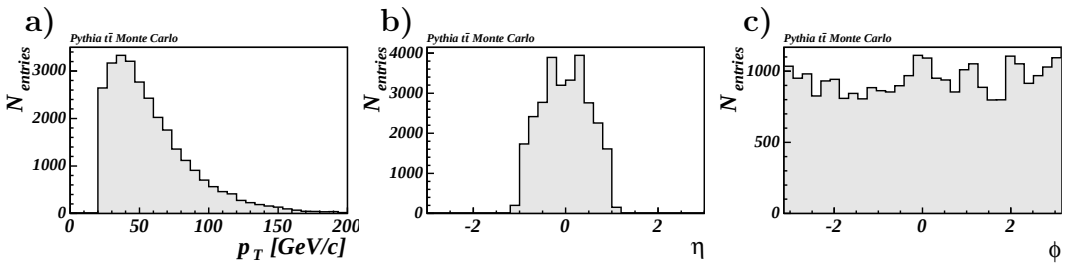

Figure 5.10: Measured p_T (a), η (b) and ϕ (c) values of the **isolated lepton** after simulation and reconstruction.

energy of the event and the ϕ-direction can be measured. To reconstruct the four-momentum of the neutrino we use the W boson mass constraint:

$$m_W = \sqrt{(p_\ell + p_\nu)^2} = 80.42\,\mathrm{GeV}/c^2$$

This leads to a quadratic equation with two solutions, for detailed calculation see Appendix B.1. If the solution is a complex number we take the real part,

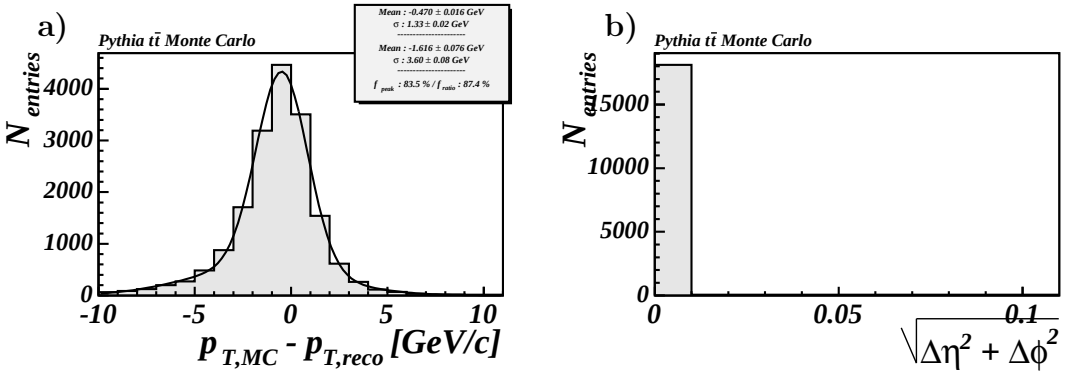

Figure 5.11: Difference between Monte Carlo true values and reconstructed values of the **isolated lepton**. a) p_T and b) distance in the $\eta - \phi$-plane. The p_T distribution is fitted with a double Gaussian. f_{peak} gives the fraction of events contained in the peak, meaning events within 2σ of the narrower Gaussian. In addition the fraction of the norming constants f_{ratio} of both Gaussians is stated.

otherwise we take the solution with the smaller value of $|p_z|$. The physical explanation for using the smaller value is that the decay products of a heavy particle, like the W boson, are produced dominantly with a large p_T. This means that they are produced centrally in the detector. In figure 5.12 an example of these two solutions with different reconstructed W bosons are shown. They are drawn as a 3D-view of both `PaxEventInterprets`.

As the W boson is also a decay product of a heavier particle, it is also produced

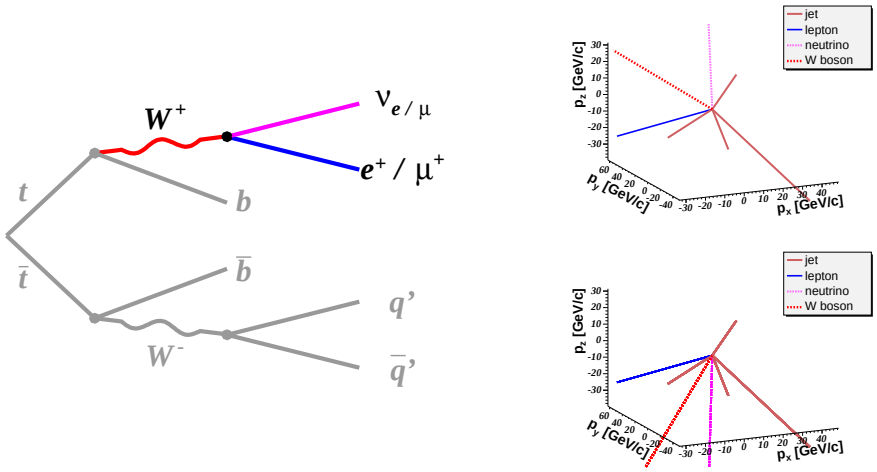

Figure 5.12: 3D view of the two different solutions of the reconstructed W boson (red dashed line) with the calculated ν fourvector (purple dotted line) for one representative event.

with high transverse momentum and small η values, see figure 5.13. The p_T spectrum has a mean value of 80 GeV/c and values up to 200 GeV/c.
Due to the imperfect measurement of the detected particle energies, the missing

energy and therefore also the transverse energy of the W is not perfect. The mismeasurement of the lepton can be neglected as shown before. To quantify the goodness of the reconstruction we first have to determine the correct event interpretation. The interpretation, for which the direction of the reconstructed fourvector points in the same direction as the fourvector of Monte Carlo true values, is defined as the correct one. Technically we calculate the distance $\Delta R = \sqrt{(\phi_{mc} - \phi_{reco})^2 + (\eta_{mc} - \eta_{reco})^2}$ in the $\eta - \phi$-plane between the reconstructed and the true values. We then define the interpretation with the smallest distance as the correct or best possible one. In figure 5.14 the differences between the Monte Carlo generated W boson and the best possible interpretation, is shown. The distance between the best possible reconstruction and the Monte Carlo true values is smaller than 0.5 in 82.7 % of all cases. The energy resolution is measured with a double Gaussian fit to the difference of the p_T distribution between the reconstructed and the Monte Carlo true values. We can reconstruct about 85.5% of the events with width of 12.2 GeV/c and with $\sim$ 4.3 GeV/c more transverse momentum then it was produced.

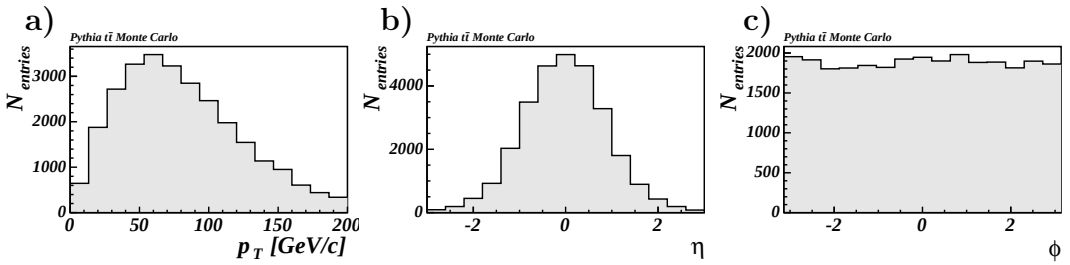

Figure 5.13: Measured p_T (a), η (b) and ϕ (c) values of the **leptonically decaying W boson** after simulation and reconstruction for the best possible interpretation.

Selecting the solution with the smaller value of $|p_z|$ is correct in $\sim$ 78% of the cases. To determine the quality of the selection of $|p_z|_{min}$ we show the η-distribution of the W boson and the cosine of the electron angle in the W boson rest frame meaning the angle between the electron in the W rest frame with respect to the W boost direction in figures 5.15. The solid black curve is defined as the best possible selection by the smallest $\Delta R = \sqrt{\Delta\eta^2 + \Delta\phi^2}$. The red crosses are the event interpretations with the smaller $|p_z|$ value for the two neutrino p_z solutions. The blue dashed histogram represents the other (wrong) event interpretations. As one can see the peak around $\eta = 0$ is slightly sharper than for the generated one. This is what we expect because we are always selecting this interpretation with the smaller value of $|\eta|$. An independent test of our selection is the electron angle in the W boson rest frame, which shows a good agreement with the Monte Carlo best possible reconstruction.

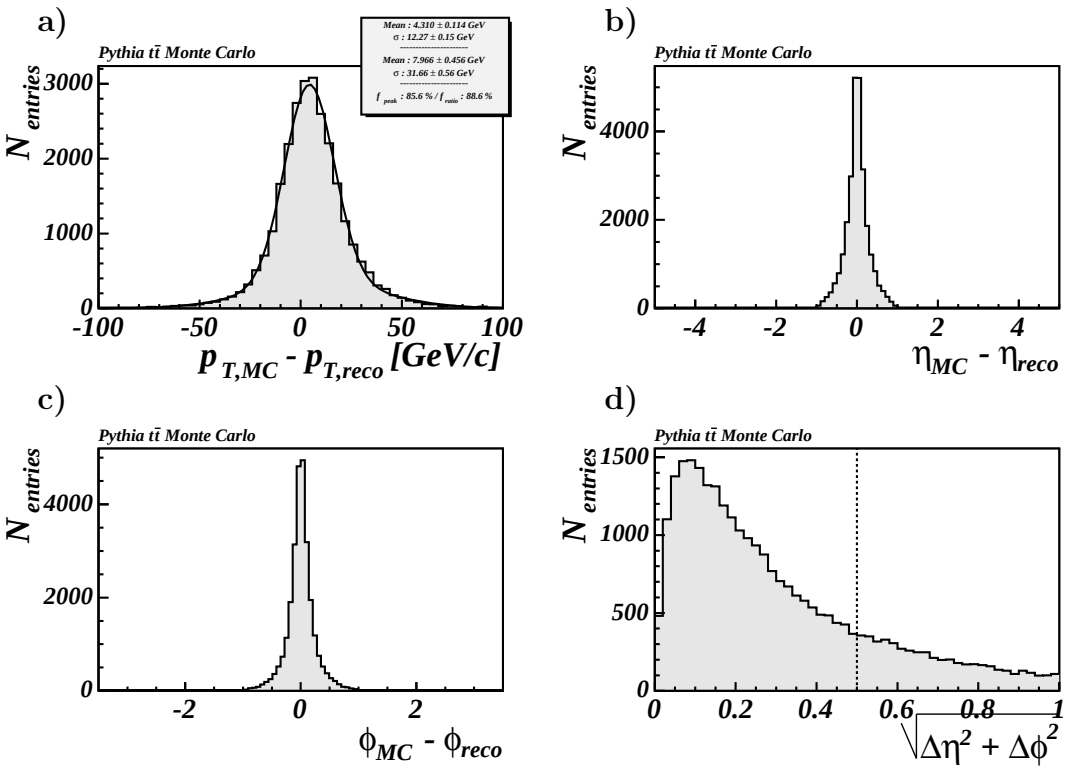

Figure 5.14: Difference between Monte Carlo true values and reconstructed transverse momentum (a) , η (b), ϕ (c) and the distance in the $\eta - \phi$ - plane (d) of the **leptonically decaying W boson** for the best possible event interpretation. The p_T distribution is fitted with a double Gaussian. f_{peak} denotes the fraction of events contained in the peak, meaning events within 2σ of the narrower Gaussian. In addition the fraction of the normalization constants f_{ratio} of both Gaussians is given.

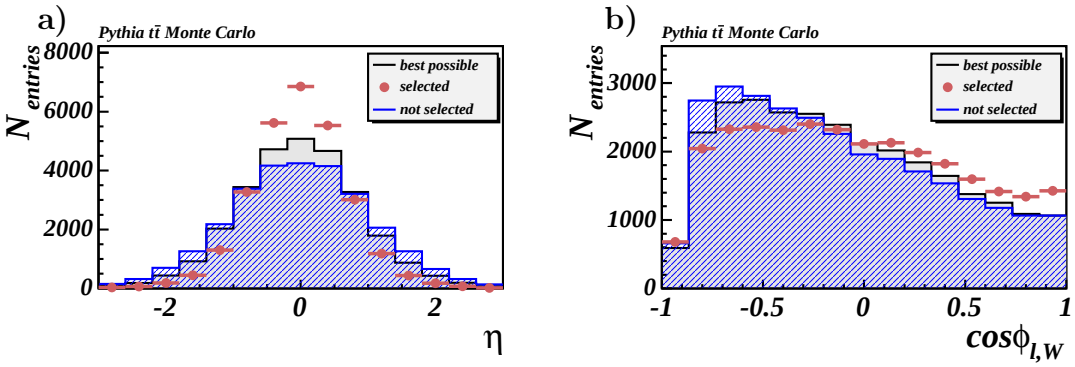

Figure 5.15: a) η of the W boson, b) cosine of electron angle in the W boson rest frame. The solid gray histogram represents the best possible event interpretation, the red crosses the interpretation with the smallest $|p_{z,\nu}|$ solution and the blue dashed histogram the other (wrong) solution.

$top \rightarrow bW \rightarrow \ell\nu$

The next step is the reconstruction of the leptonically decaying top quark. Therefore we combine each taggable jet with the W boson which decays into leptons and neutrinos. Taggable jets are jets which can potentially b tagged by the secondary vertex tagger. Therefore they have to fulfill some criteria. Taggable jets have to have more than 15 GeV/c transverse momentum, a minimum of two good tracks and have to be within the fiducial volume of the silicon vertex detector. As we need a minimum of four jets for the reconstruction of the complete $t\bar{t}$ process, we consider only events with four or more jets. Since we only need one jet for the leptonically decaying top quark, we can reconstruct four different event interpretations for a four jet event. In figure 5.16 these four different event interpretations are drawn in a 3-D view for one representive event.

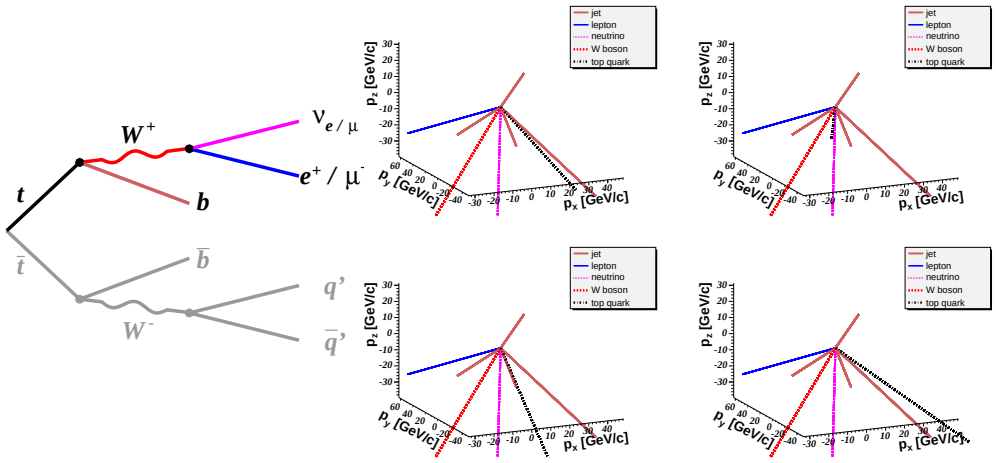

Figure 5.16: 3D view of the four different combinations of the reconstructed top quark (black dashed line).

The reconstructed top quarks are produced within a wide range of p_T with values from 50 GeV/c up to 200 GeV/c. The η range is between -2 and 2, see figure 5.17a),b). The top quark mass is obtained by a double Gaussian fit. About 50% of the events have a mean of $\sim$ 170.1 GeV/c^2 with a width of 13.7 GeV/c^2, see figure 5.17d). The difference of 8 GeV to the original produced mass of 178 GeV/c^2 is caused by the jet corrections which are general corrections for all types of jets. These corrections are in general too small for b quark jets because of the semi-leptonical decays of the B hadron, where additionally the energy of the neutrino is lost. The width of the reconstructed top quark mass is comparable to the energy resolution width of the transverse momentum, see figure 5.18. A double Gaussian fit gives a width of $\sim$ 11.5 GeV/c for about 78% of the events. The reason for that is not only the mismeasurement of the jet energy but also the definition of the "true" event interpretation. As the quarks interact via color strings with other colored particles it is possible that the jet direction does not point perfectly into the original b quark direction. Another

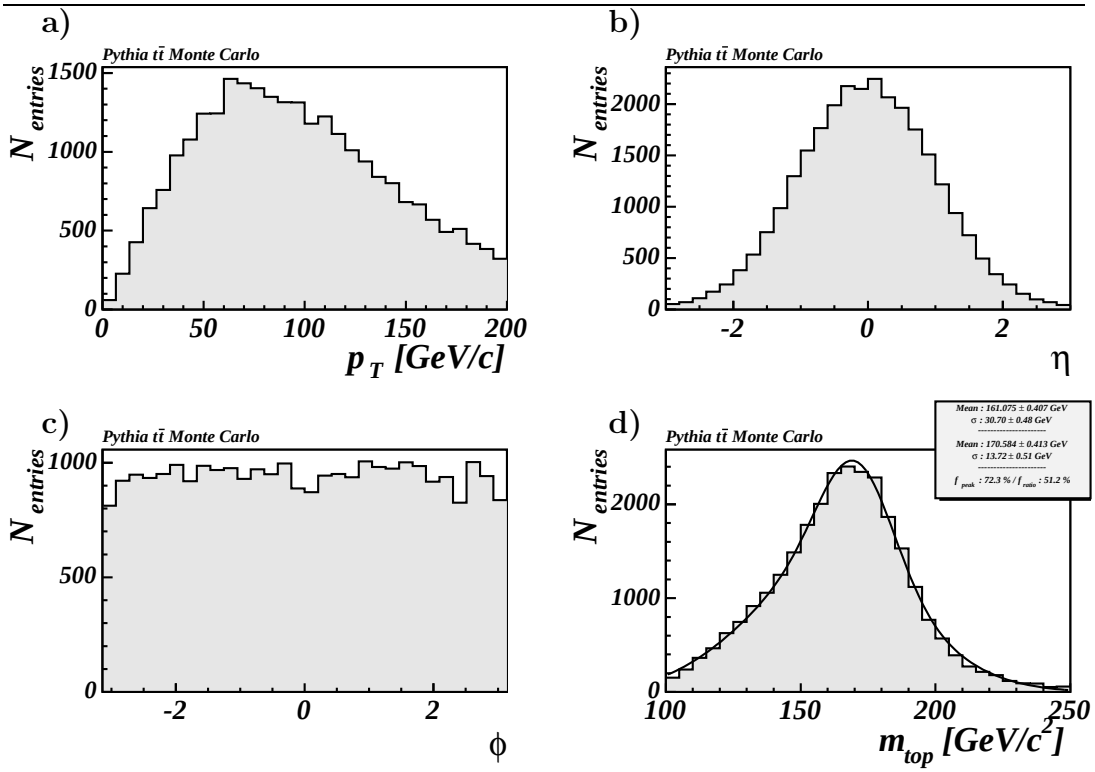

Figure 5.17: p_T (a), η (b), ϕ (c) and reconstructed mass (d) distribution of the **leptonically decaying top quark**. The mass distribution is fitted with a double Gaussian.

point is the jet algorithm itself, where the jet axis does not necessarily point into the direction of the originating quark but to the center of mass of the jet. This can be seen in the right plot of figure 5.18 where the difference in the $\eta - \phi$-plane between the best possible reconstructed event interpretation and the partonic top quark is shown. Nearly all events are within $\Delta R < 0.5$ (91.0 %).

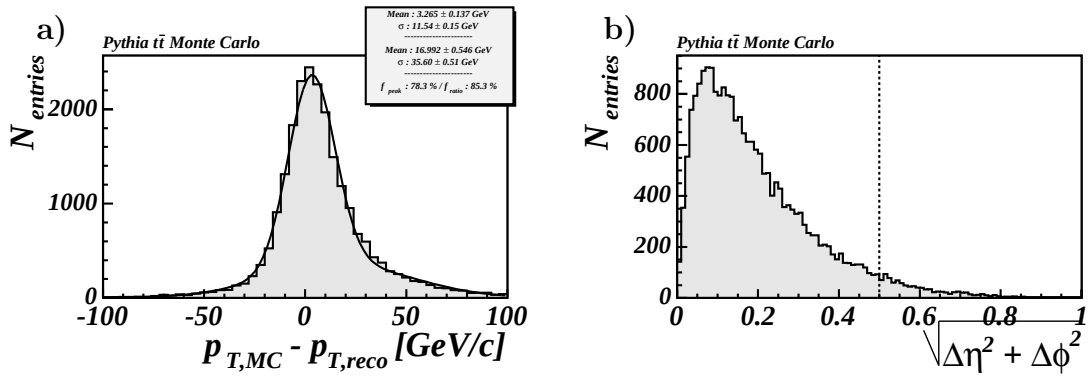

Figure 5.18: a) Difference in p_T and b) in the $\eta - \phi$-plane between partonic and best possible reconstructed **top quark**.

$W \rightarrow jj$

In the second "part" of the $t\bar{t}$ process we have to reconstruct the hadronically decaying W boson. Therefore we have to combine two jets not assigned to the leptonically decaying top quark. For a four jet event there are three remaining jets which can be combined to three different event interpretations for one chosen event interpretation for the already reconstructed top quark. In figure 5.19 one typical event interpretation is shown. The black line corresponds to the leptonically decaying top quark. The two red lines correspond to the two W bosons. Figure 5.20 shows the p_T and η distributions of the hadronically de-

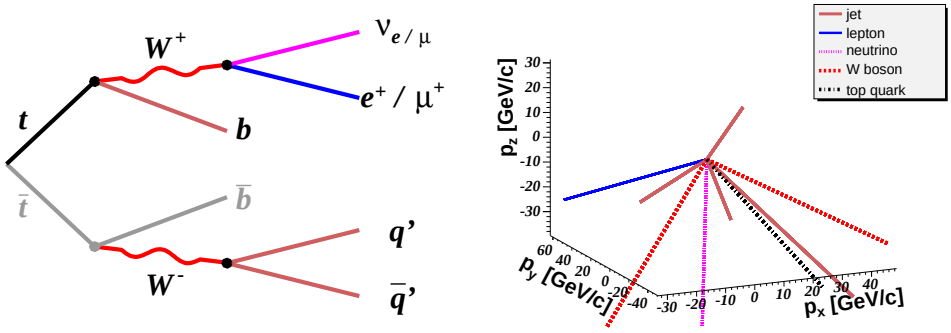

Figure 5.19: 3D view of one representative event interpretation with one reconstructed top quark(black dashed line) and two reconstructed W bosons (red dashed lines).

caying W boson.They are comparable to the leptonically decaying W boson as expected, because they are both decay products of a top quark. Since we do not have to constrain the mass of the W boson, we can measure it, see figure 5.20d). The result of a double Gaussian fit is a mean of $\sim$ 79.4 GeV/c^2 with a width of $\sim$ 10.8 GeV/c^2 for about 77% of the events. Since we have to combine only two jets the reconstruction of the energy and the direction is better than for the leptonically decaying top quark, see figure 5.21. The resolution of the transverse momentum is somewhat smaller compared to that of the leptonically decaying top quark with $\sim$ 13.7 GeV/c. The amount of events where the difference in the $\eta - \phi$-plane between reconstructed and true values is smaller than 0.5 (95.8%) is larger than for the leptonically decaying top quark.

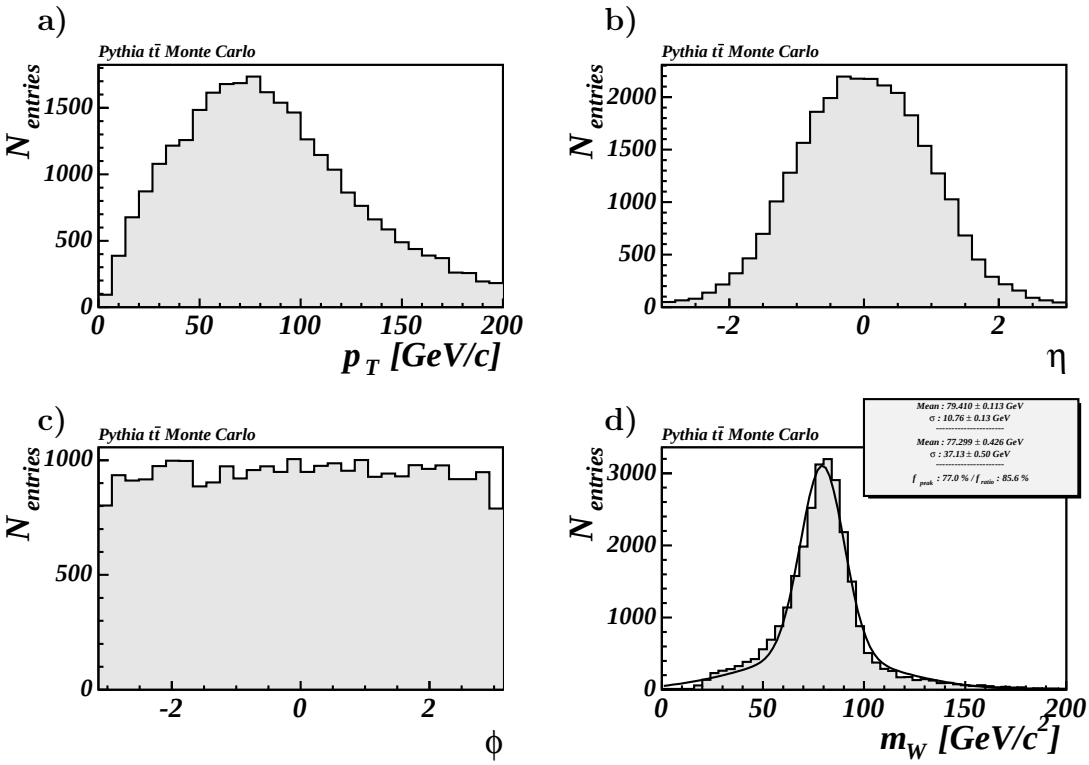

Figure 5.20: p_T (a), η (b), ϕ (c) and reconstructed mass (d) distribution of the **hadronically decaying** W **quark**. The mass distribution is fitted with a double Gaussian.

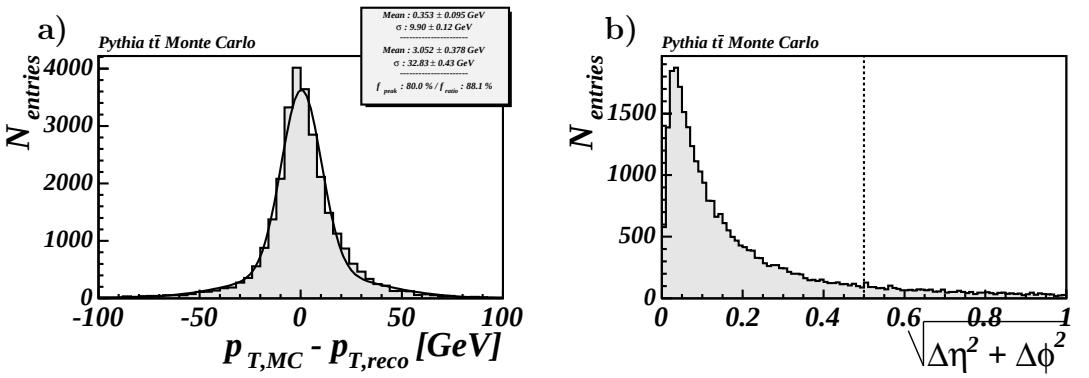

Figure 5.21: a) Difference in p_T and b) difference in the $\eta - \phi$-plane between partonic and best possible reconstructed **hadronically decaying W-boson**.

$top \rightarrow bW \rightarrow bjj$

The last stage is the reconstruction of the second top quark. Considering again four jet events we combine therefore the remaining jet with the hadronically decaying W boson. As for the steps before we show in figure 5.22 one representative event interpretation, now with both top quarks (black lines) and both W bosons.

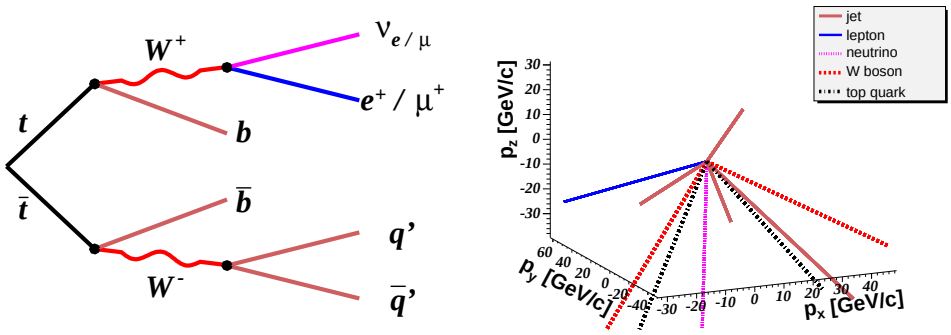

Figure 5.22: 3D view of one representative event interpretation (the same as in figure 5.19) with two reconstructed top quarks (black dashed lines) and two reconstructed W bosons (red dashed lines).

The p_T and η spectra of the hadronically decaying top quark are comparable to the leptonically decaying top quark with values about 100 GeV and an η-range between -2 and 2 see figure 5.23. For the top quark mass, determined with a double Gaussian fit, we get a mean value of ~ 173.1 GeV/c^2 and a width of ~ 11.6 GeV/c^2 for 71.8% of the events, see figure 5.23d). However there are large tails towards lower values. The resolution plots, shown in figure 5.24 are also comparable with the plots of the W boson. The width of smaller Gaussian of the double Gaussian fit is again ~ 12.4 GeV/c where we measure in average 0.8 GeV/c less transverse momentum and we have broad tails with values up to 100 GeV/c. The difference for the direction reconstruction is also of the same size as for the hadronically decaying W boson, we get $\sim 90.6\%$ events within $\Delta R < 0.5$. Summarizing the reconstruction of the different partons we can say that the energy resolution for all reconstructed partons, W bosons and top quarks, is comparable and of the order of 15 GeV. To check the quality of the parton reconstruction, we consider the difference ΔR in the $\eta - \phi$-plane between the partonic fourvector and the reconstructed fourvector. We see that most events (the worst value is $\sim 80\%$) are within a cone of 0.5 which corresponds to the cone radius of the used jet algorithm (0.4). So we can conclude that it is possible to reconstruct the complete partonic process with a energy resolution of about 15 GeV. However, there is also an amount of events ($\sim 20\%$) with a worse energy resolution of the order of 30 - 40 GeV. A second point is that the hadronically decaying top quark can be reconstructed better than the leptonically decaying one. A summary of the results is given in table 5.5.

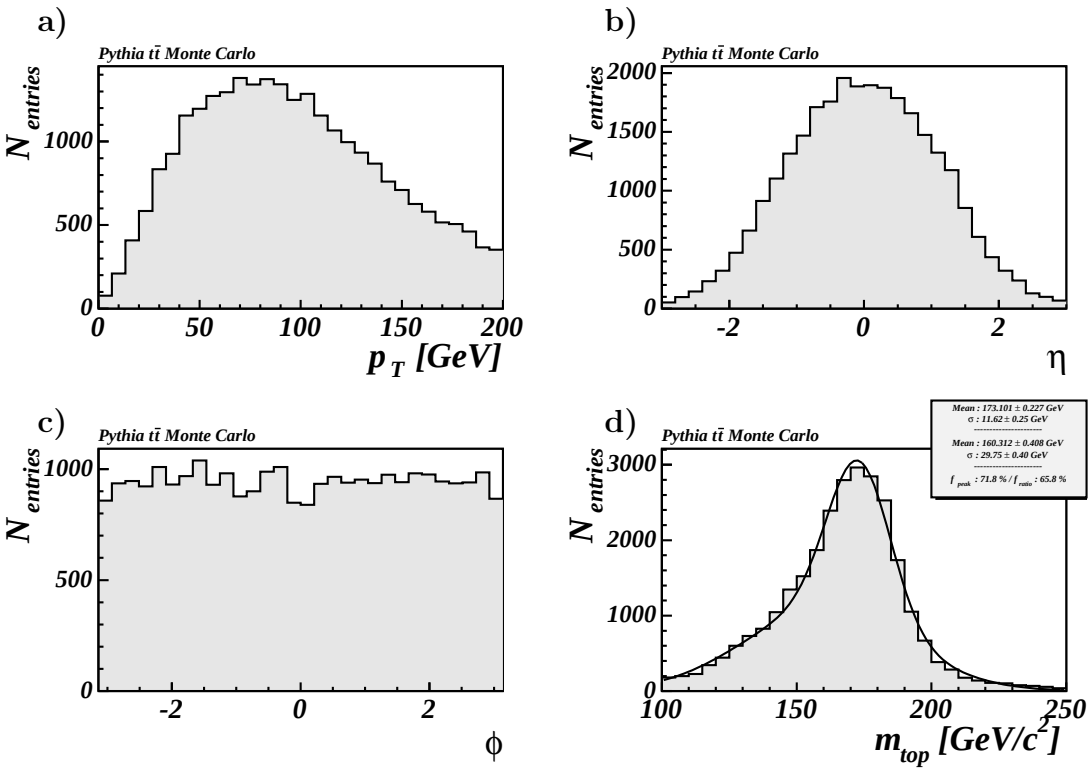

Figure 5.23: p_T (a), η (b), ϕ (c) and reconstructed mass (d) distribution of the **hadronically decaying top quark**. The mass distribution is fitted with a double Gaussian.

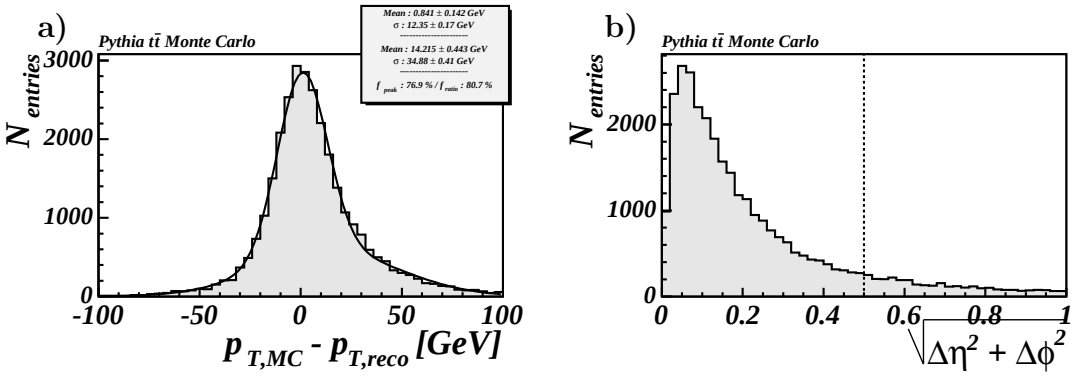

Figure 5.24: On the left plot the difference in p_T and on the right plot the difference in the $\eta - \phi$-plane between partonic and best possible reconstructed **top quark** is shown.

Parton	μ [GeV/c^2]	σ [GeV/c^2]	f_{peak}	$\Delta R < 0.5$
$W \to \ell\nu$				82.73 %
$W \to jj$	79.41	10.76	76.99 %	95.76 %
$top \to b\ell\nu$	161.08	30.70	72.28 %	91.04 %
$top \to bjj$	173.10	11.62	71.80 %	90.61 %

Table 5.5: Summary of mass reconstruction for the best possible event interpretation. We give the mean and the width of the double Gaussian fit for the Gaussian with the narrower width. Also the amount of events within 2σ of this Gaussian is given. The last colum gives the amount of events with a distance in the $\eta - \phi$-plane between reconstructed and generated parton smaller than 0.5.

5.2.2 Selection of the Correct Event Interpretation

In data, we have no direct information about the initial top quarks. In order to choose the best event interpretation here, we determine for each interpretation a quantity Ψ, which gives a quantitative estimate how well the hypothesis matches the $t\bar{t}$ pair assumption. Several quantities enter the computation of Ψ:

1. Constraints on the mass of the hadronically decaying W boson.
2. The difference between both reconstructed top masses (two particles with the same mass).
3. The b likeness of the jets chosen to be the b jets from the top pair (P_{b-prob}).
4. A constraint on the sum of the reconstructed transverse energy. of the two top quarks, which should in leading order calculation be equal to the transverse energy of the event

We define Ψ as:

$$\Psi = \frac{P_\nu}{|\alpha - P_{energy}| \cdot \chi^2} \cdot P_{b-prob} \tag{5.2}$$

The five constituents are defined as follows :

1. **$\mathbf{p_z}$ of the neutrino**
   As described in section 5.2.1 we take always the solution with the smaller value of $|p_z|$. In equation 5.2 we set $P_\nu = 1$ for the smaller and equal to 0 for the larger solution.
2. **χ^2 for masses**
   We calculate a χ^2 including the reconstructed W mass of the hadronically decaying W boson and the difference between both reconstructed top quark masses. Since we want to have the top quark mass as a control variable, we do not constrain the mass, but the difference between both masses. The expected W mass $m_{W\to jj,exp}$ and the width $\sigma_{m_{W\to jj}}$ is obtained from a double Gaussian fit to the mass distribution of the best possible event interpretation. We use the width and the mean from the Gaussian with the smaller width, see 5.5. The uncertainty of the top quark mass difference is obtained in the same way, see figure 5.25a). The width $\sigma_{\Delta m_{top}}$ is the weighted average of the two widths obtained from the double Gaussian fit on the Δm_{top} distribution.

   Then the χ^2 is given by :

$$\chi^2 = \frac{(m_{W\to jj,reco} - m_{W\to jj,exp})^2}{\sigma^2_{m_{W\to jj}}} + \frac{(m_{top\to b\ell\nu,reco} - m_{top\to bjj,reco})^2}{\sigma^2_{\Delta m_{top}}} \tag{5.3}$$

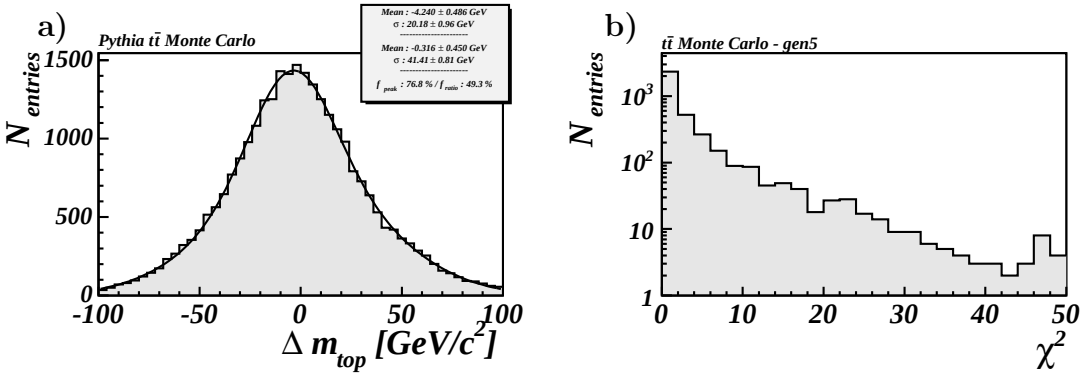

Figure 5.25: a) Difference between both reconstructed top quark masses using the best possible event interpretation. The distribution is fitted with a double Gaussian. The width $\sigma_{\Delta m_{top}}$ is the weighted average of the two widths. b) χ^2 distribution for the best possible $t\bar{t}$ event interpretation, plotted on a logarithmic scale.

with

$$\begin{aligned} m_{W\to jj,exp} &= 79.4\,\mathrm{GeV}/c^2 \\ \sigma_{m_{W\to jj}} &= 10.8\,\mathrm{GeV}/c^2 \\ \sigma_{\Delta m_{top}} &= 30.9\,\mathrm{GeV}/c^2 \end{aligned}$$

The χ^2 values for the best possible $t\bar{t}$ event interpretations are given in figure 5.25b).

3. **b probability**
   To take the b likeness of the jets assigned as b jets into account we consider the so called b probability calculated by the `JetProb` package. This algorithm calculates the probability of the jet belonging to the primary vertex. We are using the values which are calculated considering positive impact parameters in the $r-\phi$-plane JP. In figure 5.26 the logarithm of this variable is shown. Jets originating from b quarks, defined as jets from the top quark decay, are plotted in the black solid histogram, and jets originating from light quark jets are plotted in the blue dashed histogram. The light quark jets have a typical value around 0, as expected, where jets containing B Hadrons are distributed over the complete range. To exploit the purity of the secondary vertex tag (tag), we multiply the jet probability value with 10 for each tagged jet assigned to the top quarks.

$$P_{b-prob} = (-log(JP_{top\to bl\nu})) \cdot (-log(JP_{top\to bjj})) \cdot 10^{\Sigma tag} \qquad (5.4)$$

4. **energy criteria**
   The last contribution to our selection variable is a consideration of pro-

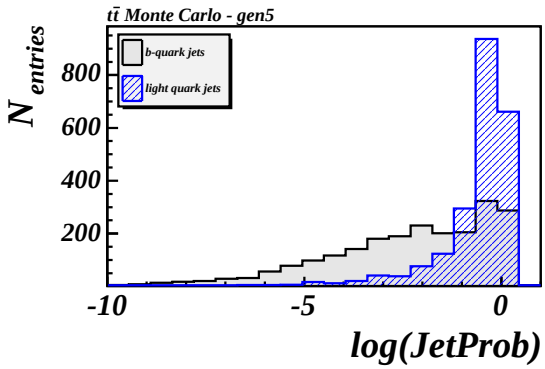

Figure 5.26: Jet probability (`jpbRPpos`) for b quark jets (black line) and light quark jets (blue dashed histogram)

duced and reconstructed energy in the event. For a $2 \rightarrow 2$ process the following equation holds for each particle i:

$$E_i = m_{T,i} \cdot \cosh y_i \tag{5.5}$$

where m_T is the transverse mass

$$m_{T,i}^2 = m_i^2 + p_T^2 \tag{5.6}$$

Since we have an ambiguity in the longitudinal momentum of the neutrino we are only able to reconstruct the transverse momentum completely. Therefore we consider only the transverse part of equation 5.5. The sum of the transverse energy $H_T = E_{T,top\rightarrow b\ell\nu} + E_{T,top\rightarrow bjj}$ is then given by:

$$H_T = \sqrt{\sum p_{T,top}^2 + \sum m_{reco,top}^2} \tag{5.7}$$

This equation can now be used as a variable by dividing the reconstructed top quantities by the measured total transverse energy :

$$P_{energy} = \frac{\sqrt{p_{T,top\rightarrow b\ell\nu}^2 + m_{top\rightarrow b\ell\nu}^2} + \sqrt{p_{T,top\rightarrow bjj}^2 + m_{top\rightarrow bjj}^2}}{\sum\limits_{t\bar{t}\,\text{jets}} p_{T,jet} + E_{T,miss} + E_{T,\ell}}$$

In figure 5.27 this ratio is shown for the best possible event interpretation. We fit this distribution with a double Gaussian to get the average ratio. We obtain a mean of 1.014 and a width of 0.09 from the Gaussian with the smaller width. The mean of P_{energy} distribution is indicated in equation 5.2 with α.

To show the different values for the different event interpretations of our selection variable Ψ (eq. 5.2), we plot for one representative event the value of Ψ for each interpretation. This can be seen in figure 5.28. The red cross marks the best possible interpretation, which has also the highest value of Ψ.

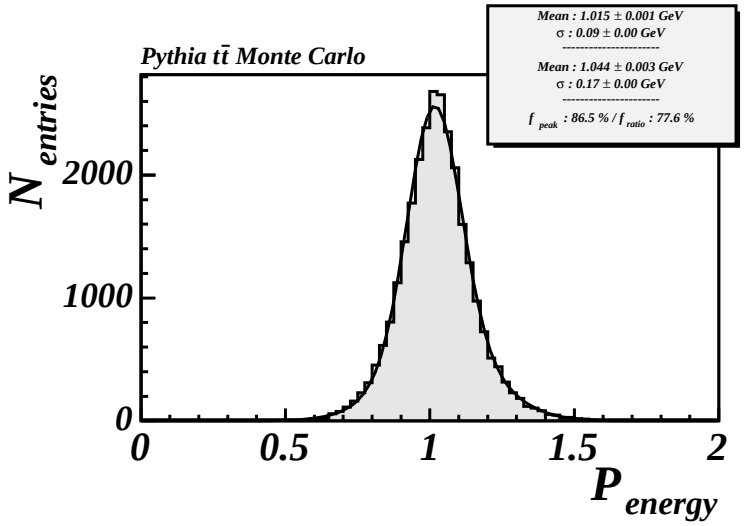

Figure 5.27: Ratio of reconstructed over measured transverse energy P_{energy} for the best possible event interpretation.

5.2.3 Quality of the selection

Choosing the event interpretation with the highest Ψ as the best one, we have to check the goodness of our selection procedure. Therefore we compare our selection with the best possible one and all others. The best possible one is defined in the same way as mentioned before. For all histograms the black solid histogram represents the distribution of the correct (best possible) event interpretation, the red crosses this interpretation with the highest Ψ value and the blue dashed all others. Since we are interested in the difference of the shapes the wrong interpretations are weighted with the number of event interpretations per event. First we check the reconstructed masses of the top quarks and the hadronically decaying W boson, see figures 5.29 a - c. We fit all three distributions with a double Gaussian and state the results in table 5.6. The values are the fit results of the narrower Gaussian, additionally we give the fraction of events f_{peak}, which are within 2σ of the narrower Gaussian. Compared to table 5.5 the results of the W boson is comparable to the values of the best possible interpretations, which is not surprising, since we use these values in the χ^2. Our selection tends to choose in some cases interpretations with smaller top quark masses as the best possible one.

Not only the mass distributions are interesting and useful to check the goodness of our selection, but also kinematic variables such as the transverse momenta, η or decay angles for the top quarks and their decay products. The p_T distributions of both top quarks are shown in figure 5.29 d,e. The selected interpretation approximates the shape of the best possible event interpretation

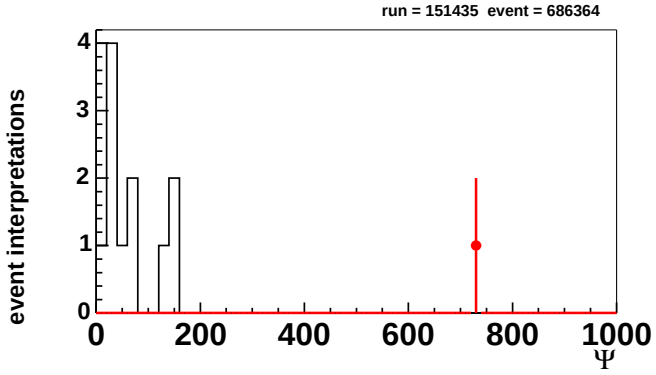

Figure 5.28: Ψ for one representative event. The cross indicates the event interpretation with the highest value, the solid black histogram are all other interpretations.

	μ	σ	f_{peak}
$m_{W\to jj}$	80.8 GeV/c^2	9.0 GeV/c^2	80.8 %
$m_{topW\to \ell\nu}$	160.1 GeV/c^2	24.8 GeV/c^2	92.4 %
$m_{topW\to jj}$	172.5 GeV/c^2	10.5 GeV/c^2	55.4 %

Table 5.6: Summary for fit results of mass reconstructions.

very well. The wrong combinations tend to have smaller values. The η distributions of the top quarks, figure 5.30 a,b, are very similar for the selected one, the best possible one as well as for the discarded interpretations. Only the selected interpretation of the leptonically decaying top quark has a somewhat narrower shape. That is due to the selection of the smaller $|p_z|$ solution for the neutrino. Figure 5.30 c,d shows the decay angles of the W bosons, meaning the angle between the W boson in the top quark rest frame with respect to the boost direction of the top quark. There are only differences between the best possible and the wrong event interpretations for the leptonically decaying top quark. Our selected interpretations describe the shape of the best possible very well. In the case of a hadronically decaying top quark the differences vanish. As a last check we consider the further decay of the W bosons. In figure 5.30 e,f the right plot shows the decay angle of the jet, meaning the angle between the first jet in the W rest frame with respect to the W boson boost direction. Our selected combination is in very good agreement with the best possible selection where the wrong combinations show a big difference for values around 1. The distribution of the electron decay angle is shown in the left plot. This distribution does not differ very strongly between the selected, the best possible and the other event interpretations.

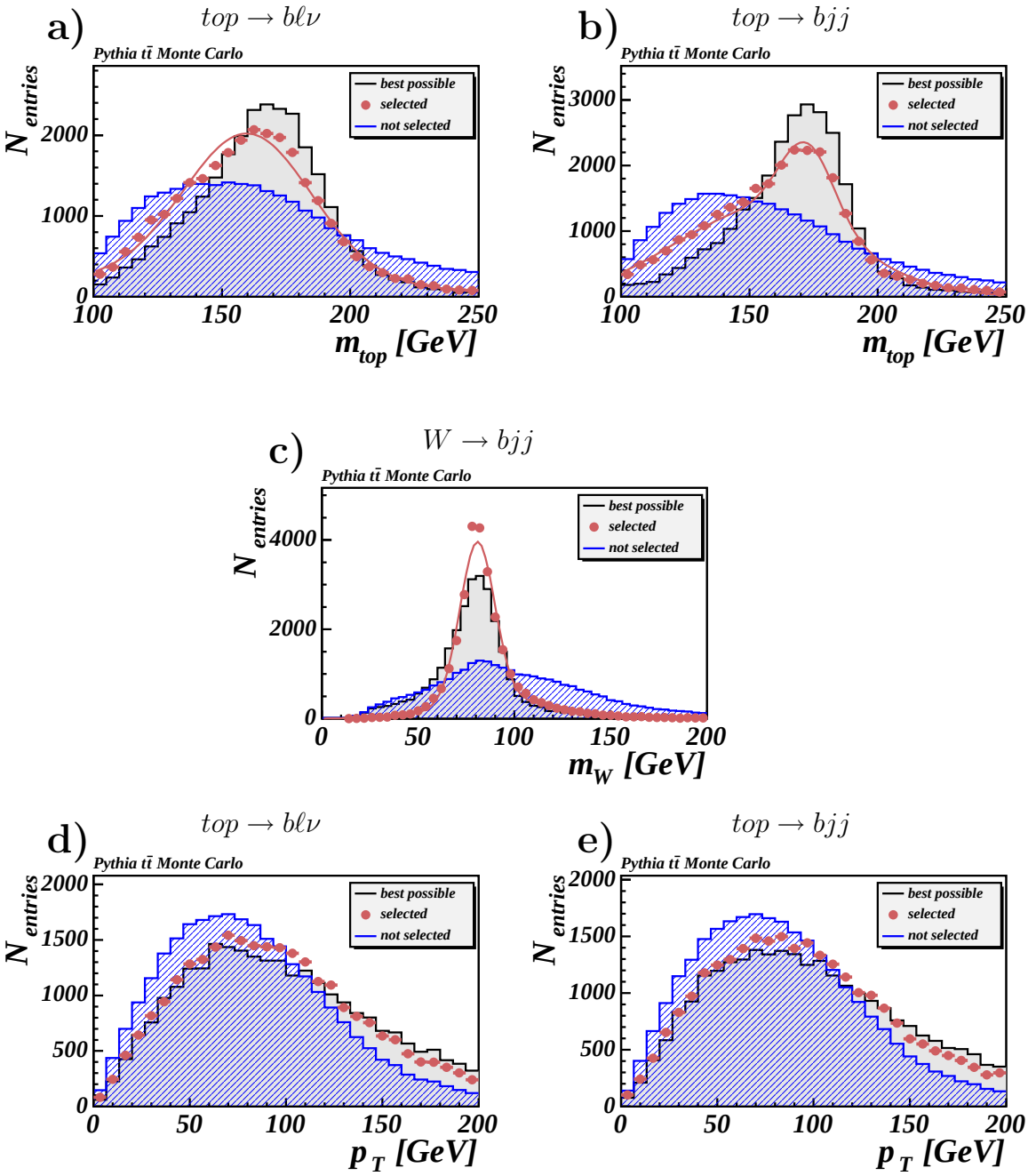

Figure 5.29: The solid black histograms represent the best possible event interpretation, the red crosses represents the selection with our procedure and the blue dashed represents the remaining interpretations weighted with the number of interpretations in the event. (a) Reconstructed mass of the leptonically decaying top quark. (b) Reconstructed mass of the hadronically decaying top quark. (c) Reconstructed W boson mass. The fits are applied to the histogram selected by our procedure. (d) p_T distribution of the leptonically decaying top quark. (e) p_T distribution of the hadronically decaying top quark.

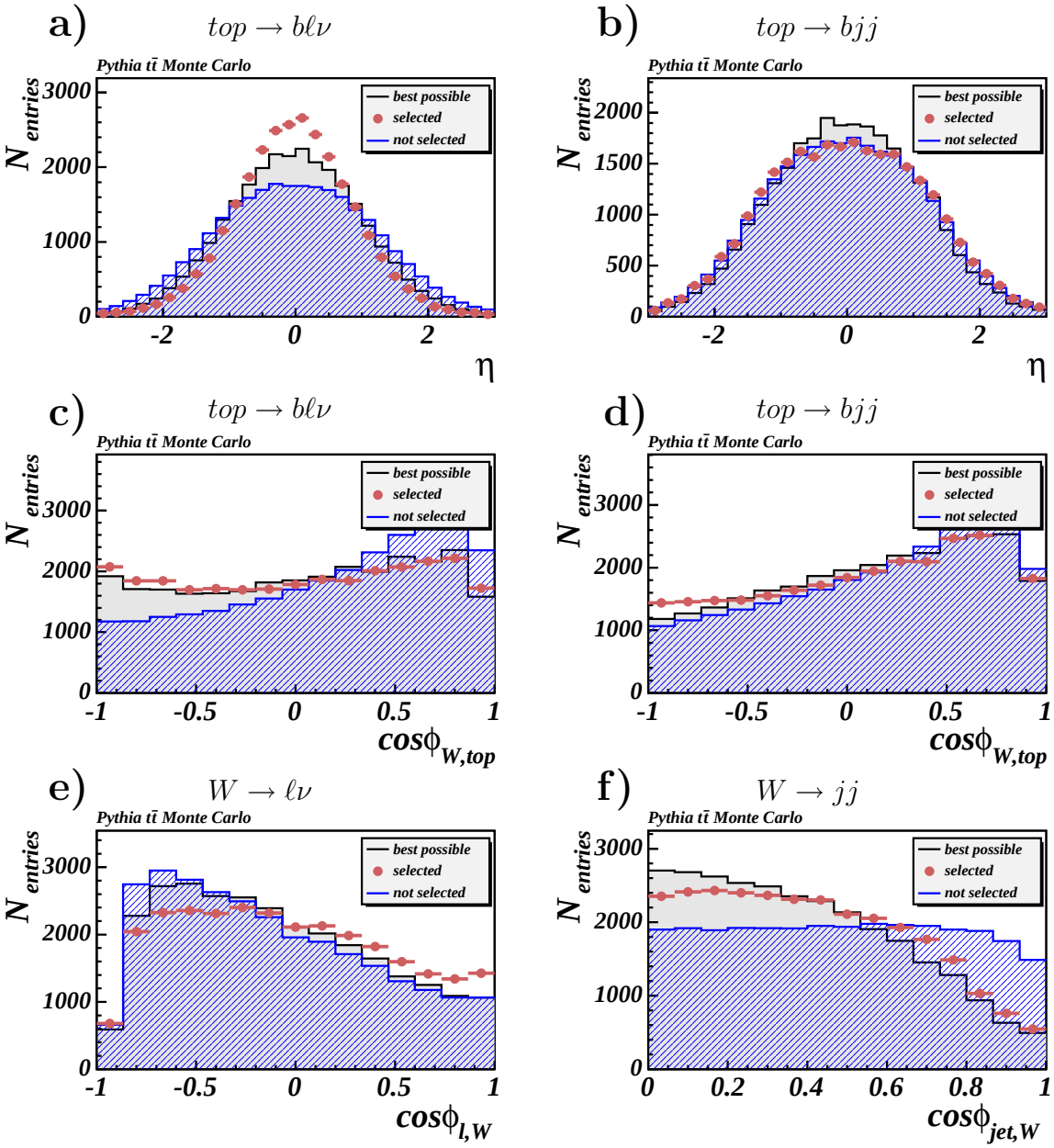

Figure 5.30: The solid black histograms represent the best possible event interpretation, the red crosses represents the selection with our procedure and the blue dashed represents the remaining interpretations weighted with the number of interpretations in the event. Shown are : (a) Pseudorapidity of the leptonically decaying top quark. (b) Pseudorapidity of the hadronically decaying top quark. (c) Cosine of the W boson in top quark rest frame for the leptonically decaying top quark. (d) Cosine of the W boson in top quark rest frame for the hadronically decaying top quark. (e) Cosine of the electron in W rest frame of the leptonically decaying W boson. (f) Absolute value of the cosine of jet angle in W rest frame of the hadronically decaying W boson.

5.3 Comparison with the Kinematic Fitter

In the previous section we presented our procedure to fully reconstruct $t\bar{t}$ event candidates. In this section we compare our method with the kinematic fitter. The kinematic fitter is described in detail in ref. [56].

The basic idea of the kinematic fitter is to incorporate the known systematic detector effects into the computation of the invariant mass of the top quark and the reconstruction of the top pair. For each hypothesis of a selected $t\bar{t}$-candidate a χ^2 function, consisting of physics constraints and detector systematics, is minimized. In contrast to our procedure the hypotheses are build up only from the four highest energetic jets, leading to 24 hypotheses, corresponding to 12 ways to assign the four leading jets to the four partons in the $t\bar{t}$ decay, times the 2 solutions from the z-component of the momentum of the neutrino. b tagging information is taken into account by ignoring those combinations, where a b tagged jet is assigned to a light quark at parton level. A further difference to our method is that the kinematic fitter uses the jet four-vectors corrected to the partons from the top pair. For this correction the so called top specific corrections [57] are applied in addition to the level 5 jet energy corrections, while we apply the level 7 jet energy corrections in our procedure. In the χ^2 function the transverse momenta of the leptons and the four jets and the x and y components of the unclustered energies are permitted to vary in the fit according to their resolutions. Here unclustered energies means any energy seen in the calorimeter, which is not associated with the charged lepton or a jet. Furthermore, mass constraints on the masses of the leptonically and hadronically decaying W boson, are applied using a width of 2.12 GeV/c^2. The top mass M_t^{fit} is a free parameter in the fit, which enters in the terms $(m_{bjj} - M_t^{fit})^2/\Gamma_t^2$ and $(m_{b\ell\nu} - M_t^{fit})^2/\Gamma_t^2$. Here, m_{bjj} and $m_{b\ell\nu}$ refer to the invariant mass of the sum of the four-vectors denoted in the subscript. Γ_t is the total width of the top quark and is chosen to be 1.5 GeV/c^2. The fit routine returns the four-vectors of the lepton, of the neutrino and of the four jets (partons) for each combination. The hypothesis with the smallest χ^2 value is selected. The four-vectors of the W^+, W^-, top and anti-top quark are then obtained by adding the four-momenta of their decay particles.

In figures 5.31 the kinematic fitter and our method are compared for kinematic quantities of the hadronically decaying W boson respectively. The selected event interpretation of our method (red points) is compared with the selected hypothesis of the kinematic fitter (blue triangles). In addition the best possible event interpretation is drawn in the figures (solid black line). A similar comparison for the kinematic quantities of the leptonically decaying and hadronically decaying top quark is performed in figures 5.32 and 5.33, respectively. Except for the reconstructed mass of the hadronically decaying W boson and top quark the kinematic fitter and our method lead to almost equivalent results. Since the mass of the hadronically decaying W boson is constrained very tightly in case

of the kinematic fitter, the resolution of these quantities is better than for our method, especially for the reconstructed mass of the hadronically decaying W boson.

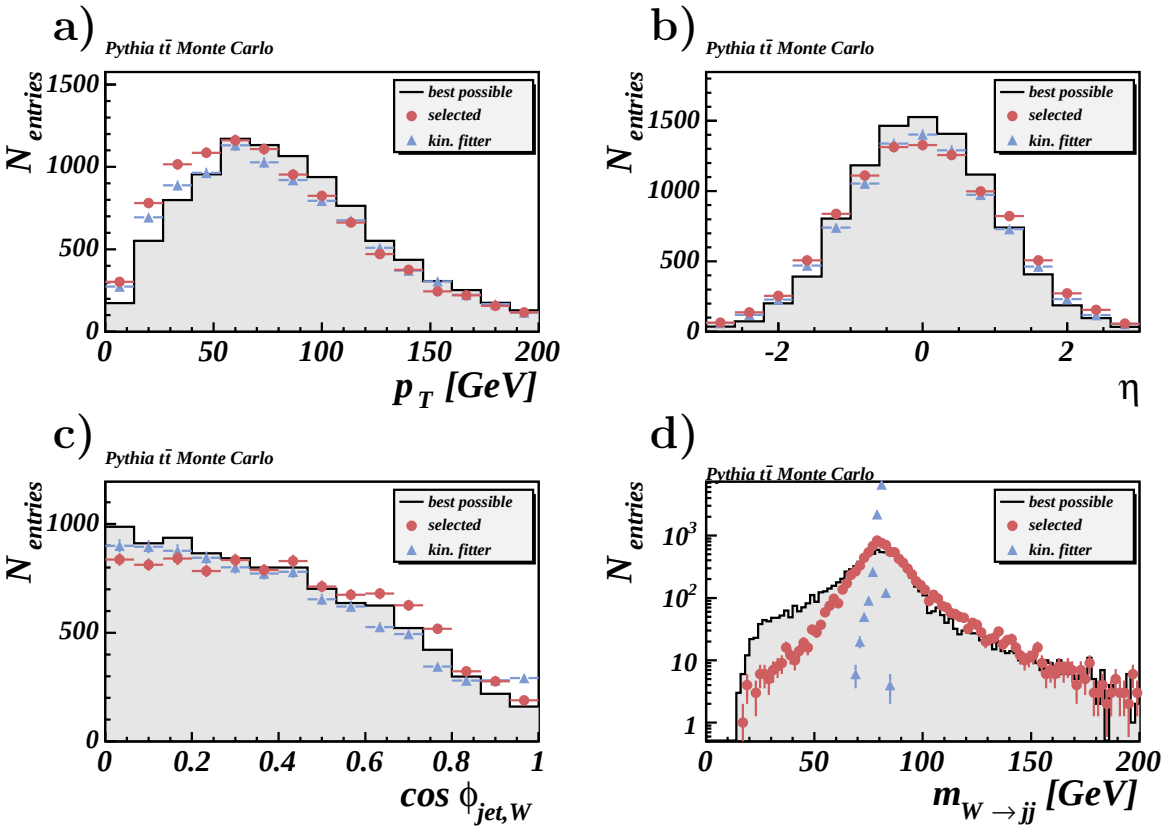

Figure 5.31: Comparison of the kinematic fitter with our method for quantities of the **hadronically decaying W-boson**. Shown are the transverse momentum (a), the pseudorapidity (b) of the W boson, the cosine of the angle of the first light quark jet $\cos\phi_{jet,W}$ (c) in the rest frame of the W boson with respect to the boost direction of the W boson and the reconstructed mass of the W boson (d) obtained by the Monte Carlo generator Pythia. The selected event interpretation of our method (red points) is compared with the selected interpretation of the kinematic fitter (blue triangles) as well as with the best possible one (solid black line).

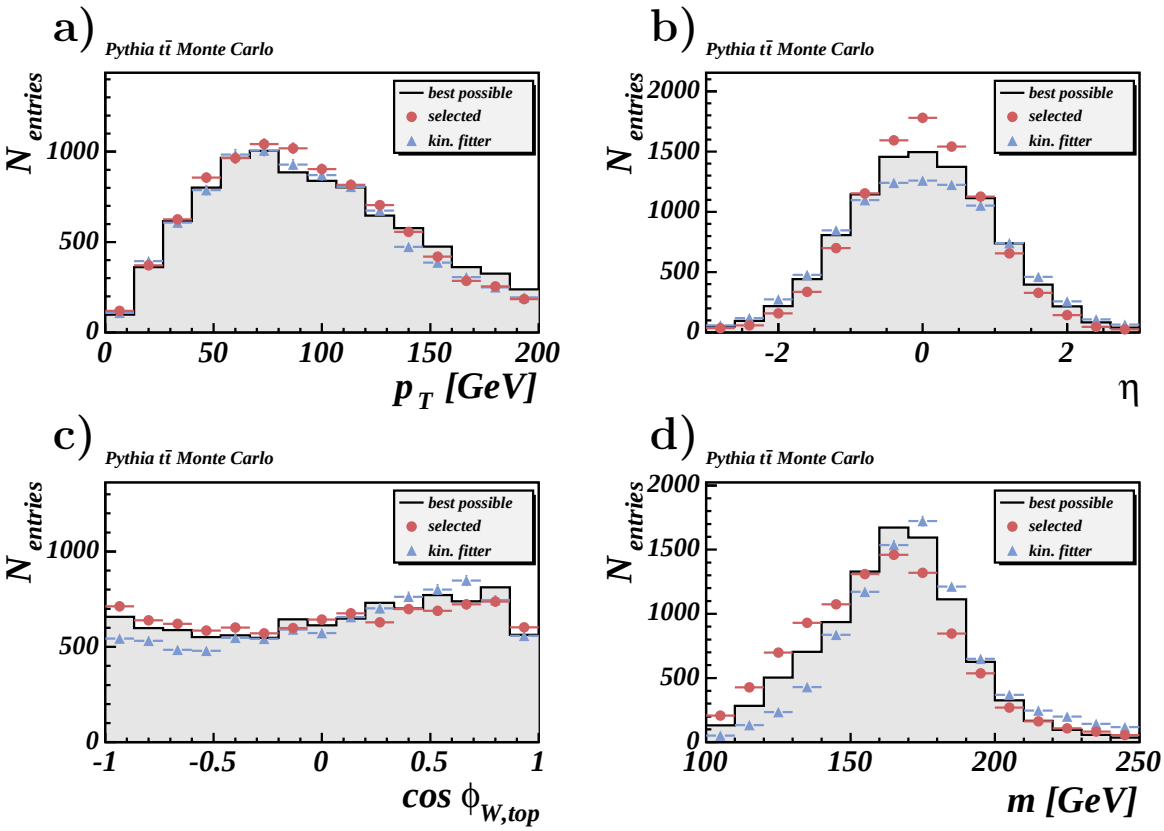

Figure 5.32: Comparison of the kinematic fitter with our method for interesting quantities of the **leptonically decaying top quark**. Shown are the transverse momentum (a), the pseudorapidity (b) of the top quark, the cosine of the angle of the W boson $\cos\phi_{\ell W}$ (c) in the rest frame of the W boson with respect to the boost direction of the top quark and the reconstructed mass of the top quark (d). The selected event interpretation of our method (red points) is compared with the selected interpretation of the kinematic fitter (blue triangles) as well as with the best possible one (solid black line).

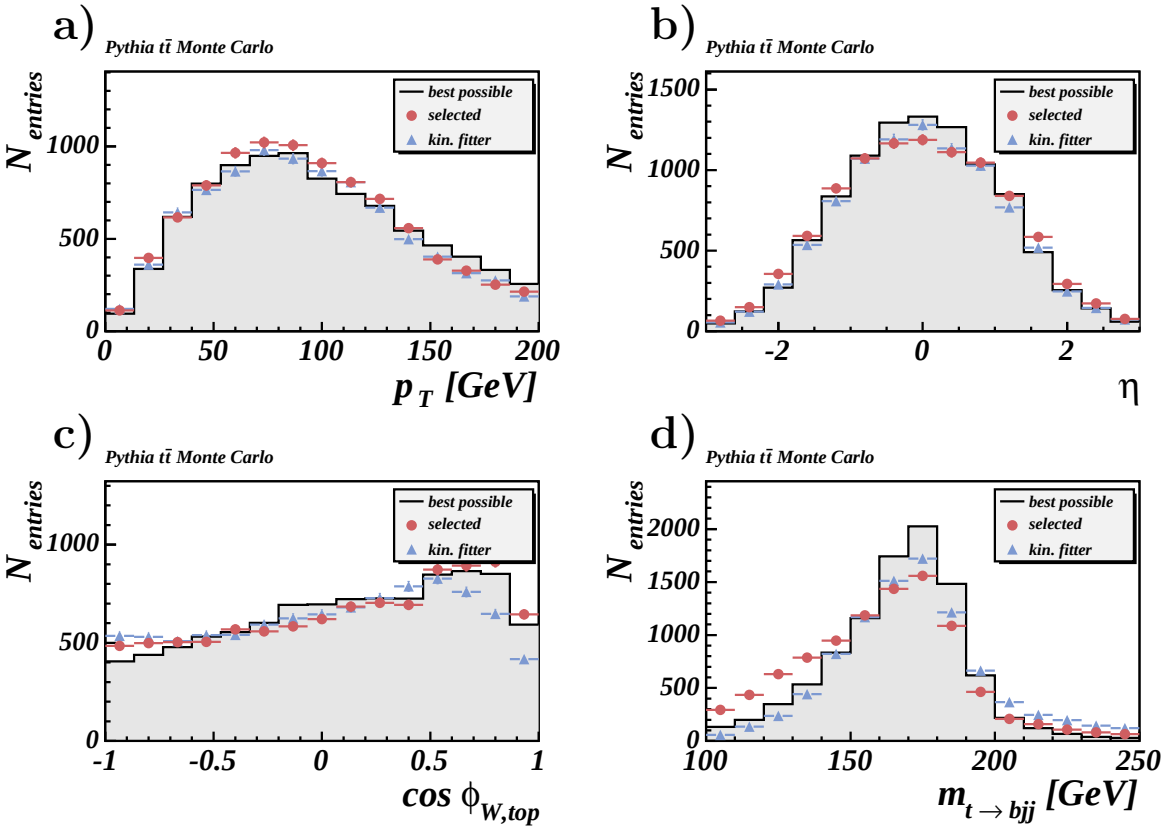

Figure 5.33: Comparison of the kinematic fitter with our method for quantities of the **hadronically decaying top quark:** $t \to b\,j\,j$. Shown are the transverse momentum (a), the pseudorapidity (b) of the top quark, the cosine of the angle of the W boson $\cos(\Phi_{W\to jj})$ (c) in the rest frame of the W boson with respect to the original flight direction of the top quark and the reconstructed mass of the top quark (d) obtained by the Monte Carlo generator Pythia. The selected event interpretation of our method (red points) is compared with the selected interpretation of the kinematic fitter (blue triangles) as well as with the best possible one (solid black line).

The fractions how often the selected event interpretation of the kinematic fitter as well as the selected interpretation of our method corresponds to the best possible one, are given in table 5.7. Additionally the fraction of events for both methods which lies within a certain distance $\sum \Delta R$ with respect to the Monte Carlo true value are given. The $\sum \Delta R$ is defined as :

$$\sum \Delta R \;=\; \Delta R_{t\to b\ell\nu} + \Delta R_{t\to bjj} + \Delta R_{W\to jj} \tag{5.8}$$

Both methods lead to almost the same fractions in all four categories, whereas our method yields slightly better results. Thus, the two methods are comparable in finding the best event interpretation. Another very important criterium to

	Selected $t\bar{t}$ event interpretation [%]	
	our method	kin. fitter
best possible	30.2	29.1
$\sum \Delta R < 1.5$	41.5	40.0
$\sum \Delta R < 3.0$	57.9	55.5
$\sum \Delta R < 4.5$	66.4	63.8

Table 5.7: Comparison of the quality of the selected event interpretation of our method with those of the kinematic fitter. The fraction of selected interpretations which correspond to the best possible one are stated as well as the fractions of selected hypotheses within a certain distance $\sum \Delta R$ with respect to the Monte Carlo true values.

qualify our method are deviations between the reconstructed quantities and Monte Carlo true values on an event by event basis. In table 5.8 the resolution of the transverse momentum, the pseudorapidity and the azimuthal angle ϕ are summarized for the leptonically and hadronically decaying W boson as well as for the two top quarks. The information on the resolution is obtained from a double Gaussian fit (to account for tails) to the difference of the generated and the reconstructed value of the different quantities. The mean value μ and the width σ of the Gaussian with the smaller width are quoted in the table. Furthermore the fraction f_{peak} of events, which are contained in the peak, is given. We define f_{peak} as the fraction of events, which are contained within 2σ of the narrower Gaussian. Not only are the distributions of the pseudorapidities and of ϕ reconstructed well, also the resolution looks reasonable. In case of p_T a shift of the mean value towards smaller values is observed.

	Δp_T [GeV]			$\Delta\eta$			$\Delta\phi$		
	μ	σ	f_{peak}	μ	σ	f_{peak}	μ	σ	f_{peak}
our method									
$W \to \ell\nu$	4.96	12.33	0.82	0.0059	0.23	0.68	0.0009	0.17	0.82
$W \to jj$	-0.23	8.68	0.59	-0.0013	0.08	0.52	-0.0020	0.10	0.58
$top \to b\ell\nu$	4.51	11.43	0.57	-0.0038	0.19	0.51	0.0001	0.12	0.56
$top \to bjj$	1.92	12.92	0.63	-0.0070	0.12	0.55	0.0042	0.13	0.61
kin. fitter									
$W \to \ell\nu$	3.29	13.09	0.80	0.0064	0.20	0.59	0.0022	0.16	0.81
$W \to jj$	-0.48	7.72	0.58	0.0007	0.08	0.53	-0.0021	0.10	0.59
$top \to b\ell\nu$	3.62	12.11	0.56	0.0096	0.21	0.50	0.0017	0.13	0.55
$top \to bjj$	0.44	11.04	0.58	-0.0030	0.13	0.58	0.0063	0.14	0.61

Table 5.8: Comparison of the resolution of the transverse momentum p_T, the pseudorapidity η and the azimuthal angle ϕ of the leptonically and hadronically decaying W boson and of the leptonically and hadronically decaying top quark for our method and for the kinematic fitter. The symbol Δ indicates the difference between the generated and reconstructed quantities. A double Gaussian is fitted to the difference of generated and reconstructed value (to account for tails). The mean value μ and the width σ of the Gaussian with the smaller width are quoted in this table. Furthermore, the fraction f_{peak} of events, which are contained in the peak is given. f_{peak} is defined as the number of events within 2σ of the narrower Gaussian.

Chapter 6

Measurement of the $t\bar{t}$-production

In this chapter the extraction of $t\bar{t}$ signal candidates for the data taken at CDF is described. We give the numbers of $t\bar{t}$ candidates in the lepton + jets channel after applying all selection cuts. The background estimation is taken from the so called "Method 2 calculation" of the CDF lepton + jets group used in the $t\bar{t}$ cross-section measurement [58]. At last we compare different distributions obtained from Monte Carlo simulation with data. The used samples are described in detail in chapter 3.

6.1 Selected $t\bar{t}$ candidates

In table 6.1 and table 6.2 the cut flow is given for each detector component separately. As we need a minimum of four jets to reconstruct $t\bar{t}$ events in the considered lepton + jets channel, the interesting columns are those with four or more jets. After lepton identification, veto cuts and the cut on missing transverse energy we get 207 events. The requirement for one or more secondary vertex tags reduces the event numbers by more than a factor of 2. In the end we get 47 $t\bar{t}$ candidates with an electron, 25 candidates with a CMUP muon and 7 with a CMX muon. Summed over all three detector components 79 $t\bar{t}$ candidates can be used for a further analysis, the complete list with run and event numbers is given in appendix A.3.

Cut	0 jet	1 jet	2 jet	3 jet	**4 jet**	$\geq$ **5** jets	all
Total	499922	380726	325532	42323	**6284**	**928**	1255715
Good Run	315626	238447	203945	26644	**3964**	**578**	789204
CMX Good Total	301507	229035	196139	25576	**3822**	**560**	756639
≥ 1 Tight Std. lepton	315609	118584	14107	2105	**363**	**62**	450830
≥ 1 with add. ID cuts	315609	118451	14074	2096	**361**	**60**	450651
CEM electrons							
Tight Di-Lepton Veto	285410	100523	10591	1449	**256**	**37**	398266
Trigger Path	273744	95964	10155	1396	**250**	**37**	381546
Z Vertex Cut	273499	95877	10147	1396	**250**	**36**	381205
Z veto	265646	85708	8969	1191	**226**	**34**	361774
Cosmic veto	265646	85708	8969	1191	**226**	**34**	361774
Missing Et	177601	17621	2839	467	**115**	**19**	198662
taggable (Info)	0	11754	2474	431	**112**	**19**	14790
b tag ≥ 1	0	248	142	59	**39**	**8**	496

Table 6.1: Cut flow table of $t\bar{t}$ selection for central electrons.

Cut	0 jet	1 jet	2 jet	3 jet	**4 jet**	$\geq$ **5** jets	all
Total	380615	119341	42701	8242	**1288**	**214**	552401
Good Run	242271	75924	27081	5201	**818**	**138**	351433
CMX Good Total	235332	74052	26370	5077	**787**	**137**	341755
$\geq$ 1 Tight Std. lepton	203550	30092	3766	533	**118**	**22**	238081
$\geq$ 1 with add. ID cuts	195015	27693	3528	507	**113**	**20**	226876
CMUP muons							
Tight Di-Lepton Veto	115893	17029	2141	307	**77**	**12**	135459
Trigger Path	115217	16412	1985	290	**65**	**12**	133981
Z Vertex Cut	110987	16293	1966	285	**65**	**12**	129608
Z veto	106608	15735	1884	279	**63**	**11**	124580
Cosmic veto	102089	15707	1879	279	**63**	**11**	120028
Missing Et	87727	8223	1220	193	**45**	**10**	97418
taggable (Info)	0	5390	1049	182	**44**	**9**	6674
b tag $\geq$ 1	0	106	62	24	**18**	**7**	217
CMX muons							
Tight Di-Lepton Veto	68464	9252	1142	151	**25**	**8**	79042
Trigger Path	54980	7474	926	120	**21**	**4**	63525
Z Vertex Cut	49896	7320	902	116	**20**	**4**	58258
Z veto	48144	7105	871	114	**20**	**4**	56258
Cosmic veto	47686	7096	871	113	**20**	**4**	55790
Missing Et	40762	3510	527	77	**15**	**3**	44894
taggable (Info)	0	2361	456	71	**14**	**3**	2905
b tag $\geq$ 1	0	60	27	8	**5**	**2**	102

Table 6.2: Cut flow table of $t\bar{t}$ event selection for muon events.

6.2 Background estimates

After the selection of $t\bar{t}$ candidates the sample still includes background events. The background processes to be considered are W boson plus jets production and QCD processes. We consider two different types of W-production. On the one hand the jets originating from light quarks, then one jet has to be misidentified as a b jet (mistags). On the other hand one or more jets originate from a c- or b quark (W + heavy flavor events). The third type of events are QCD processes where one jet fakes an electron and another jet is misidentified as a b quark jet. (QCD background). The last very small contributions of background stems from di-boson and single top production (Electroweak backgrounds).
This estimation is taken from the so called "Method 2 calculation" of the CDF lepton + jets group used in the $t\bar{t}$ cross-section measurement [58]. In the following a short description for each background is given:

- **Mistag Rate**
  "Mistags" are b-tagged events where a jet which did not result from the fragmentation of a heavy quark is tagged due to measurement errors of the secondary vertex position. This error is mostly caused by tracks which are displaced due to tracking errors, although there are other contributions like nuclear interactions with the detector material as well. Because the secondary vertex tagger algorithm is symmetric in its treatment of the impact parameter d_0 and the decay length significance, the mistags should occur at the same rate for positive and negative tags. Therefore a good estimate of the positive mistag rate can be obtained from the negative tag rate. The rate of negative tags for taggable jets is measured in an inclusive sample of jet triggers. The rate is parameterized as a function of four jet variables - number of taggable tracks, the raw jet E_T , the η and ϕ of the jet - and one event variable, the sum of the E_T for all jets in the event with $E_T > 10$ GeV and $|\eta| < 2.4$. This so-called mistag matrix [54] is used to obtain the probability that a jet will be negatively tagged.
  There are several corrections applied to the mistag estimate. The negative tag rate contains contributions from jets with heavy flavor contents and the used sample contains contamination from $t\bar{t}$ events, which has a significant effect in events with four jets.

- **QCD (non-W) background**
  The non-W QCD background is a mixture of events where the lepton does not come from the decay of a W- or Z-boson. These include lepton and missing energy fakes as well as semileptonic b hadron decays. Since several backgrounds are calculated by normalizing to the number of W + jets events before tagging, it is necessary to understand the level of QCD contamination in this so-called pretag sample. In addition, some of these non-W QCD events may be b-tagged. Both the pretag and tagged

contributions are measured directly from data events. In a leptonic W decay, the lepton is isolated and there is large $\not\!\!E_T$ due to the neutrino, while in non-W events this is not necessarily true. We define the lepton isolation `Isol` as the ratio of energy (not due to the lepton) in the calorimeter in a cone around the lepton direction to the measured lepton energy, see section 5.1.1. Isolated leptons will have small values of `Isol` . Sideband regions for lepton isolation and $\not\!\!E_T$ in the high-p_T lepton sample contain mostly non-W events and are used to extrapolate QCD expectations into the signal region. The sideband regions are defined as follows, see also figure 6.1:

1. Region A: `Isol` > 0.2 and $\not\!\!E_T < 15$ GeV
2. Region B: `Isol` < 0.1 and $\not\!\!E_T < 15$ GeV
3. Region C: `Isol` > 0.2 and $\not\!\!E_T > 20$ GeV
4. Region D (W signal region): `Isol` < 0.1 and $\not\!\!E_T > 20$ GeV

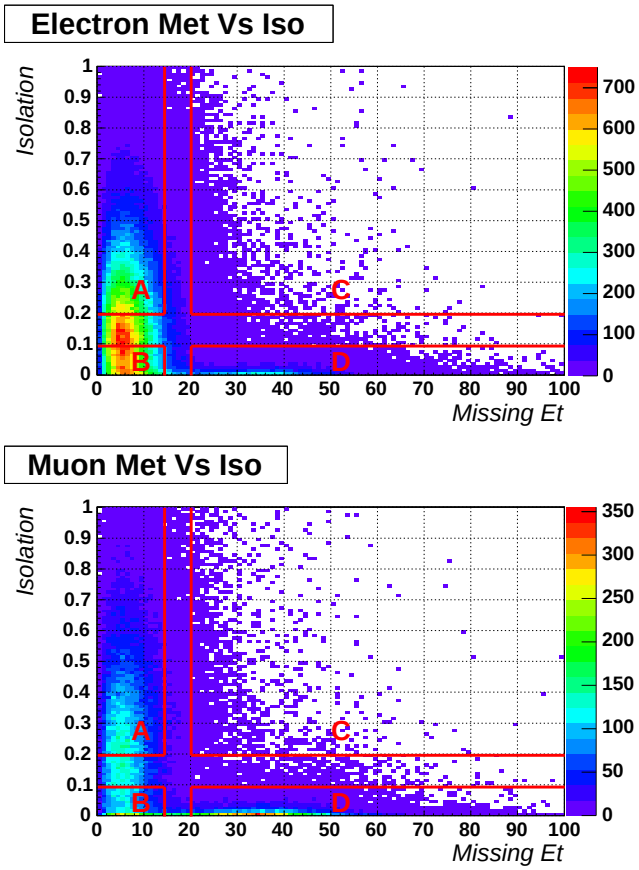

Figure 6.1: Pretag events in Regions A,B,C,D for electrons and muons.

For the QCD background these two variables are assumed to be mostly uncorrelated: the ratio of non-W events at low and high `Isol` values in

the low $\not\!\!E_T$ region is the same as in the high $\not\!\!E_T$ region. The number of non-W events in the signal region is estimated by

$$\frac{N_A}{N_B} = \frac{N_C}{N_D} \implies QCD = N_D = \frac{N_B \cdot N_C}{N_A} \tag{6.1}$$

The contribution of true W and $t\bar{t}$ events in the sideband regions is estimated using Monte Carlo samples to determine the ratio of W and $t\bar{t}$ in the signal and sideband regions, and normalized to the observed number of events in the pretag signal region. The correction is 5-30% depending on the lepton type and event jet multiplicity.

- **W+heavy flavor events**
  The W+heavy flavor events $Wb\bar{b}$, $Wc\bar{c}$, Wc are the second largest background components. One of the main strengths of Method 2 is a technique for estimating these flavor processes via Monte Carlo and solving normalization problem: the Monte Carlos are used to derive a flavor fraction, and the background normalization stems from multiplying the number of pretag W +jets events by the flavor fraction of $Wb\bar{b}$, $Wc\bar{c}$ and Wc events, see reference [59]. The number of pretag events is corrected for QCD and electroweak (WW, etc.) backgrounds. The heavy flavor fraction is based on Monte Carlo, and at present the Run I fractions are used [60]. The number of tagged events is derived by multiplying the pretag flavor components by the tagging efficiencies based on Run II MC samples, corrected for b tag scale factor.

- **Electroweak backgrounds and Single Top** The normalization of the diboson and single top backgrounds is based on the theoretical cross sections [62], the measured luminosity and the acceptance and b-tagging efficiency derived from Monte Carlo. The different processes which are considered are listed in table 6.3. The samples are normalized to a luminosity of $318.5 pb^{-1}$ for CEM and CMUP events and $305.2 pb^{-1}$ for CMX. The Monte Carlo acceptance is corrected for lepton identification, trigger efficiencies and z vertex cut. The tagging efficiency is scaled by the Monte Carlo/data scale factor.

In table 6.4 a summary of the background estimates is given. For events with four or more jets the number of expected background events is 10.3 ± 1.9. To model the background shape of the different distributions of the interesting variables we use two different Monte Carlo samples. For the QCD and mistag background we use a W + four light quark jets sample and for all other backgrounds with heavy flavor contents, a W + two b quark jets + two light quark jets sample is used.

Process	Theoretical Cross Section
WW	13.25 ± 0.25 pb
WZ	3.96 ± 0.06 pb
ZZ	1.58 ± 0.02 pb
Single top W^*	0.88 ± 0.05 pb
Single top $W - g$	1.98 ± 0.08 pb

Table 6.3: Theoretical cross sections for electroweak backgrounds.

Jet multiplicity	1 jet	2 jets	3 jets	$\geq$ **4 jets**
QCD (non$W$)	42.3 ± 10.1	19.3 ± 4.8	6.7 ± 1.9	$\mathbf{3.7 \pm 1.1}$
Mistags	94.1 ± 19.3	39.1 ± 7.9	11.1 ± 2.2	$\mathbf{2.5 \pm 0.5}$
$W + c$	99.2 ± 26.6	21.1 ± 6.0	3.2 ± 1.0	$\mathbf{0.5 \pm 0.2}$
$W + c\bar{c}$	33.5 ± 10.2	20.1 ± 6.6	4.9 ± 1.7	$\mathbf{0.8 \pm 0.4}$
$W + b\bar{b}$	98.7 ± 32.4	55.1 ± 17.9	10.9 ± 3.4	$\mathbf{1.8 \pm 0.8}$
EW	4.5 ± 0.7	8.5 ± 1.3	2.1 ± 0.3	$\mathbf{0.5 \pm 0.1}$
Single Top	6.9 ± 1.7	11.6 ± 2.4	2.5 ± 0.5	$\mathbf{0.5 \pm 0.1}$
Total	379.1 ± 72.5	174.8 ± 32.0	41.4 ± 6.8	$\mathbf{10.3 \pm 1.9}$

Table 6.4: Summary of background estimates. The errors are added in quadrature.

6.3 Kinematic distributions

In this section the comparison between the measured data and the expected distribution given by the Monte Carlo simulation is done. The data are taken after applying all selection cuts, described in detail in section 5.1, including a minimum of one secondary vertex tag. After all cuts we get 79 $t\bar{t}$ candidates. The numbers of the expected background are taken from the estimates described one section before. For the QCD and "mistags" summed background we expect 6.2 ± 1.2 events, for all other backgrounds with heavy flavor content or diboson production we expect 4.1 ± 0.9 events. The difference between the expected background number and the number of $t\bar{t}$ candidates is taken as the $t\bar{t}$ content. A summary of the used numbers and samples is given in table 6.5. In the following plots the data events are drawn with red crosses and error bars represent the statistical errors. The QCD and mistag background is drawn in yellow, the remaining diboson and heavy flavor background in blue and the $t\bar{t}$-signal in light gray. All three histograms are drawn stacked to one histogram forming the expected shape for each variable.

The Monte Carlo distributions are created with the reconstructed event interpretation. This means that all events, signal and background, have to survive all selection cuts and that event interpretation is considered which is marked best by our selection procedure.

Process	Expected events	MC sample (electron/muons)
QCD & Mistags	6.1 ± 1.2	atop7a / atoppb
Electroweak and heavy flavor	4.1 ± 0.9	atopfb / atopjb
$t\bar{t}$	68.8 ± 1.5	ttopel

Table 6.5: Number of expected events and used samples for the background and signal modeling.

There are no discrepancies between the expected distributions and the measured data within statistical fluctuations.

- **Lepton**
  In figure 6.2 the transverse momentum, the pseudorapidity and the azimuthal angle ϕ of the reconstructed lepton are shown. All three plots show no discrepancies between the simulated and measured values within the statistical errors.

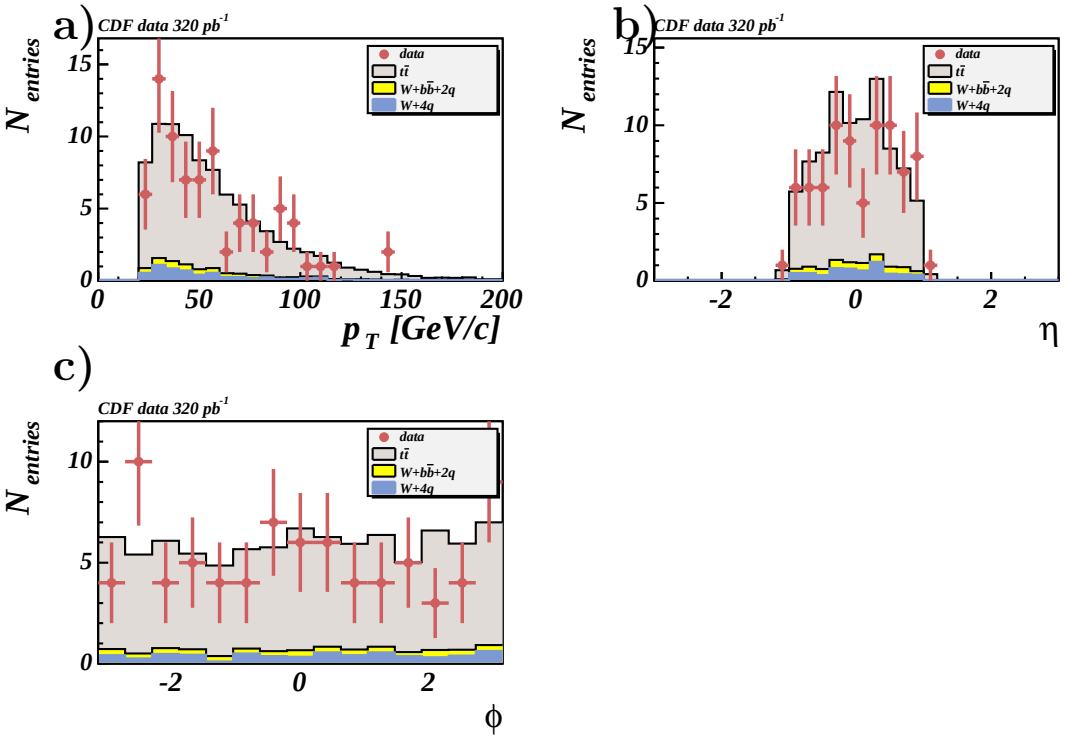

Figure 6.2: Comparison of the reconstructed **lepton** between data (red crosses) and Monte Carlo generated events (stacked histogram - yellow : W + four light quark jets, blue : W + two light quark jets + two b quark jets, gray : $t\bar{t}$). (a) transverse momentum, (b) pseudorapidity and (c) azimuthal angle ϕ of the **leptons**.

- **Leptonically decaying W boson**
  In figure 6.3 the transverse momentum, the pseudorapidity and the azimuthal angle ϕ of the leptonically decaying W boson are shown. Additionally we compare the distribution of the electron decay angle of the measured data with the expected one. We see, that also the decay of the W boson is reconstructed well in data.

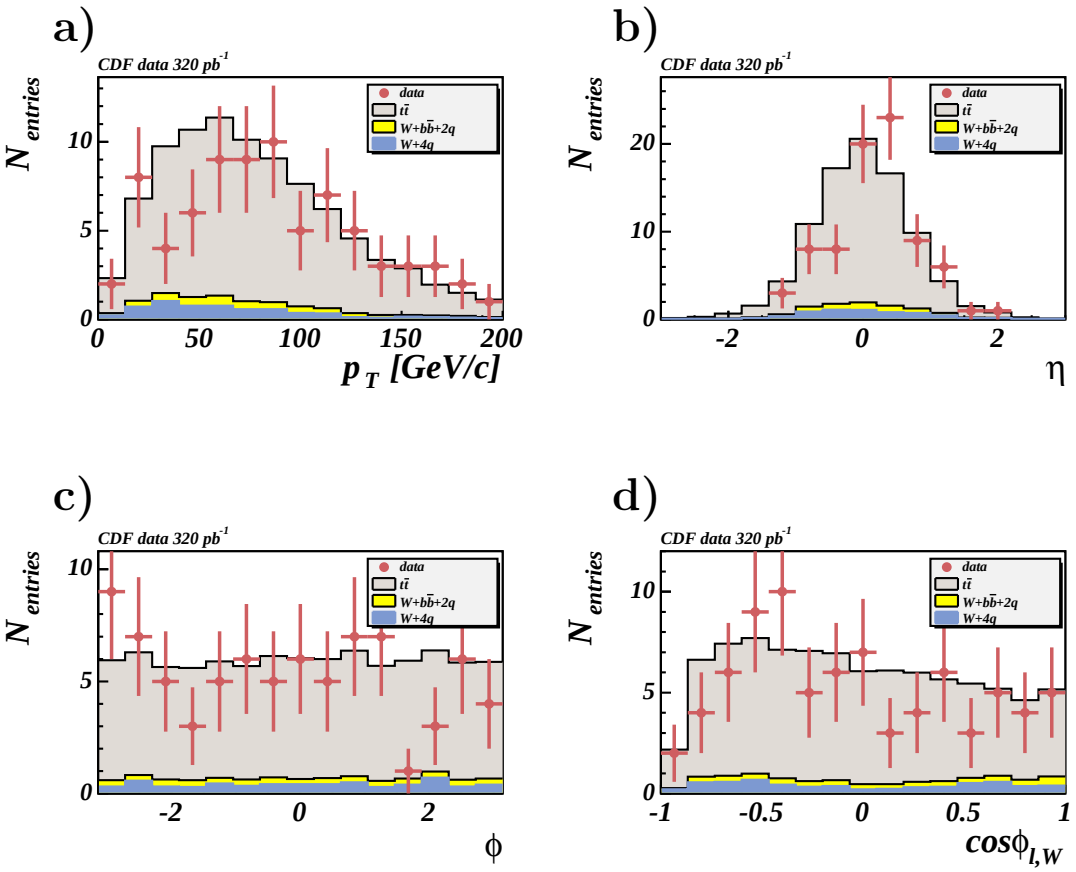

Figure 6.3: Comparison of the reconstructed **leptonically decaying W boson** between data (red crosses) and Monte Carlo generated events (stacked histogram - yellow : W + four light quark jets, blue : W + two light quark jets + two b quark jets, gray : $t\bar{t}$). (a) transverse momentum, (b) pseudorapidity, (c) azimuthal angle ϕ and (d) cosine of electron decay angle in W boson rest frame.

- **Hadronically decaying W boson**
  In figure 6.4a-c the transverse momentum, the pseudorapidity and the azimuthal angle ϕ of the hadronically decaying W boson are shown. As the Monte Carlo simulations predicted the η distribution is broader than for the leptonically decaying W boson. Since the η-range of the substitutants is wider we can measure higher values. For all three variables the data fits well to the simulated values. The reconstructed mass and the jet angle in the W boson rest frame are shown in figure 6.4d,e. The W boson mass can be reconstructed well in the data, also the decay of the W boson does not show any deviation.

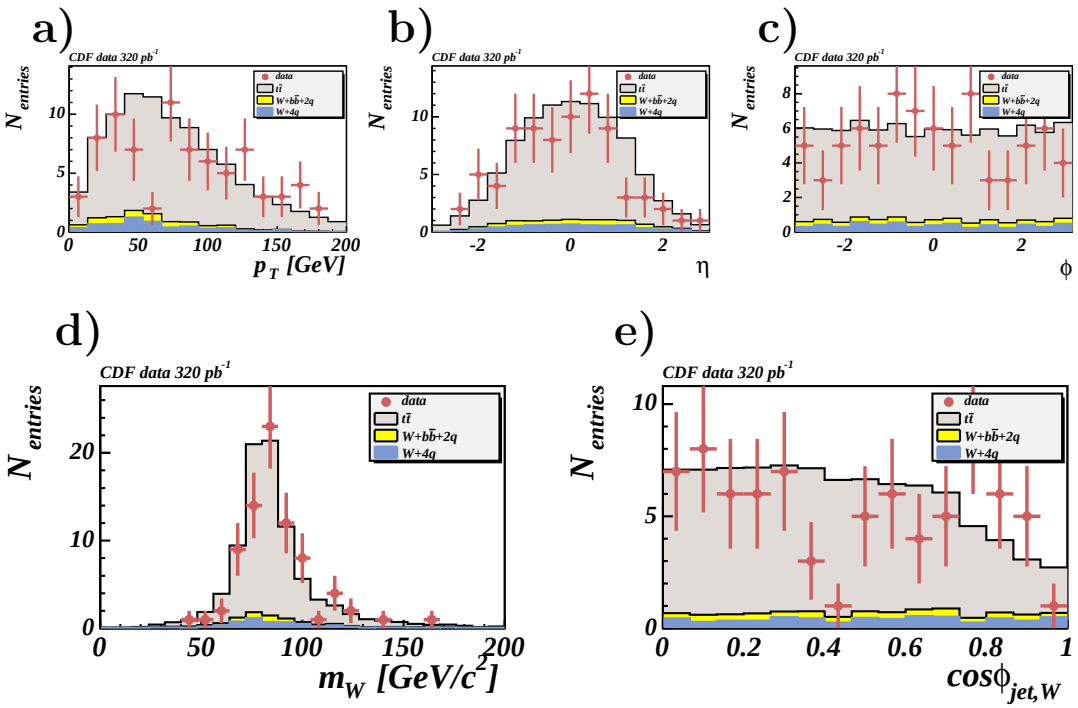

Figure 6.4: Comparison of the reconstructed **hadronically decaying W boson** between data (red crosses) and Monte Carlo generated events (stacked histogram - yellow : W + four light quark jets, blue : W + two light quark jets + two b quark jets, gray : $t\bar{t}$). (a) transverse momentum, (b) pseudorapidity, (c) azimuthal angle ϕ, (d) reconstrcuted mass and (e) cosine of jet angle in W boson rest frame.

- **Top quark decaying further into leptonically decaying W boson** In figure 6.5 the transverse momentum, the pseudorapidity and the azimuthal angle ϕ of the leptonically decaying top quark are shown. In contrast to the W boson the statistical fluctuations in the transverse momentum distribution are higher, but still in accordance with the expected distribution. The reconstructed mass and the W boson decay angle in the top quark rest frame are shown in figure 6.5d,e. Like the distribution of the transverse momentum the distribution of the reconstructed mass has a lot of statistical fluctuations. In the next section we will perform a fit of the top quark mass after background subtraction.

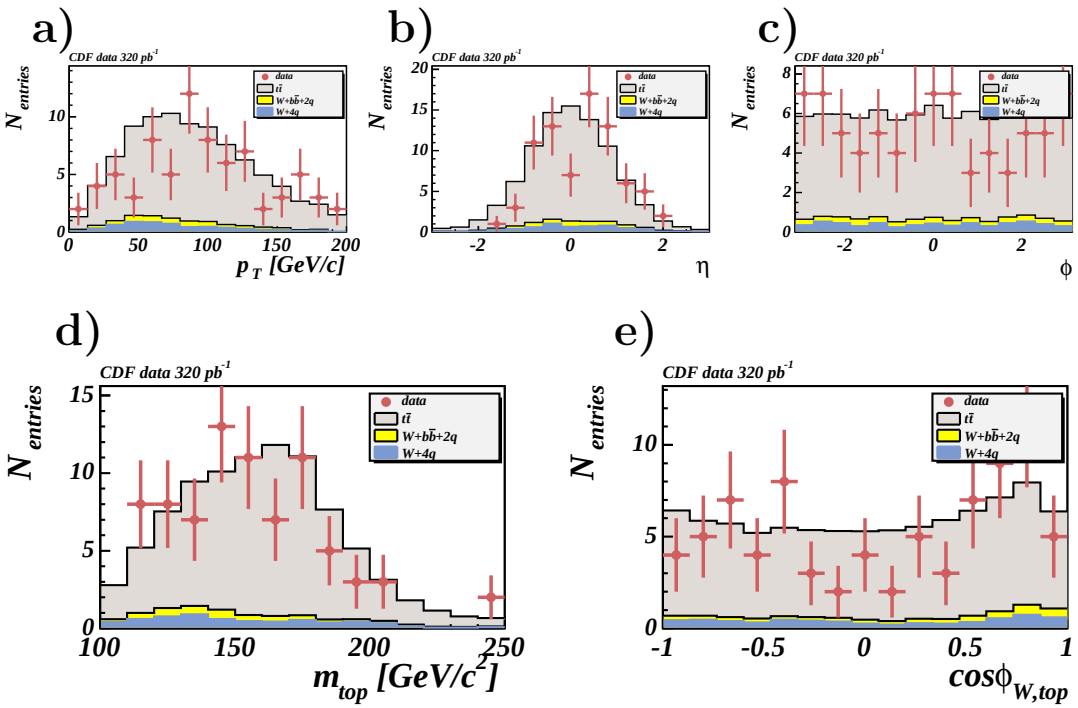

Figure 6.5: Comparison of the reconstructed **leptonically decaying top quark** between data (red crosses) and Monte Carlo generated events (stacked histogram - yellow :W + four light quark jets, blue :W + two light quark jets + two b quark jets, gray :$t\bar{t}$). (a) transverse momentum, (b) pseudorapidity, (c) azimuthal angle ϕ, (d) reconstrcuted mass and (e) cosine of the W boson angle in top quark rest frame.

- **Top quark decaying further into hadronically decaying W boson** In figure 6.5 the transverse momentum, the pseudorapidity and the azimuthal angle ϕ of the hadronically decaying top quark are shown. The transverse momentum distribution has also a lot of statistical fluctuation as we have seen for the leptonically decaying top quark. In figure 6.5d,e the reconstructed mass and the W boson decay angle in the top quark rest frame are shown. As well as the mass of the leptonically decaying top quark the mass of the hadronically decaying top quark and the decay angle of the W boson can be reconstructed well.

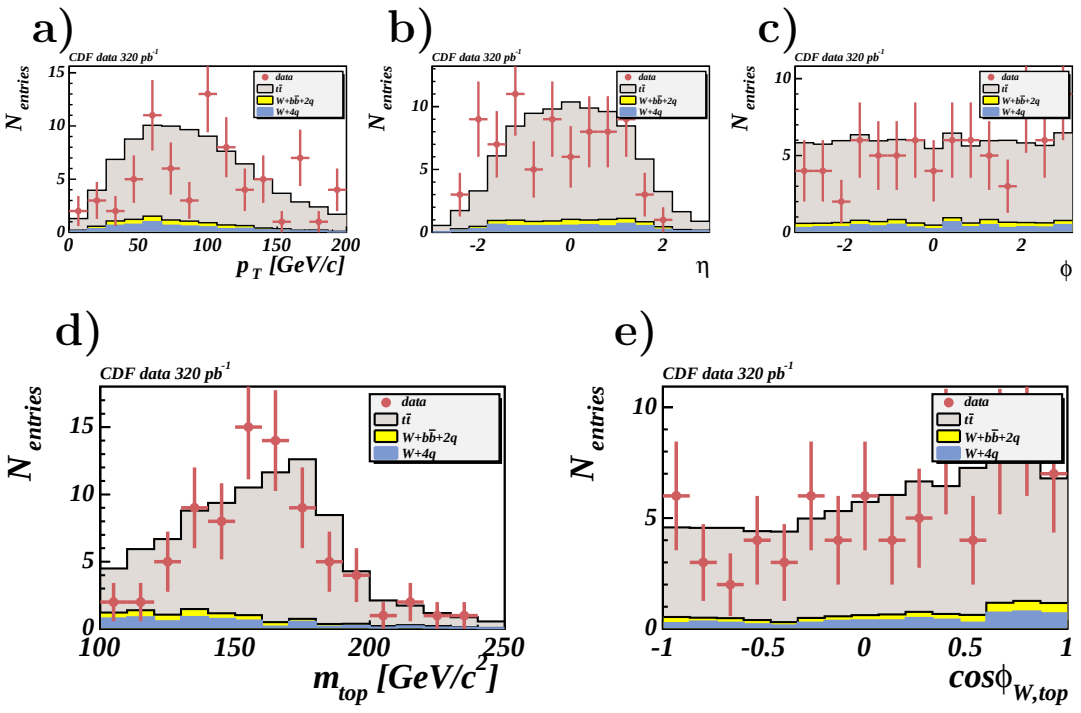

Figure 6.6: Comparison of the reconstructed **hadronically decaying top quark** between data (red crosses) and Monte Carlo generated events (stacked histogram - yellow :W + four light quark jets, blue :W + two light quark jets + two b quark jets, gray :$t\bar{t}$). (a) transverse momentum, (b) pseudorapidity, (c) azimuthal angle ϕ, (d) reconstrcuted mass and (e) cosine of the W boson angle in top quark rest frame.

6.4 Check of the reconstructed top quark mass

In this section we will fit the reconstructed top quark masses. This is not supposed to be a real measurement of the masses but a consistency check of our reconstruction and selection procedure. Starting with the leptonically decaying top quark, the reconstructed top quark mass of the 79 $t\bar{t}$ candidates is plotted in figure 6.7a with red crosses. The estimated background is drawn like in the section before. The blue filled part represents the QCD and mistag background and the yellow filled one represents all other backgrounds including heavy flavor and electroweak processes. In figure 6.7b the estimated background is subtracted from the data events. Then this "signal" histogram is fitted with a Gaussian to extract the top quark mass. Unfortunately the data are spread over a wide range and the width becomes very bad. The result is a mean of ~ 152.6 GeV/c^2 with a width of about 28.4 GeV/c^2.

The second top quark, decaying hadronically, is shown in figure 6.7c. The data (red crosses) and the estimated background (yellow and blue) are drawn in the same way as for the leptonically decay top quark. The Gaussian fit after background subtraction gives a mean value of about 160.0 GeV/c^2 with a width of about 19.1 GeV/c^2. As we have seen in the section before the hadronically decaying top quark can be reconstructed better than the leptonically decaying one. A short overview of the fit results is given in table 6.6.

We can conclude that our reconstruction and selection procedure works also

	μ [GeV/c^2]	σ [GeV/c^2]
$m_{top\to b\ell\nu}$	152.6 ± 4.1	28.4 ± 3.3
$m_{top\to bjj}$	160.1 ± 2.5	19.1 ± 1.8

Table 6.6: Summary of the fit of the reconstructed top quark mass measured after background subtraction.

well on real data. We do not see big deviations in the considered variables of all reconstructed particles, neither in variables sensitive to the energy reconstruction nor in variables sensitive to the kinematic reconstruction. Also as a final test, the reconstructed top quark masses are in the expected range, whereas the values are smaller than the expected value. The reason for this is, that we do not use top specific jet corrections. The width are comparable to the expected values within the statistical errors.

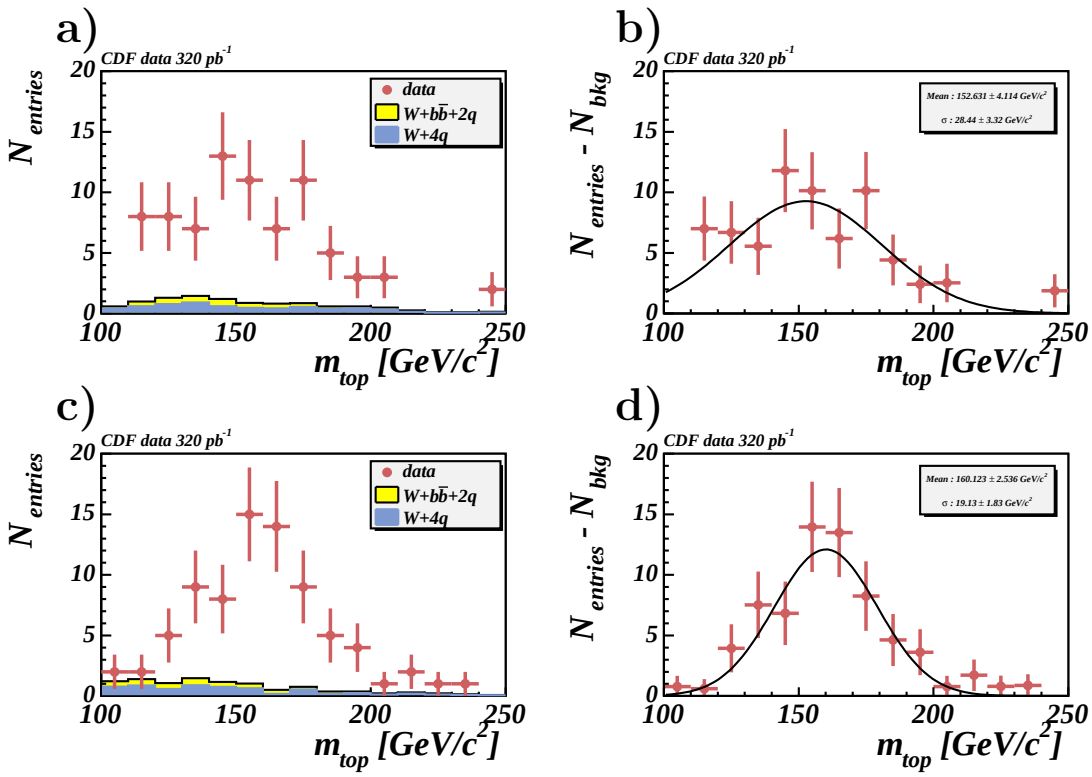

Figure 6.7: Reconstructed mass of the leptonically decaying top quark. Figure a) with measured data and estimated background, figure b) with subtracted background and Gaussian fit.Reconstructed mass of the hadronically decaying top quark. Figure c) with measured data and estimated background, figure d) with subtracted background and Gaussian fit.

Chapter 7

Measurement of the W Helicity in top quark decays

In this chapter we describe our measurement of the W helicity in top quark decays. In the first section we give a detailed description of the reconstruction and resolution of the measured angle. In the following section we perform a separate analysis for all three detector components (CEM, CMUP, CMX), because the different acceptances modify the reconstructed distribution. Afterwards we add all three detector components and perform a combined measurement of the fraction of the W boson polarizations. The analysis is done in the following five steps.

1. Determination of the transfer function τ. The transfer function transforms the measured distribution into a distribution, which can be compared to theoretically expected distributions.

2. Multiply each bin i of the data as well as of the background with the value of the corresponding bin of the transfer function.
   $N_{final}(i) = N_{signal}(i) \cdot \tau(i)$.

3. Add up the histograms of all three detector components.
   $\sum_{j=CEM,CMUP,CMX} N(i)_{j,final}$

4. Perform a binned likelihood fit with the fraction of the longitudinally polarized W bosons as a free parameter.

5. Perform a binned likelihood fit with the fraction of the right-handed polarized W bosons as a free parameter.

At the end of the chapter we investigate the consistency of our method using pseudo experiments and determine systematic uncertainties.

7.1 Reconstruction and Resolution of the W Helicity Angle

To determine the helicity angle of the W boson in top quark decays, we consider the decay angle of the lepton momentum in the W boson rest frame with respect to the W boson momentum in the top quark rest frame. Therefore, the reconstructed fourvectors of the top quark and the W boson are required. In figure 7.1 a schematic view of the helicity angle is given. To reconstruct this angle

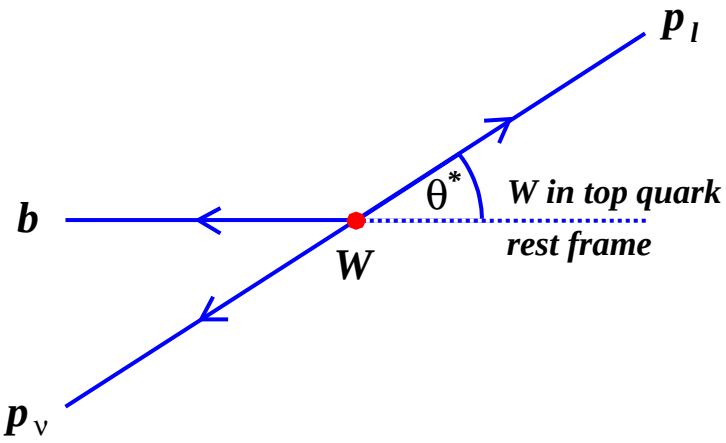

Figure 7.1: Schematic view of the helicity angle $\cos\theta^*$.

from the measured fourvectors in the lab frame we have first to boost the lepton fourvector and the W boson fourvector into the top quark rest frame. After this we boost the lepton fourvector into the W boson rest frame. The helicity angle $\cos\theta^*$ can then be calculated as the angle between the lepton fourvector and the boostvector from the top rest frame into the W boson rest frame. The theoretical expected distributions of the helicity angle for the different polarizations of W bosons are given in equations 7.1 - 7.3, for more details see section 1.2.3.

$$|\mathcal{M}_{W,long}|^2 \sim \frac{3}{4}(1-\cos^2\theta^*) \tag{7.1}$$

$$|\mathcal{M}_{W,left}|^2 \sim \frac{3}{8}(1-\cos\theta^*)^2 \tag{7.2}$$

$$|\mathcal{M}_{W,right}|^2 \sim \frac{3}{8}(1+\cos\theta^*)^2 \tag{7.3}$$

The partonic distribution, calculated with true values of the Monte Carlo and without any cuts, of the helicity angle is shown in figure 7.2. To measure the fraction of longitudinally polarized W bosons F_0 we fit the following function to the distribution:

$$f_{fit} = F_0 * \frac{3}{4}(1-\cos^2\theta^*) + (1-F_0) * \frac{3}{8}(1-\cos\theta^*)^2 \tag{7.4}$$

The fraction F_+ of right-handed polarized W bosons is set to 0 as given in the Standard Model. The fit gives a value of $F_0 = 0.705 \pm 0.002$ for the ratio of longitudinally polarized W bosons. We can conclude that the polarization in the top quark decay is implemented in the Monte Carlo generator as it is predicted in the Standard Model, compare with figure 1.7.

To determine the resolution of our reconstruction we plot the reconstructed

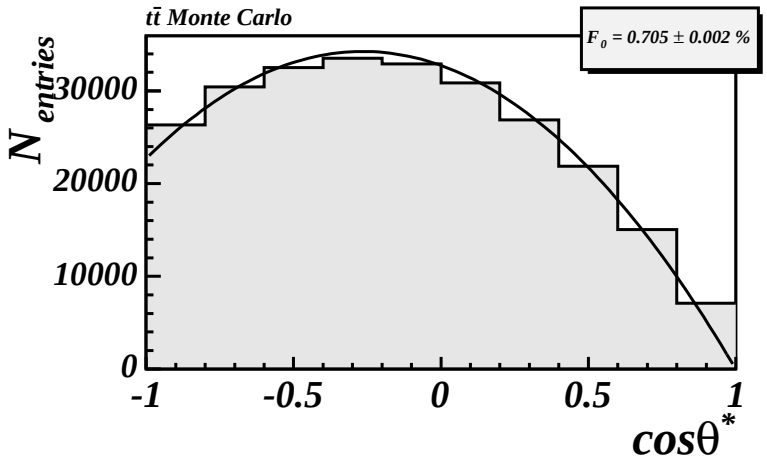

Figure 7.2: Partonic distribution of the helicity angle $\cos\theta^*$ without any cuts. We fit the fraction of longitudinal polarized W bosons F_0.

value of the helicity angle $\cos\theta^*_{reco}$ versus the generated one of the Monte Carlo true values $\cos\theta^*_{mc}$. This is shown in figure 7.3. Most events can be reconstructed well lying on the line $\cos\theta^*_{reco} = \cos\theta^*_{mc}$. But there is also a spread for a given value of $\cos\theta^*$. To deduce a sensible number of bins for our data analysis we divide the two-dimensional plot into 10 slices for different Monte Carlo values and plot for each of them the difference between the produced and the reconstructed helicity angle in a separate histogram. This is shown in figure 7.5. For each slice we perform a Gaussian fit and enter the obtained width in figure 7.4. All values except slice 6 are smaller than 0.4. Therefore, we decide to use 5 bins as a proper value for binning the data.

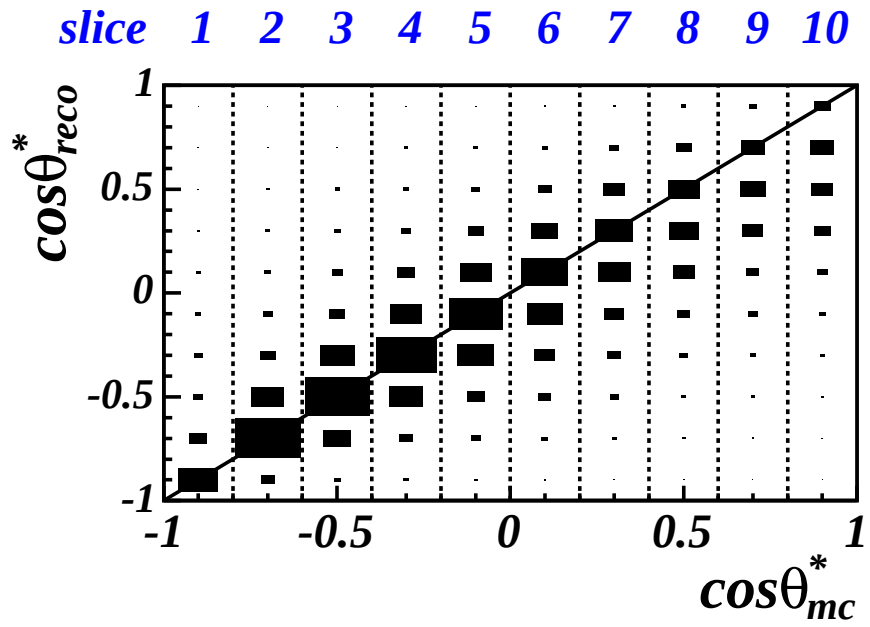

Figure 7.3: $\cos\theta^*_{reco}$ *vs.* $\cos\theta^*_{mc}$. $\cos\theta^*_{mc}$ is calculated using true values generated in the Monte Carlo, $\cos\theta^*_{reco}$ is calculated after complete reconstruction and our selection procedure.

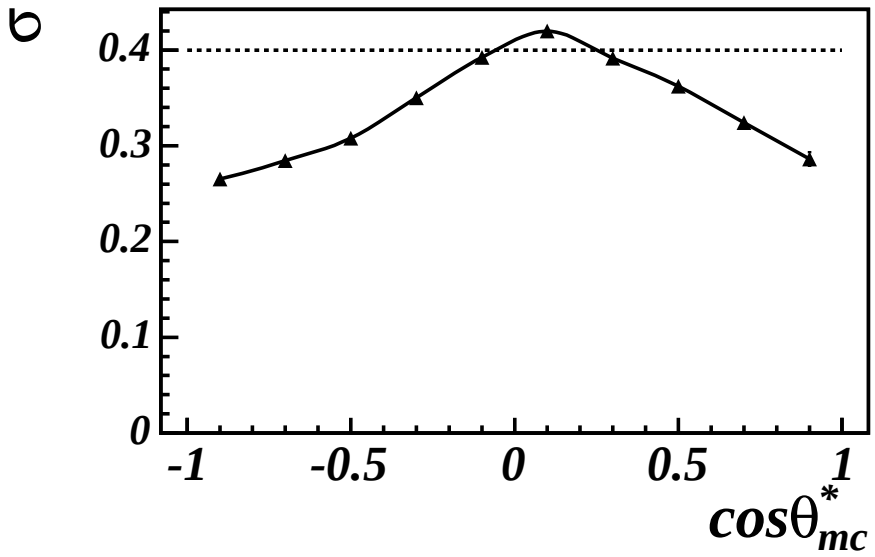

Figure 7.4: Width σ of the Gaussian fit of $\cos\theta^*_{mc} - \cos\theta^*_{reco}$ for each slice.

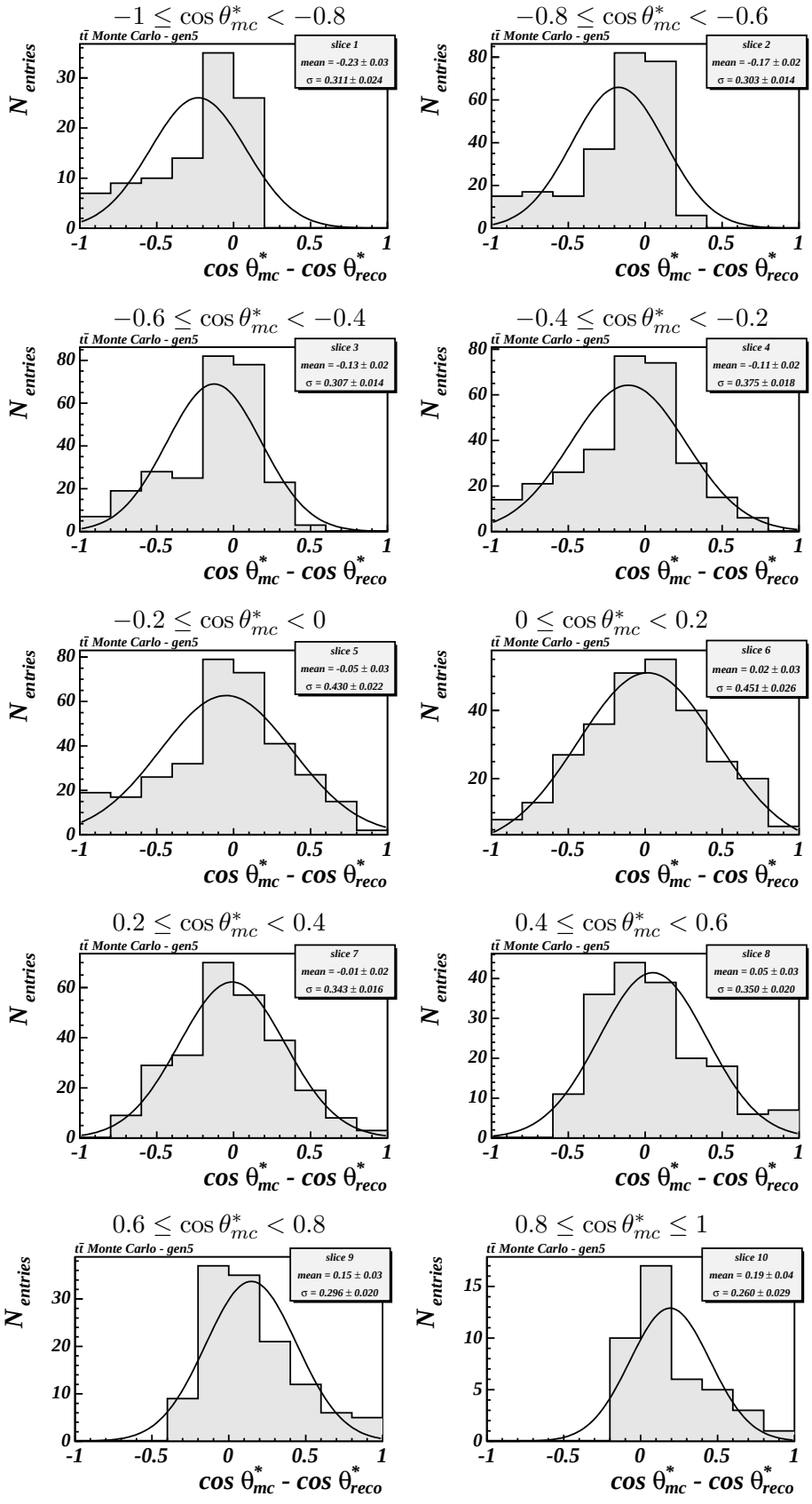

Figure 7.5: Difference between the Monte Carlo truth and the reconstructed value of the helicity angle $\cos\theta^*$ for different regions. A Gaussian fit is performed to get the width of the distributions.

7.2 Determination of the acceptance and reconstruction correction

Due to detector effects and different acceptances in different regions of phase space, a measured distribution is not the same as the one at parton level. Therefore, we determine a so called transfer function τ using a Monte Carlo sample. Bin by bin the partonic distribution is divided by the distribution obtained after reconstruction. To understand the different effects modifying the shape of the distribution this is done in two steps. The first step considers only acceptance effects. The second step considers reconstruction effects and mismeasurements that arise from selecting not the best possible event interpretation.

7.2.1 Transfer function for acceptance effects

To show the effect of the lepton selection we divide the distribution resulting after lepton identification by the partonic distribution. For the partonic distribution the helicity angle is calculated with the true Monte Carlo fourvectors. All generated events are considered. To show only effects of the acceptance we calculate the helicity angle still with the Monte Carlo true values but we only consider these events which pass our selection cuts. To take only effects on the shape into account, we scale the partonic distribution to the same integral as the distribution after the selection. One bin of the transfer function τ_{acc} is then calculated by :

$$\tau_{acc}(i) \quad = \quad \frac{N_{acc}(i)}{N_p(i)} \cdot s_{acc} \quad \text{with} \quad s_{acc} = \frac{\sum N_p(i)}{\sum N_{acc}(i)} \tag{7.5}$$

where $N_{acc}(i)$ denotes the contents of bin i of the distribution after lepton identification, $N_p(i)$ the bin contents of the partonic distribution and s_{acc} the scale factor.
The transfer function, showing the acceptance effects, is plotted in figure 7.6. In figures a),c),e) the rescaled partonic distribution (solid gray) and the distribution calculated with the same fourvectors but considering only events after passing lepton identification (hatched) are drawn. The division of both histograms gives the corresponding transfer function, shown in figures 7.6 b),d),f).
As can be seen in figures 7.6 events with $\cos\theta^* \sim -1$ are suppressed. Events with $\cos\theta^* \sim -1$ are events where the b quark from the top quark decay has the same direction as the lepton from the W boson decay, see figure 7.1. Due to the isolation cut applied to the leptons, all events are rejected where an electron is close to a jet in a cone of 0.4. No isolated electron is allowed to be in a jet.

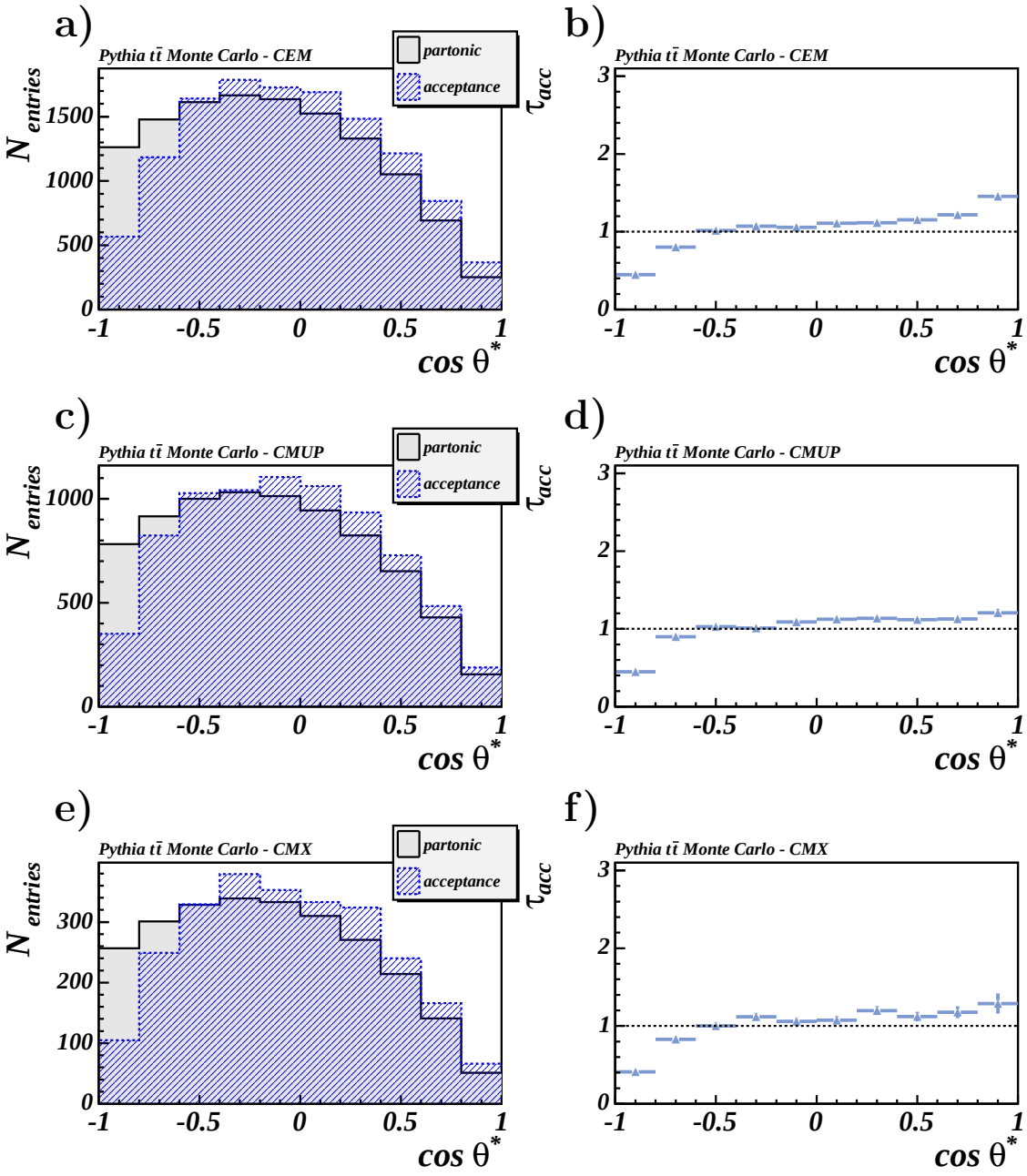

Figure 7.6: a),c),e) Partonic distribution of the helicity angle (solid gray) and distribution after CEM electron, CMUP muon and CMX muon identification (sketched blue), respectively. The helicity angle θ^* is still calculated with Monte Carlo true values. The appropriate transfer functions b),d),f) show the division of both histograms.

7.2.2 Transfer function for reconstruction effects

The effect of the reconstruction and selection of one event interpretation is investigated by creating a second transfer function τ_{reco}. This function is constructed by dividing bin by bin the distribution calculated with full reconstructed fourvectors after all cuts, $N_{reco}(i)$, and the distribution we got after the electron identification calculated with Monte Carlo true values, $N_{acc}(i)$. Again the latter is scaled to the same integral as the distribution after reconstruction.

$$\tau_{reco}(i) \quad = \quad \frac{N_{reco}(i)}{N_{acc}(i)} \cdot s_{reco} \quad \text{with} \quad s_{reco} = \frac{\sum N_{acc}(i)}{\sum N_{reco}(i)} \tag{7.6}$$

The effect of the detector reconstruction and selection procedure is shown in figure 7.7a),c),e). Here both helicity angle distributions after lepton identification (hatched) and after reconstruction (red crosses) are separately shown for each detector component. Figure 7.7 b),d),f) shows the corresponding transfer functions. These transfer functions show that too many events with $\cos\theta^* \sim -1$ and $\cos\theta^* \sim 1$ are reconstructed. This is explained by the following effects:

1. **cos$\theta^* \sim -1$:** Going back to figure 7.1 we find that $\cos\theta^* \sim -1$ corresponds to events where the lepton has the same direction as the b quark of the jet. Due to the fact that the reconstructed jet axis of the b jet does not point perfectly into the direction of the original b quark the isolation is smeared out. This does not mean that the isolation between the lepton and the jets are softened but the reconstruction of the helicity angle uses the jet and not the original b quark.

2. **cos$\theta^* \sim 1$:** In this case the b quark points into the same direction as the neutrino from the W decay. From studies using the true values of the b quark direction and energy we conclude that the difference for $\cos\theta^* \sim 1$ is caused by mismeasurements of the missing transverse energy and therefore the imperfect reconstruction of the neutrino.

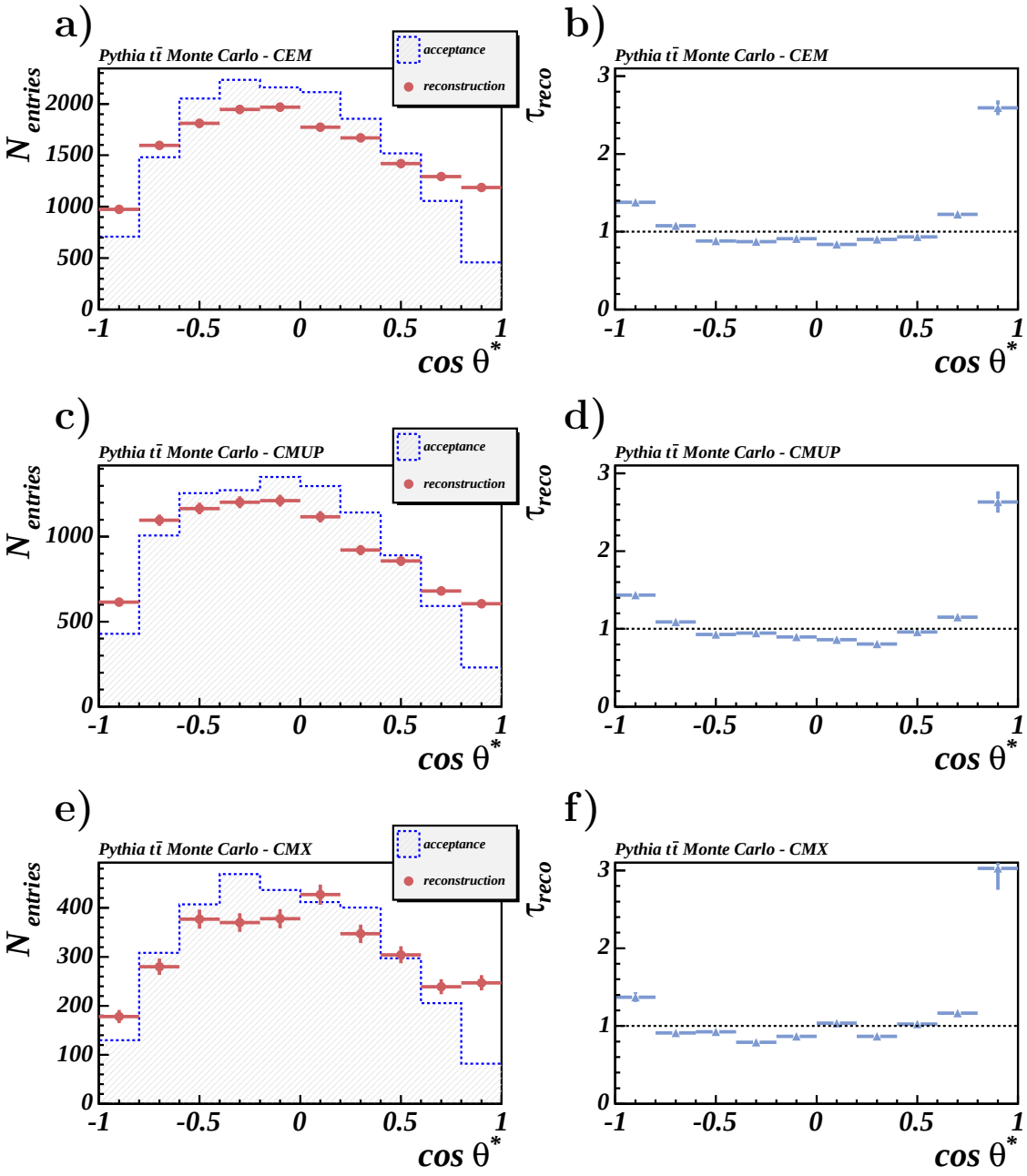

Figure 7.7: a),c),e) Rescaled distribution of the helicity angle after lepton identification calculated with true Monte Carlo values (hatched) and helicity angle distribution after complete reconstruction and selection of one event interpretation (red crosses). The appropriate transfer functions b),d),f) are the division of both histograms.

7.2.3 Transfer function for measured data

The resulting transfer function for the measured data do not use the intermediate step. We determine only one transfer function τ calculated by dividing bin by bin the partonic distribution N_p and the distribution of the helicity angle after complete reconstruction N_{reco}. This ratio is multiplied by a scale factor s normalizing the partonic distribution to the distribution after reconstruction.

$$\tau(i) \quad = \quad \frac{N_p(i)}{N_{reco}(i)} \cdot s \quad \text{with} \quad s = \frac{\sum N_{reco}(i)}{\sum N_p(i)} \tag{7.7}$$

In figure 7.8 the resulting transfer functions are given for each detector component separately using the bin width of $\cos\theta^*$ (=5) deduced in chapter 7.1.

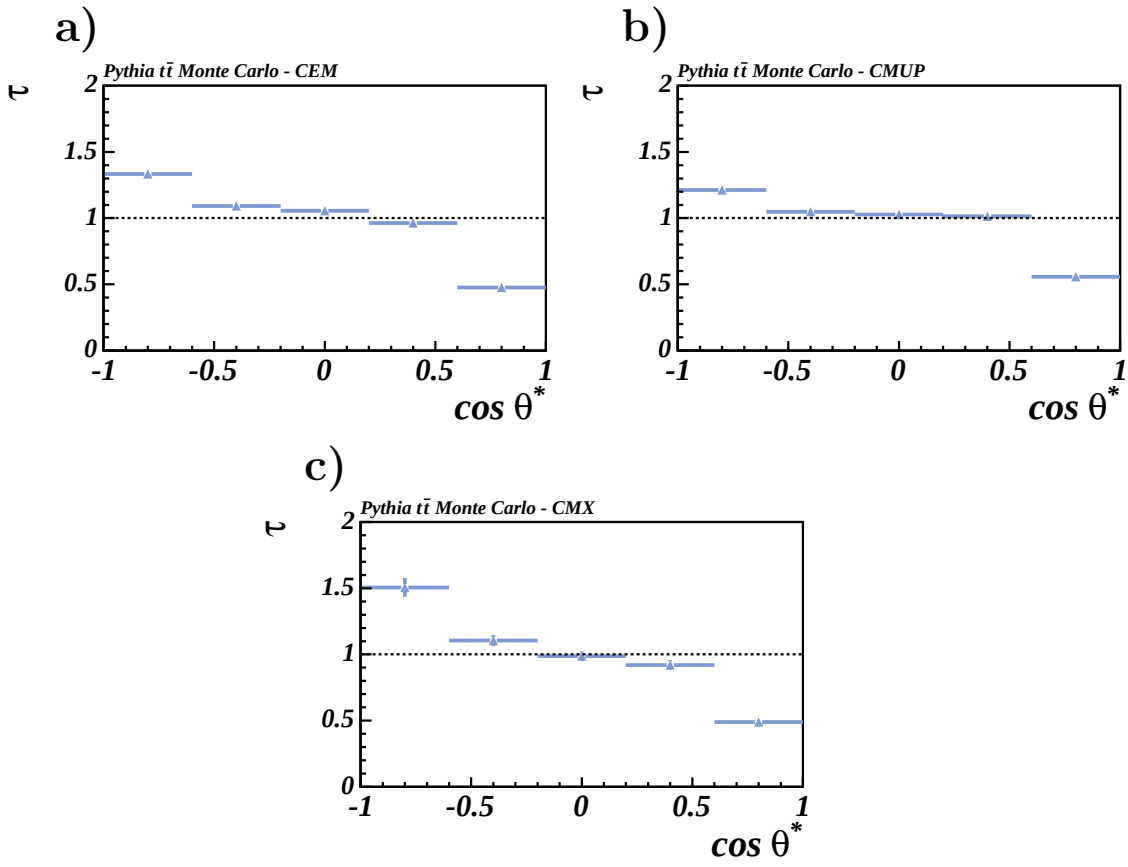

Figure 7.8: a) Transfer function from partonic distribution to full reconstruction for a) CEM electrons, b) CMUP and c) CMX muons. The transfer function is calculated by dividing the partonic distribution of the helicity angle by the distribution after complete reconstruction.

7.3 Determination of the helicity fractions

In this section we will measure the polarizations of the W boson in CDF data. We will start with a separate analysis for the different detector components, combine them afterwards and determine the helicity fractions of the longitudinally polarized W bosons as well as the fraction of right-handed polarized W bosons in a second fit.

7.3.1 Separate Analysis for CEM, CMUP, CMX

Before we fit the data to the theoretically expected distributions for the W boson polarization we multiply the data as well as the background templates with the transfer function τ. Figure 7.9 shows the helicity angle $\cos\theta^*$ of the measured data with the estimated background fraction. To model the background we use two different Monte Carlo samples, see section 6.2. We consider two main background sources, $W + b\bar{b}$+2 light quark jets to model W + heavy flavor and electroweak processes and W+4 light quark jets to model QCD and mistag background. The background was estimated to be $\mu_{W+b\bar{b}+2q} = 6.2 \pm 1.2$ and $\mu_{W+4q} = 4.1 \pm 0.9$ events, see table 6.4.

Before we can fit the distribution we have to correct it for acceptance and reconstruction effects. Therefore, we multiply bin by bin the signal $N_{signal}(i)$ as well as the background template $N_{bkg}(i)$ with our transfer function τ, shown in figure 7.8

$$N_{final}(i) = N_{data}(i) \cdot \tau(i) \quad (7.8)$$

$$N^{bkg}_{final}(i) = N_{bkg}(i) \cdot \tau(i) \quad (7.9)$$

On the left hand side of figure 7.9 the reconstructed helicity distribution of the data in combination with the background distribution is shown for each detector component separately. The right-hand side shows these distributions after multiplying with the transfer function τ.

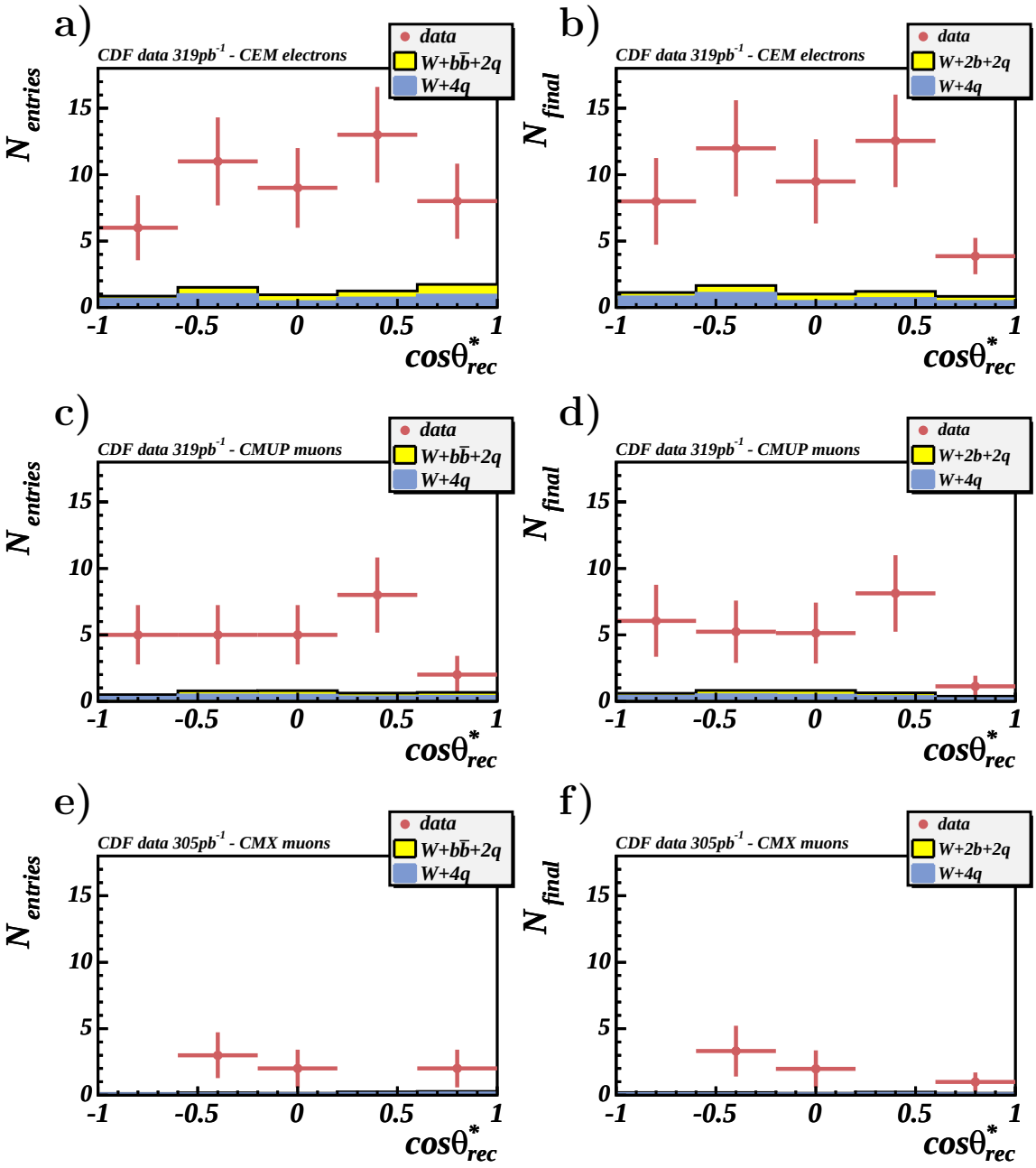

Figure 7.9: Left hand side : Helicity distribution of data (red crosses) after reconstruction. Additionally, the background templates for $W + b\bar{b} + 2q$ and $W + 4q$ are shown. Right hand side : Same distributions after multiplying with the transfer function. a,b) CEM electrons, c,d) CMUP muons, e,f) CMX muons.

7.3.2 Extracting the helicity fractions

After transferring to the "partonic" distribution we add up all detector components and fit the theoretically expected functions of the different W boson helicities.
First, we will measure the fractions of the Standard Model expected polarizations. For this measurement only the shape of the $\cos\theta^*$ distribution is relevant. The absolute normalization is therefore adjusted to the observed number of events and does not enter as a parameter in the fit. The value of the right-handed rate F_+ is predicted to be zero in the Standard Model. The sum of the fractions of longitudinally and left-handed polarized W bosons has to be 1. Therefore, we can fit one parameter. We fit the fraction of longitudinally polarized W bosons (F_0) and calculate afterwards the fraction of the left-handed polarized ones ($F_- = 1 - F_0$). The fit function f_{fit} is given by:

$$f_{fit} = F_0 \cdot f_0 + (1 - F_0) \cdot f_- \tag{7.10}$$

where (compare with equations 7.1, 7.2)

$$f_0(\cos\theta^*) = \frac{3}{4}(1 - \cos^2\theta^*) \tag{7.11}$$

$$f_-(\cos\theta^*) = \frac{3}{8}(1 - \cos\theta^*)^2 \tag{7.12}$$

As we use only the shape, we have to make sure, that the integral of our fit function is 1:

$$I_{fit} = \int_{-1}^{1} F_0 \cdot \frac{3}{4}(1 - x^2) + (1 - F_0) \cdot \frac{3}{8}(1 - x)^2 dx = 1 \tag{7.13}$$

To extract the parameter F_0 we use the binned likelihood method. A χ^2-fit is disfavored because of the small bin content in each bin.

Likelihood functions [65] are based on a known or estimated probability density function $f(\mathbf{x}|\mathbf{a})$ where $\mathbf{x}$ is an observable and $\mathbf{a}$ is a set of unknown parameters to be estimated. For a set of measured observables $x_1, x_2, ...x_n$ the likelihood function $L_\mathbf{a}$ is defined by

$$L(\mathbf{a}) = f(x_1|\mathbf{a}) \cdot f(x_2|\mathbf{a}) \cdots f(x_n|\mathbf{a}) = \prod_{i=1}^{n} f(x_i|\mathbf{a}) \tag{7.14}$$

The best estimator $\hat{\mathbf{a}}$ for the parameter set $\mathbf{a}$ is the one that maximizes $L(\mathbf{a})$ with respect to the given data set x_i. Since we use a binned likelihood function for our measurement the contents of a set of bins n_i are used as observables. The statistical content of a bin n_i is described by the Poisson distribution

$$P(n_i) = \frac{\mu_i^{n_i} e^{-\mu_i}}{n_i!} \tag{7.15}$$

where μ_i denotes the theoretically expected mean value for the $t\bar{t}$ signal $\mu_i^{t\bar{t}}$ plus the number of estimated background events μ_i^{bkg} in this bin i.

$$\mu_i = \mu_i^{t\bar{t}} + \mu_i^{bkg} \tag{7.16}$$

Taking the number of events N_{final} in our final plot into account we can calculate the theoretically expected mean value for each bin i of the $t\bar{t}$ signal by:

$$\begin{aligned} \mu_i^{t\bar{t}} &= \mu^{t\bar{t}} \cdot \int_{a_i}^{a_{i+1}} f_{fit}(\cos\theta^*, F_0)\, d\cos\theta^* \\ \text{with } \mu^{t\bar{t}} &= N_{final} - \mu^{bkg} \\ \text{This yields:} \quad & \int_{-1}^{1} f_{fit}(\cos\theta^*, F_0)\, d\cos\theta^* = 1 \end{aligned}$$

In order to get the single free parameter F_0 the negative log likelihood function has to be minimized. The negative log-likelihood function is then defined as:

$$l(F_0) = -\sum_{i=1}^{Nbins} \ln\left(\frac{\mu_i^{n_i} e^{-\mu_i}}{n_i!}\right) \tag{7.17}$$

To measure the fraction of longitudinally polarized W bosons we sum up the $\cos\theta^*$ distribution of all three detector components and minimize the negative log likelihood function. We use the program MINUIT [66] to minimize the negative log likelihood function. The fit parameter F_0 is constraint in the fit to the physical region $[0, 1]$. Figure 7.10 shows the summed histogram with the resulting distribution of the fit (black line) and as comparison the Standard Model expectation (dashed line). On the right hand side the negative log likelihood function within the physical region is shown. We get a fraction for the longitudinally polarized W bosons of $F_0 = 81.3\,^{+11.4}_{-12.4}\,\%$ (stat.), which is comparable with the Standard Model prediction within the errors.

Since the normalized likelihood function can be interpreted as a probability density function upper or lower boundaries can be calculated. These limits are, calculated for a given confidence level (C.L.), defined as :

$$c_{C.L.}^{upper} = \frac{\int_{-\infty}^{F_{0,up}} L(F_0) d\cos\theta^*}{\int_{-\infty}^{\infty} L(F_0) d\cos\theta^*} \quad \text{or} \quad c_{C.L.}^{lower} = \frac{\int_{F_{0,low}}^{\infty} L(F_0) d\cos\theta^*}{\int_{-\infty}^{\infty} L(F_0) d\cos\theta^*} \tag{7.18}$$

Since a Bayesian approach is persued in this analysis the integration is only done in the physical region $0 \leq F_0 \leq 1$. In the language of Bayesian statistics this means to apply a prior distribution which is 1 in the interval $[0; 1]$ and

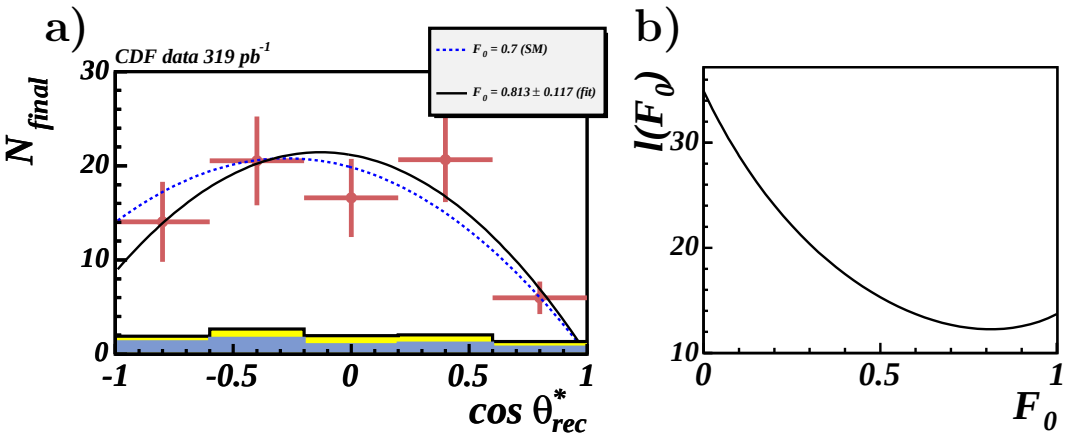

Figure 7.10: a) Measured data with the estimated background after correction of acceptance and reconstruction effects. All three detector components are summed up. The fit is performed with one free parameter, the longitudinal fraction of the W boson helicity F_0. The right-handed ratio is set to zero, as expected in the Standard Model. b) Negative log likelihood function within the physical region.

0 elsewhere. In case of F_0 we calculate the lower limit by shifting the lower boundary until the required confidence interval is reached.

$$c_{C.L.}^{lower} = \frac{\int_{F_{0,low}}^{1} L(F_0) d\cos\theta^*}{\int_{0}^{1} L(F_0) d\cos\theta^*} \tag{7.19}$$

For this analysis we use a confidence level of 95%. The lower limit of the fraction of longitudinally polarized W bosons is then 59.9%. The result is shown in figure 7.11.

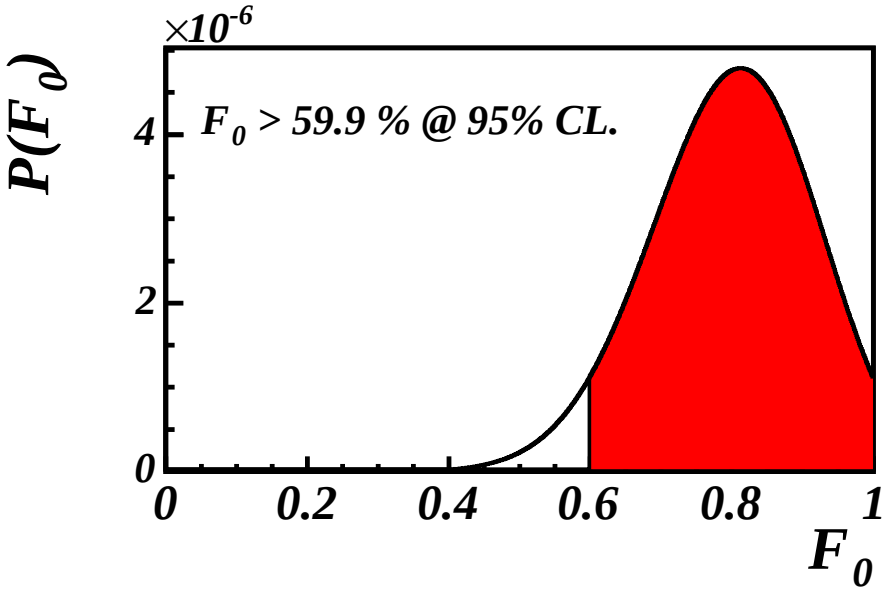

Figure 7.11: Posterior probability density function of F_0. The lower limit is calculated by shifting the lower boundary until the required confidence interval of 95% is reached.

To test the V-A structure of the electroweak force we now include also right-handed W boson component in our fit. In order to have still one free parameter we fix the fraction of longitudinally polarized W bosons to the value given by the Standard Model $F_0 = 0.7$. This is sensible because a modified coupling would lead to a production of right-handed W bosons, but would leave the longitudinal component unaltered [64]. The complete fit function is then given by :

$$f_{fit}(\cos\theta^*, F_+) = N_{final} \cdot \frac{2}{5}\left(0.7 \cdot \frac{3}{4}(1-\cos^2\theta^*) + (0.3 - F_+) \cdot \frac{3}{8}(1-\cos\theta^*)^2 + F_+ \cdot \frac{3}{8}(1+\cos\theta^*)^2\right)$$

where F_+ denotes the fraction of right-handed W bosons. The fraction of left-handed W boson is then given by $F_- = 0.3 - F_+$.

The result of the fit gives a fraction of right-handed W bosons of $F_+ = 4.0\,^{+7.2}_{-4.0}\,\%$ (stat.), which is in good agreement with the Standard Model expectation of 0.

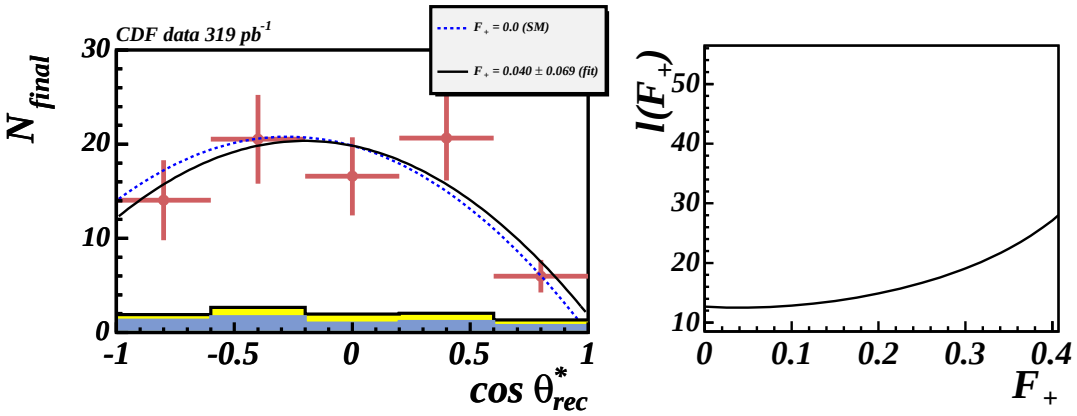

Figure 7.12: a) Measured data with the estimated background after correction of acceptance and reconstruction effects. All three detector components are summed up. The fit is performed with one free parameter, the right-handed fraction of the W boson helicity F_+. The fraction of longitudinally polarized W bosons is fixed to 0.7, as expected in the Standard Model. b) Negative log likelihood function within the physical region.

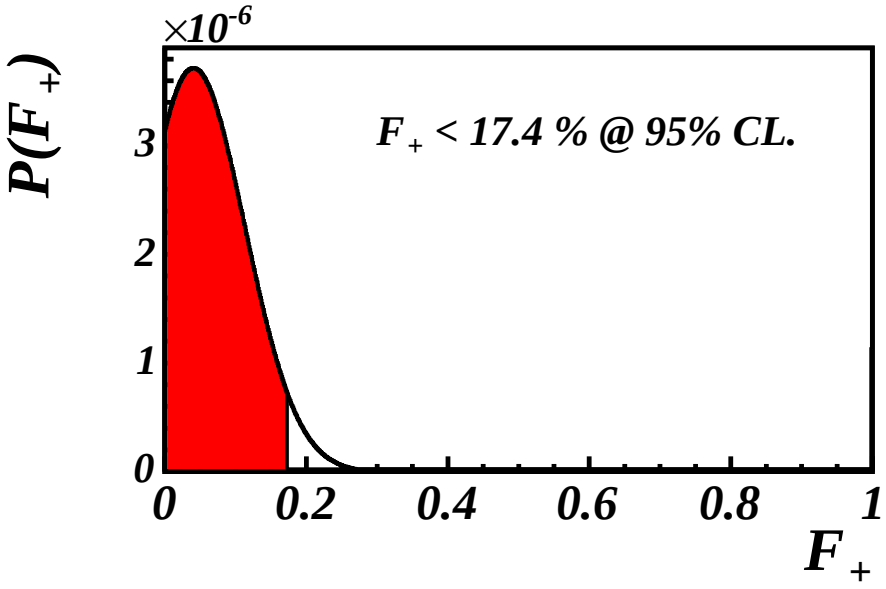

Figure 7.13: Posterior probability density function of F_+. The upper limit is calculated by shifting the upper boundary until the required confidence interval of 95% is reached.

7.3.3 Proof of Principle

In order to check the consistency of our method to extract the different helicity fractions we use the well known technique of pseudo or Monte Carlo experiments. We also use pseudo experiments to determine the systematic uncertainties. The procedure how to generate randomly CDF pseudo experiments is described in the following:
For one single pseudo experiment we throw the same number of events as we have measured (79) in data. The background is modeled using two different templates. The number of events for each template are taken to be Poisson distributed with a mean of 6.2 and 4.1, respectively. For each experiment the difference between 79 and the number of background events is taken as the number of signal events. Afterwards we create the helicity distribution by drawing the number of signal events from the $t\bar{t}$ Monte Carlo template and the number of background events from the corresponding background template. This is done for each detector component separately. These distributions are then treated like the real experiment. We multiply the signal as well as the background distribution with the transfer function and sum up all three resulting distributions. Then the fraction of longitudinally polarized W bosons as well as the fraction of possible right-handed polarized W boson is fitted in the same way as for the real data. The obtained values F_0 or F_+ are filled into a new histogram, respectively. The results for 10000 pseudo experiments are given in figure 7.14. In case of the fit of F_0 there are some experiments where the minimization fails. These experiments are accumulated in the last bin of figure 7.14a). In these experiments the fitter runs into the physical boundary at $F_0 = 1$. Therefore, we exclude the last bin in a Gaussian fit on this distribution. The results match very well with the input ($F_0 = 0.7$ and $F_+ = 0$).

In figure 7.14 we have checked our procedure with the Standard Model composition ($F_0 = 0.7$, $F_- = 0.3$, $F_+ = 0$). The result does not necessarily hold for all compositions. Therefore, it is necessary to scan the entire range of the parameter space. For this purpose we reweight the helicity distribution after complete reconstruction and selection by the weight function $w(\cos\theta^*)$. The weight is then given by:

$$w(F_0') = \frac{F_0' \cdot f_0(\cos\theta^*) + (1 - F_0') \cdot f_-(\cos\theta^*)}{0.7 \cdot f_0(\cos\theta^*) + 0.3 \cdot f_-(\cos\theta^*)}$$

where the distribution for longitudinally and left-handed polarized W bosons are f_0 and f_-, respectively, see equations 7.11, 7.12. We run 10000 pseudo experiments from $F_0' = 0$ to $F_0' = 1$ in steps of 0.1. The result can be seen in figure 7.15.

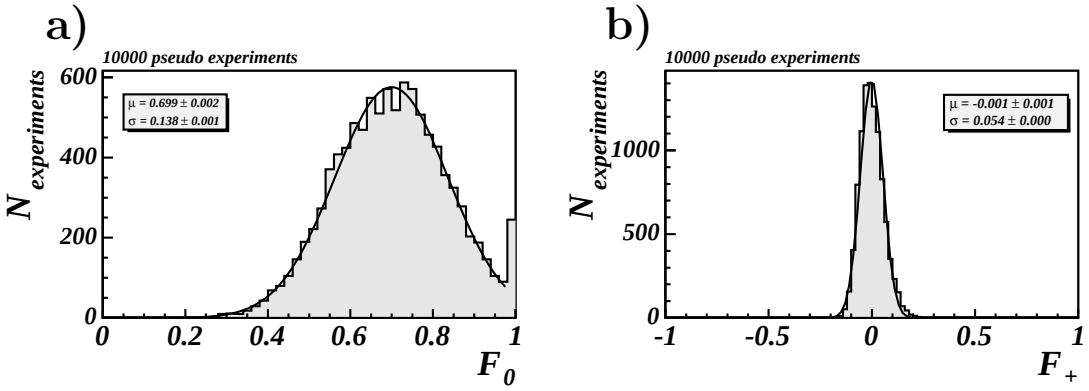

Figure 7.14: 10000 CDF pseudo experiments with the same number of events as in the real experiment which corresponds to 319 pb^{-1}. a) Fraction of longitudinally polarized W bosons CDF pseudo experiments with F_+ fixed to zero. b) Fraction of right-handed polarized W bosons with F_0 fixed to the Standard Model prediction of 0.7

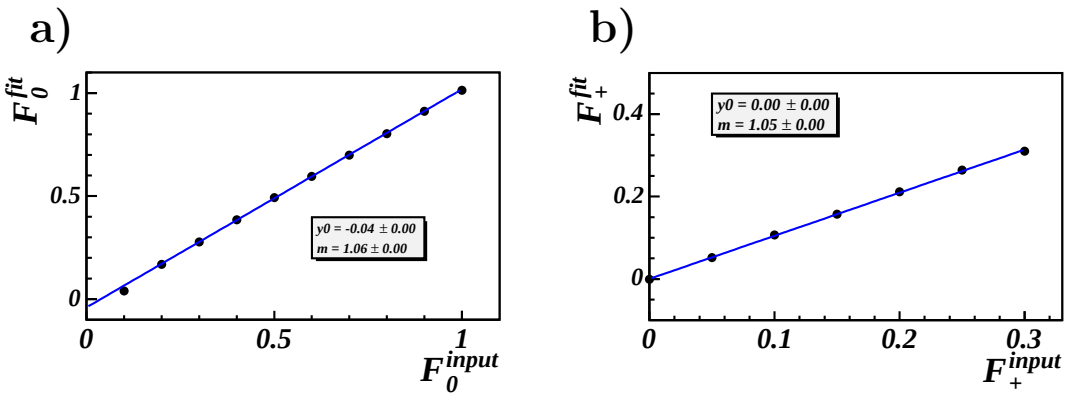

Figure 7.15: Extracted W boson helicity fraction F_0^{fit} a) and F_+^{fit} b) obtained by 10000 pseudo experiments using the same statistics of the data as in the real experiment versus the W helicity fractions F_0^{input} a) and F_+^{input} b) chosen to be present in the test Monte Carlo sample.

7.4 Uncertainties of the measurement

The uncertainties of our measurement are composed of two types. On the one hand we have to give the statistical error, which is determined through the technique of the fit. A detailed explanation can be found elsewhere [65]. On the other hand systematic uncertainties caused by theoretical parameters, experimental set up or the analysis method have to be considered.
In the following section we will determine the systematic uncertainties of our measurement with pseudo experiments. The procedure has been explained in detail in the last section. Except for the background estimation we will modify in this procedure the distribution which is used to model the $t\bar{t}$ signal. In each experiment we throw the same number of events as we have measured in data. The following uncertainties are investigated:

- Monte Carlo generator
- Top quark mass
- Parton density functions
- Initial and final state radiation
- Jet energy scale
- Background estimation
  - Background rate
  - Background modeling

We perform 10000 pseudo experiments for each modified set up. The systematic uncertainty is then given by the difference of the Gaussian means between the modified and unmodified distributions.

7.4.1 Monte Carlo Modeling

The analysis as a whole and especially the transfer function have been developed using a PYTHIA $t\bar{t}$ Monte Carlo sample (black line in figure 7.16). To investigate the effect of the Monte Carlo generator, we create 10000 pseudo experiments with a HERWIG $t\bar{t}$ Monte Carlo sample (red dashed line). The uncertainty is then given by the difference between the means of the two Gaussian fits on each set up, see figure 7.16. We get a systematic error for F_0 of $\Delta F_0 = 0.025$ and for F_+ of $\Delta F_+ = 0.011$.

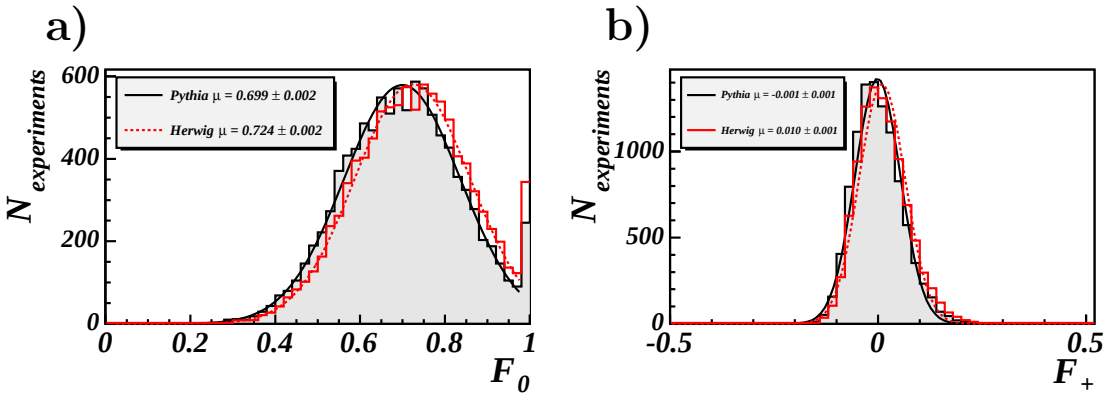

Figure 7.16: 10000 CDF pseudo experiments where the signal sample has been generated with PYTHIA(black line) or with HERWIG (red dashed line). Free fit parameter : a) F_0, b) F_+.

MC generator	F_0	ΔF_0	$\Delta F_0/F_0$	F_+	ΔF_+
PYTHIA	0.699			-0.001	
HERWIG	0.724	0.025	3.6 %	0.010	0.011

Table 7.1: Summary of fit result of a Gaussian on each distribution created with 10000 pseudo experiments.

7.4.2 Top Quark Mass

The systematic uncertainty caused due the choice of the top quark mass, which was set in the Monte Carlo, is determined by using Monte Carlo samples with different top quark masses. Remember that there is a theoretical dependence of the fraction of longitudinally polarized W bosons, see equation 1.9. Therefore, we expect small differences between the samples of different top quark masses. Since we do not have different mass samples generated with PYTHIA we use for all three different top quark masses HERWIG samples. The sample with $m_{top} = 178$ GeV/c^2 represents the reference sample. The result of 10000 pseudo experiments with top quark masses of 172.5 GeV/c^2, 175 GeV/c^2 and 178 GeV/c^2 is shown in figure 7.17. A summary of the result of the Gaussian fit on the corresponding distribution is given in table 7.2. As both samples give a difference in the negative direction we take the bigger one as the error. The resulting error for F_0 is then $\Delta F_0 = -0.033$ and for F_+ we obtain $\Delta F_+ = -0.013$.

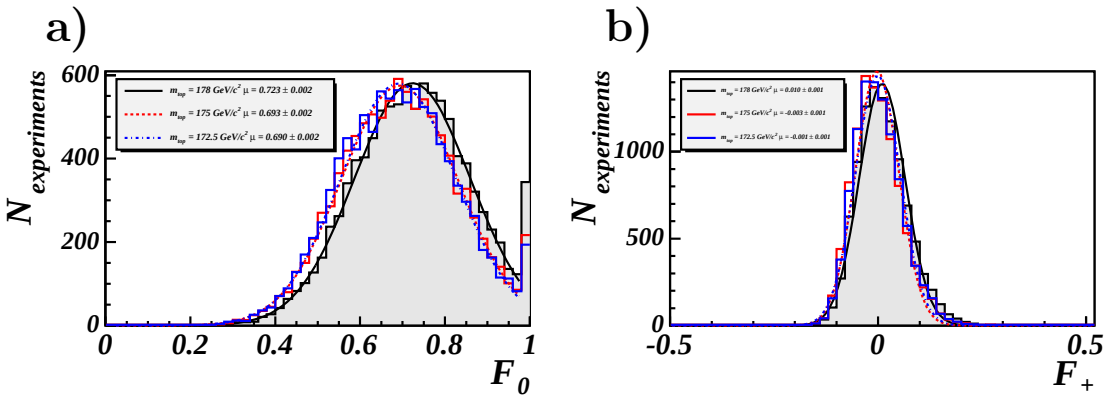

Figure 7.17: 10000 CDF pseudo experiments with $m_{top} = 172.5$ GeV/c^2 (blue dotted line), $m_{top} = 175$ GeVc^2 (red dashed line), $m_{top} = 178$ GeV/c^2 (black line). Free fit parameter a) F_0, b) F_+.

top quark mass	F_0	ΔF_0	$\Delta F_0/F_0$	F_+	ΔF_+
$m_{top} = 178$ GeV/c^2	0.723			0.010	
$m_{top} = 175$ GeV/c^2	0.693	-0.030	4.1 %	-0.003	-0.013
$m_{top} = 172.5$ GeV/c^2	0.690	-0.033	4.6 %	-0.001	- 0.011

Table 7.2: Systematic of top quark mass. Summary of fit result of a Gaussian on each distribution created with 10000 pseudo experiments.

7.4.3 Parton density function

The choice of the parton density function (PDF) can have an influence on the kinematics of the produced process. To study this effect we run 10000 pseudo experiments with Monte Carlo samples which have used the MRST72 or MRST75 PDF, respectively. The PDF of our standard PYTHIA $t\bar{t}$ sample is the CTEQ5L parameterization. The distributions of the different samples are given in figure 7.18. A summary of the result of the Gaussian fit on the corresponding distribution is given in table 7.3. We get a very small systematic uncertainty of $\Delta F_0 = 0.002$ and $\Delta F_+ = 0.003$.

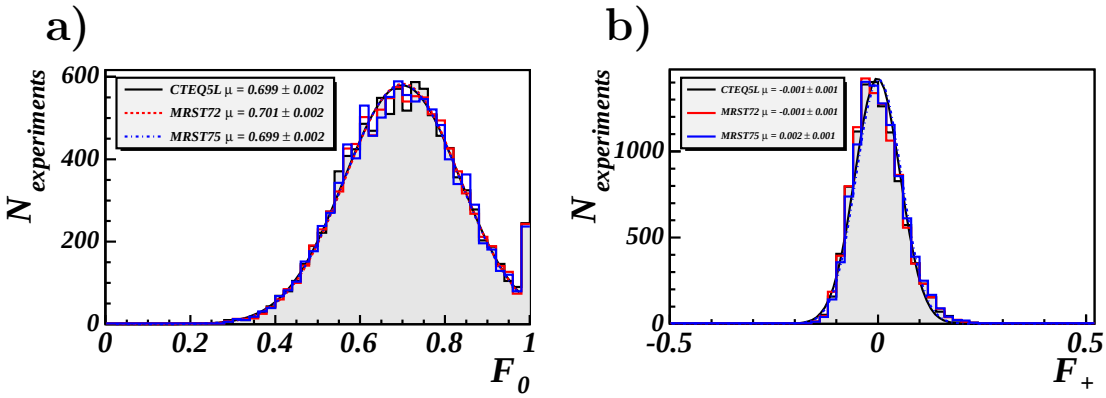

Figure 7.18: 10000 CDF pseudo experiments with CETQ5L (black line), MRST72 (red dashed line) and MRST75 (blue dotted line) parton density function. Free fit parameter a) F_0, b) F_+.

PDF	F_0	ΔF_0	$\Delta F_0/F_0$	F_+	ΔF_+
CTEQ5L	0.699			-0.001	
MRST72	0.701	0.002	0.3 %	-0.001	0.000
MRST75	0.699	0.000	0.0 %	0.002	0.003

Table 7.3: Systematic of parton density functions: Summary of fit result of a Gaussian on each distribution created with 10000 pseudo experiments.

7.4.4 Initial and final state radiation

Initial and final state radiation is also be modeled by the Monte Carlo generator. The choice of the parameter steering the radiation can have an influence on the kinematics of the physics process. To study this effect we run 10000 pseudo experiments with Monte Carlo samples which have more or less initial or final state radiation. The distributions of the different samples are given in figure 7.19. A summary of the result of the Gaussian fit on the corresponding distribution is given in table 7.4. Since all four samples give a difference in positive direction we take for each class the bigger one as the error. To give only one error we add the results both effects in quadrature. The resulting error for F_0 is then $\Delta F_0 = 0.014$ and for F_+ $\Delta F_+ = 0.011$.

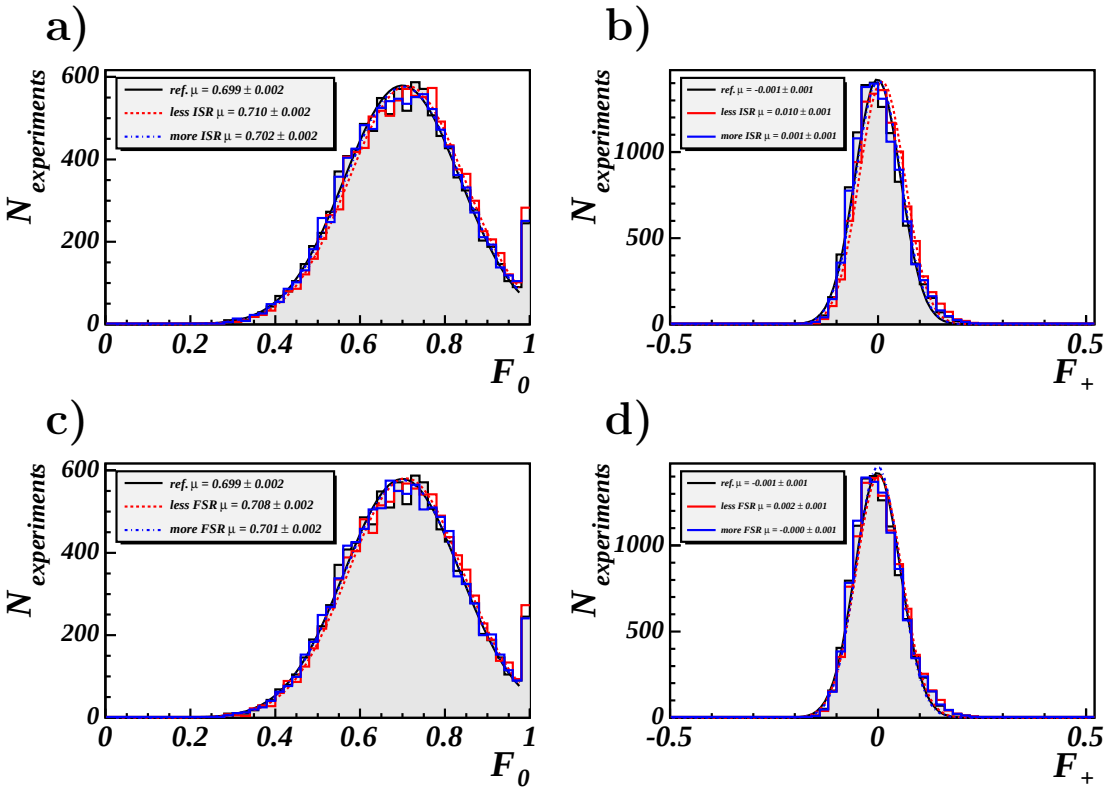

Figure 7.19: 10000 CDF pseudo experiments with standard ISR/FSR (black line), more ISR/FSR (blue dotted line) and less ISR/FSR (red dashed line). Free fit parameter a),c) F_0, b),d) F_+.

	F_0	ΔF_0	$\Delta F_0/F_0$	F_+	ΔF_+
standard	0.699			-0.001	
less ISR	0.710	0.011	1.6 %	0.010	0.011
more ISR	0.702	0.003	0.4 %	0.001	0.002
less FSR	0.708	0.009	1.3 %	0.002	0.003
more FSR	0.701	0.002	0.3 %	0.000	0.001
sum		0.014	2.0 %		0.011

Table 7.4: Systematic of initial and final state radiation. Summary of fit result of a Gaussian on each distribution created with 10000 pseudo experiments. The results of both effects are added in quadrature.

7.4.5 Jet Energy Scale

The uncertainty on the jet energy scale is determined by varying [1] the jet energy scale by one standard deviation [63]. After shifting the jet energies by one sigma in both negative and positive direction, we run for each set up 10000 pseudo experiments. The distributions of the different samples are given in figure 7.20. A summary of the result of the Gaussian fit on the corresponding distribution is given in table 7.5. The resulting error for F_0 is then $\Delta F_0 = ^{+0.029}_{-0.013}$ and for F_+ $\Delta F_+ = ^{+0.016}_{-0.006}$.

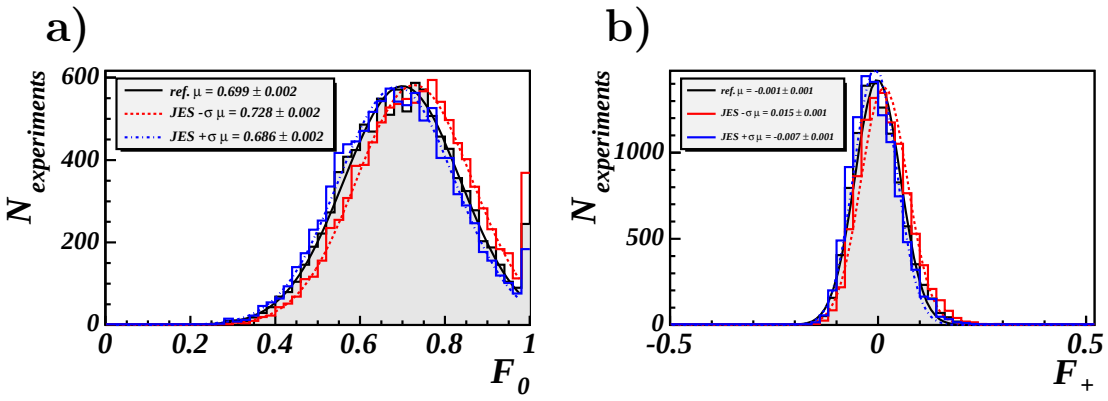

Figure 7.20: 10000 CDF pseudo experiments with no shift (black line), $-\sigma$ (red dashed line) and $+\sigma$ (blue dotted line) shift of the jet energy scale. Free fit parameter a) F_0, b) F_+.

shift	F_0	ΔF_0	$\Delta F_0/F_0$	F_+	ΔF_+
no shift	0.699			-0.001	
$-\sigma$	0.728	0.029	4.1 %	0.015	0.016
$+\sigma$	0.686	-0.013	-1.9 %	-0.007	-0.006

Table 7.5: Systematic of the jet energy scale. Summary of fit result of a Gaussian on each distribution created with 10000 pseudo experiments.

[1] We use the corresponding member function `setTotalSysUncertainties(±1)` of the jet energy correction class

7.4.6 Background Estimation

Uncertainties of the background estimation can arise from two different sources. There are uncertainties of the background rate and of the shape of the background modeling. To deal with the uncertainty of background rate we add and subtract respectively one sigma of the estimated rate ($\mu_{W+b\bar{b}+2q} = 6.2 \pm 1.2$ and $\mu_{W+4q} = 4.1 \pm 0.9$).
For the analysis we use two different background samples, one for QCD and mistag background ($W + 4q$) and one for heavy flavor production and electroweak processes ($W + 2b\bar{b} + 2q$). To check the modeling we make two sets of pseudo experiments, where all background events are drawn from only one template. We run for each set up 10000 pseudo experiments. The distributions of the different samples are given in figure 7.21. A summary of the result of the Gaussian fit on the corresponding distribution is given in table 7.6. We add the results of both effects in quadrature to give one error for the background estimation. The resulting error for F_0 is then $\Delta F_0 = ^{+0.023}_{-0.009}$ and for F_+ $\Delta F_+ = ^{+0.013}_{-0.003}$.

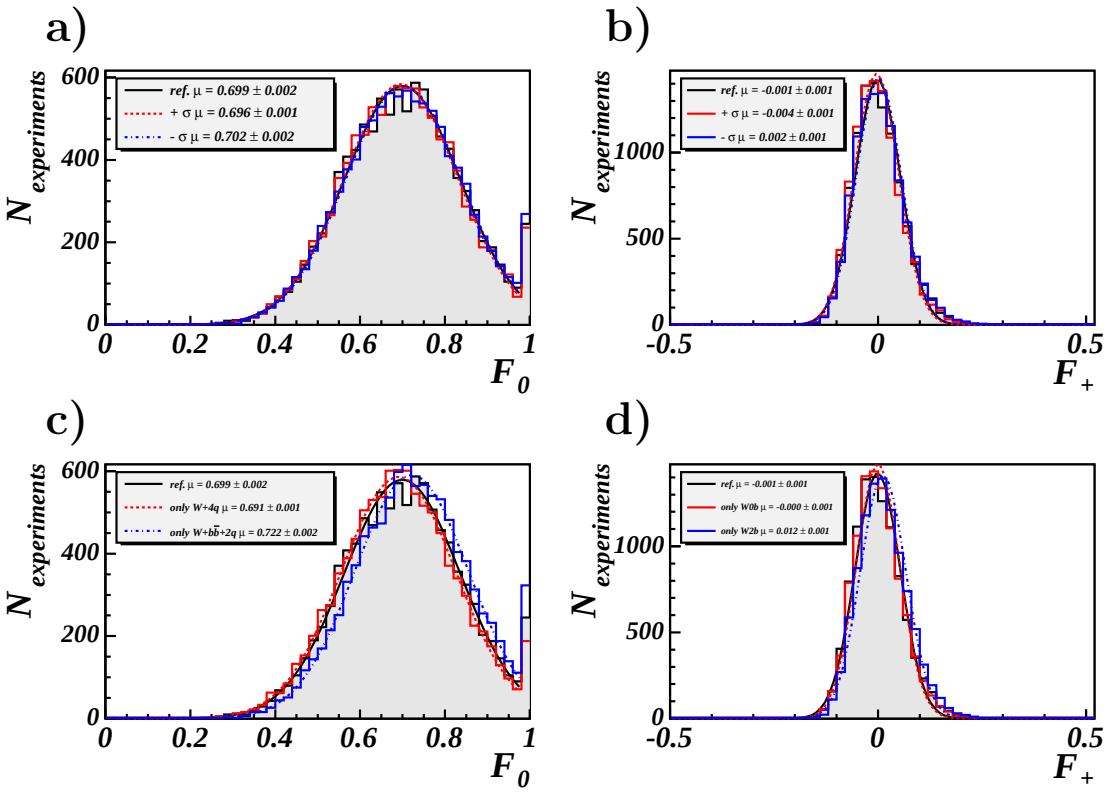

Figure 7.21: 10000 CDF pseudo experiments with standard background (black line), $+\sigma$ (blue dotted line) and -σ (red dashed line) of the estimation of the rate or modeled with only $W + b\bar{b} + 2q$ (blue dotted line) and $W + 4q$ (red dashed line), respectively. Free fit parameter a),c) F_0, b),d) F_+.

Shift	F_0	ΔF_0	$\Delta F_0/F_0$	F_+	ΔF_+
no	0.699			-0.001	
rate $-\sigma$	0.702	0.003	0.4 %	0.002	0.003
rate $+\sigma$	0.696	-0.003	-0.4 %	-0.004	-0.003
only W+$b\bar{b}$+2j	0.722	0.023	3.3 %	0.012	0.013
only W+4j	0.691	-0.008	1.1 %	0.000	0.001
sum		-0.009	1.2 %		-0.003
		+0.023	3.3 %		+0.013

Table 7.6: Background systematics: Summary of fit result of a Gaussian to each distribution created with 10000 pseudo experiments. The results of both effects are added in quadrature.

7.4.7 Summary

We have studied different systematic uncertainties. We have checked the main sources like jet energy scale and background estimations as well as smaller contributions like parton density functions or initial and final state radiation. A summary of the different uncertainties is given in table 7.7. We get an overall systematic uncertainty adding all single sources in quadrature of +0.047 and -0.037 for the determination of F_0 and of 0.026 and -0.015 for the determination of F_+.

Source	+ ΔF_0	- ΔF_0	+ ΔF_+	- ΔF_+
Monte Carlo generator	0.025		0.011	
Top quark mass		-0.033		-0.013
Parton density function	0.002		0.003	
Initial and final state radiation	0.014		0.011	
Jet energy scale	0.029	-0.013	0.016	-0.006
Background estimation	0.023	-0.009	0.013	-0.003
Total	0.047	-0.037	0.026	-0.015

Table 7.7: Summary of systematic uncertainties, the total error is calculated by adding all single sources in quadrature.

Putting everything together we get the result for the fraction of longitudinally polarized W bosons as:

$$F_0 = 81.3\,^{+11.4}_{-12.4}\,(\text{stat.})\,^{+4.7}_{-3.7}\,(\text{syst.})\,\%$$

The result for the fraction of the right-handed polarized W bosons if the fraction of longitudinally polarized bosons is fixed is:

$$F_+ = 4.0\,^{+7.2}_{-4.0}\,(\text{stat.})\,^{+2.6}_{-1.5}\,(\text{syst.})\%$$

For the used dataset it can be seen that the systematic error is about one third of the statistical error. Thus, the analysis is dominated by the limited statistics.

Chapter 8

Measurement of the charge asymmetry in $t\bar{t}$ production

This last analysis chapter describes our measurement of the charge asymmetry in $t\bar{t}$ production. In the first section we perform a resolution study using Monte Carlo events. The second section describes the data analysis. The last section deals with the uncertainties of the measurement.

8.1 Reconstruction and Resolution study of the Charge Asymmetry

In this section we will describe how we measure the charge asymmetry in $t\bar{t}$ production and perform a resolution study.

8.1.1 Definition and reconstruction of the Charge Asymmetry

The charge asymmetry is defined as:

$$A = \frac{N_t(\cos\alpha^* \geq 0) - N_{\bar{t}}(\cos\alpha^* \geq 0)}{N_t(\cos\alpha^* \geq 0) + N_{\bar{t}}(\cos\alpha^* \geq 0)} \tag{8.1}$$

The angle α^* is defined as the scattering angle of the top quarks in the $q\bar{q}$ rest frame, reminding $q\bar{q} \rightarrow t\bar{t}$ is the dominant production process at the Tevatron. Since this rest frame cannot be reconstructed we use the difference of rapidities between the top quarks. This value is Lorentz invariant and can therefore be measured in the lab frame. The connection between the scattering angle $\cos\alpha^*$ and the difference of the rapidity Δy is derived in the following equations.

The rapidity y of a particle with the z-component of the momentum p_z^* and the energy E^* in the $q\bar{q}$ rest frame is defined as :

$$y = \tanh^{-1}(\frac{p_z^*}{E^*}) \tag{8.2}$$

Transforming of $\frac{p_z^*}{E^*}$ yields, with the mass m of the particle, the absolute momentum p^* and the center of mass energy $\sqrt{\hat{s}}$ of the $q\bar{q}$ system :

$$\frac{p_z^*}{E^*} = \frac{p_z^*}{\sqrt{p^{*2}+m^2}} = \frac{p_z^*}{p^*} \cdot \frac{1}{\sqrt{1+\frac{m^2}{p^{*2}}}}$$

$$\cos\alpha^* = \frac{p_z^*}{p^*} \quad \text{and} \quad p^{*2} = \frac{\hat{s}}{4} - m^2$$

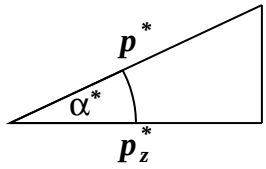

$$\Longrightarrow y = \tanh^{-1}\left(\frac{\cos\alpha^*}{\sqrt{1+\frac{4m^2}{\hat{s}-4m^2}}}\right) \tag{8.3}$$

The difference between both particles with $m = m_{top}$ is then given by :

$$y_2 - y_1 = \Delta y = 2 * \tanh^{-1}\left(\frac{\cos\alpha^*}{\sqrt{1+\frac{4m_{top}^2}{\hat{s}-4m_{top}^2}}}\right) \tag{8.4}$$

Transforming to the scattering angle provides :

$$\cos\alpha^* = \sqrt{1+\frac{4m_{top}^2}{\hat{s}-4m_{top}^2}} \cdot \tanh\left(\frac{\Delta y}{2}\right) \tag{8.5}$$

Equation 8.5, the scattering angle α^* in the $q\bar{q}$ rest frame as a function of the center of mass energy $\sqrt{\hat{s}}$ and the rapidity difference, is drawn in figure 8.1. One can see this function does not flip the sign by transforming $\cos\alpha^*$ into Δy. Since we are interested only in the asymmetry (equation 8.1) we can use the variable Δy. As our used Monte Carlo sample are leading order Monte Carlo it cannot describe this effect. We thus expect to measure no asymmetry in Monte Carlo. To measure this asymmetry we plot the $\Delta y \cdot q_{e,\mu}$ distribution of the reconstructed top quarks,where $q_{e,\mu}$ denotes the charge of the lepton from the leptonically decaying top quark. The multiplication with the charge of the lepton is done to distinguish between top quarks and anti-top quarks. The mass of the top quarks is set to 175 GeV/c^2 for the rapidity calculation. The result for our $t\bar{t}$ Monte Carlo sample is shown in figure 8.2. We see a small asymmetry in the Monte Carlo simulation of ($A = -2.4 \pm 0.6\%$).

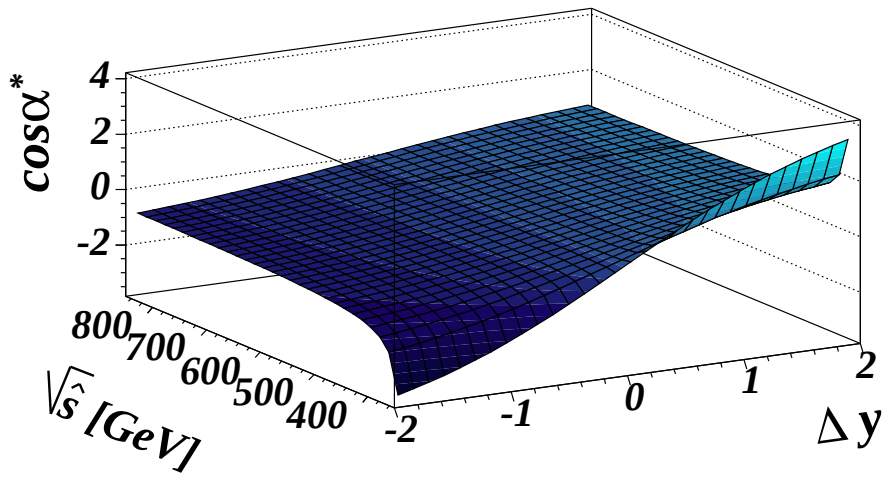

Figure 8.1: The scattering angle α^* in the $q\bar{q}$ rest frame with respect to the center of mass energy and the rapidity difference. Only regions where $|\cos\alpha^*| < 1$ are kinematically allowed regions.

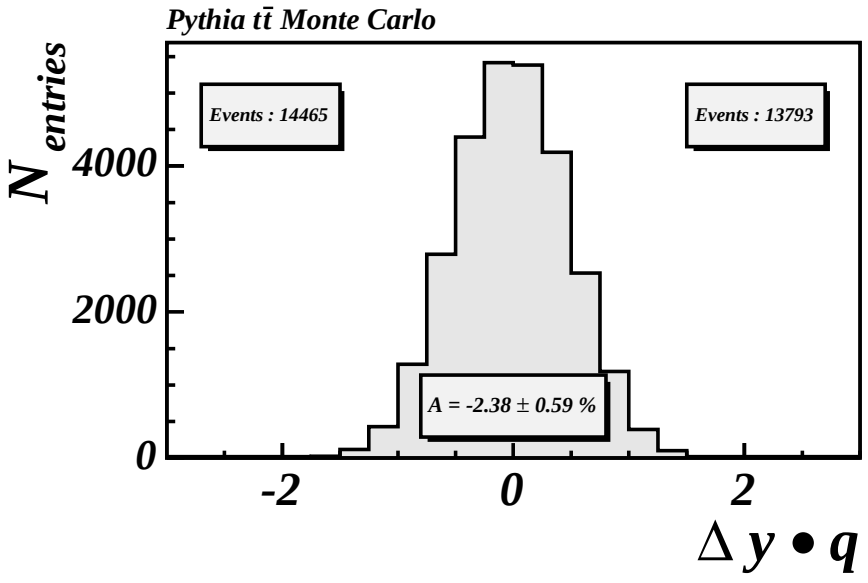

Figure 8.2: $\Delta y \cdot q_{e,\mu}$ of Monte Carlo generated top quarks. The asymmetry is calculated by dividing the difference by the sum of the event numbers.

8.1.2 Determination of the resolution of $\Delta y \cdot q$

To determine the resolution of $\Delta y \cdot q$ we plot the value after the reconstruction and selection versus the true value, see figure 8.3a. We fit each slice of the true values with a Gaussian fit and enter the width σ into a new histogram, see figure 8.3b. For the central values, the only critical region is around $\Delta y \cdot q = 0$, because we are only interested in the sum of events with $\Delta y \cdot q < 0$ or $\Delta y \cdot q > 0$, respectively. The resolution around $\Delta y \cdot q = 0$ is 0.3, therefore we use a bin width of 0.3 for the data measurement. To see if the reconstruction can bias the

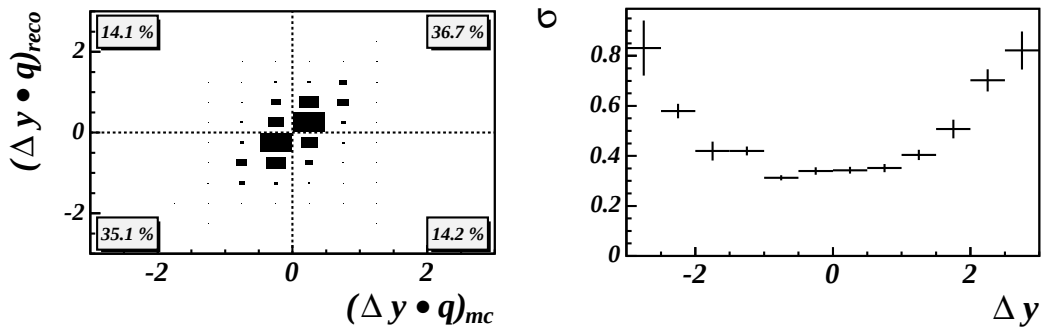

Figure 8.3: Reconstructed vs. Monte Carlo of $\Delta y \cdot q$. The numbers in the boxes are the fraction of events in the corresponding quadrant including overflow and underflow.

measurement of $\Delta y * q$ by changing the sign more often into one direction as backwards we do some migration study. We plot the Monte Carlo generated value against the value of the best possible event interpretation and count the events in all quadrants separately, see figure 8.3a. The contribution of flipped events is about 23 % which can seen in the upper left and the lower right quadrant. But the difference between the two numbers is smaller than 0.5%. Therefore, we expect no artifically constructed asymmetry after the reconstruction.

8.2 Measurement in Data

The measurement is done using $\Delta y \cdot q$, defined in the section before. The reconstruction and selection of the event interpretation is done with the same framework as for the helicity analysis. Before we consider the $\Delta y \cdot q$ variable we check the components separately. In figure 8.4 the rapidity distribution for each top quark are shown separately. For the rapidity calculation the top mass is set to 175 GeV/c^2. As last check we count the charge of the lepton, see table 8.1.

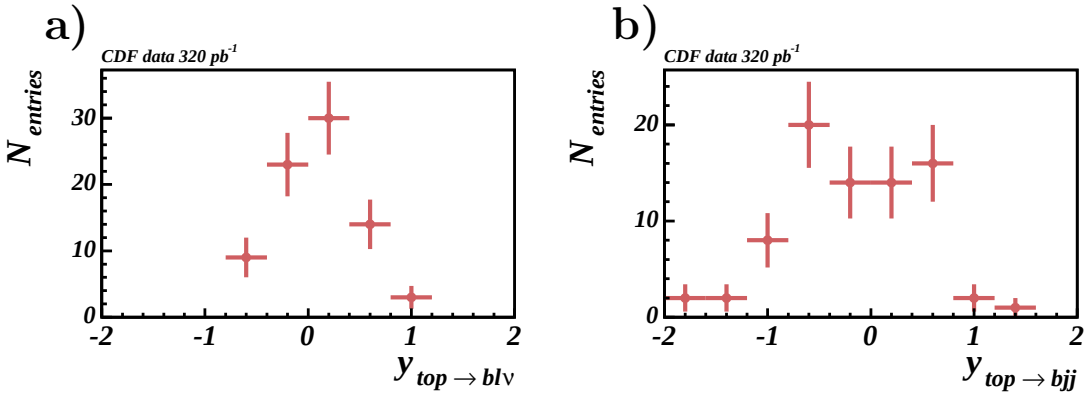

Figure 8.4: Rapidity distribution of leptonically decaying top quark (a) and hadronically decaying top quark (b) after complete reconstruction.

We do not see any difference between positive and negative leptons within the

lepton	positive	negative
CEM	26	21
CMUP	15	10
CMX	7	0
Sum	48	31

Table 8.1: Number of leptons for each detector component and charge.

statistical errors. In figure 8.5a) the data values and the estimated background distribution is shown. We subtract the background from the data as we have done in the helicity analysis before. The result after the subtraction is given in figure 8.5b). For the calculation of the asymmetry we only need the number of events with $\Delta y \cdot q > 0$ and $\Delta y \cdot q < 0$ respectively. The asymmetry then can be calculated with :

$$A = \frac{N(\Delta y \cdot q > 0) - N(\Delta y \cdot q < 0)}{N(\Delta y \cdot q > 0) + N(\Delta y \cdot q < 0)} \tag{8.6}$$

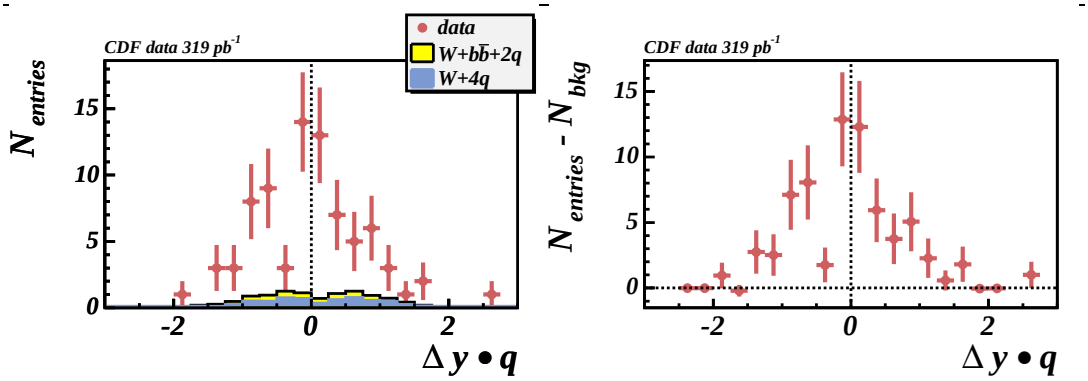

Figure 8.5: $\Delta y * q$ data events summed over all lepton types. a) With estimated background. b) after background subtraction.

After subtracting the background we get :

$$\begin{aligned} N(\Delta y \cdot q < 0) &= 35.8 \\ N(\Delta y \cdot q > 0) &= 32.6 \\ A &= -4.7\% \end{aligned}$$

8.3 Check with pseudo experiments

To check the measurement method we use again the technique of pseudo experiments. The procedure is the same as used in the helicity measurement. For one single pseudo experiment we throw the same number of events as we have measured (79) in data. The background is modeled using two different templates. The number of events for each template are taken to be Poisson distributed with a mean of 6.2 and 4.1, respectively. For each experiment the difference between 79 and the number of background events is taken as the number of signal events. Afterwards we create the $\Delta y \cdot q$ distribution by drawing the number of signal events from the $t\bar{t}$ Monte Carlo template and the number of background events from the corresponding background template. These distributions are then treated like the real experiment. We subtract the background estimation and count the events with $\Delta y \cdot q < 0$ as well as the events with $\Delta y \cdot q > 0$. The difference divided by the sum gives the value of the asymmetry. This value is filled into a new histogram. The result for 100000 pseudo experiments is given in figure 8.6. The result of a Gaussian fit is -1.2 %. We use this value to correct our measured value. The result for the data is then:

$$A_{corr} = -3.5\%$$

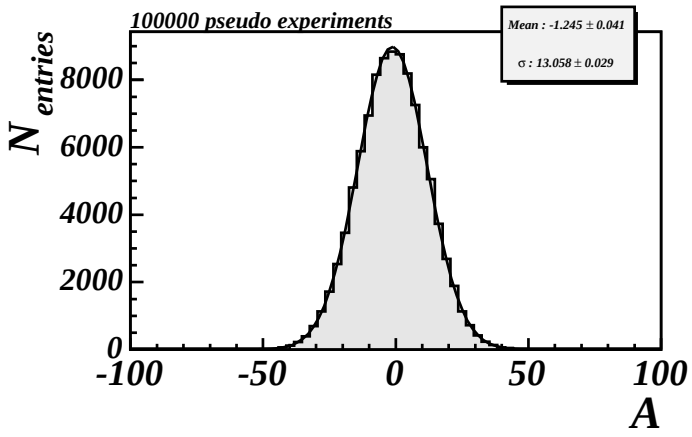

Figure 8.6: 10000 CDF pseudo experiments with the same statistic as in the real experiment with corresponds to $\sim 319\text{pb}^{-1}$.

8.4 Uncertainties of the measurement

As for each physical measurement we have to deal with statistical as well with systematic errors.

8.4.1 Statistical Error

The statistical error of the ratio can be calculated with Gaussian error propagation. To simplify the calculation we change the notation of the different fractions. We set $N_+ = N(\Delta y \cdot q > 0)$ and $N_- = N(\Delta y \cdot q < 0)$. Then we can write the asymmetry by :

$$A = \frac{N_+ - N_-}{N_+ + N_-}$$

and the error with Gaussian error propagation:

$$\sigma_A = \sqrt{\left(\frac{\partial A}{\partial N_+}\sigma N_+\right)^2 + \left(\frac{\partial A}{\partial N_-}\sigma N_-\right)^2}$$

The errors of the different fractions are given by Gaussian error propagation $\sigma N_+ = \sqrt{N_+^{data} + N_+^{bkg}}$ and $\sigma N_- = \sqrt{N_-^{data} + N_-^{bkg}}$. The partial derivatives are given by :

$$\frac{\partial A}{\partial N_+} = \frac{2N_-}{(N_+ + N_-)^2}$$
$$\frac{\partial A}{\partial N_-} = \frac{-2N_+}{(N_+ + N_-)^2}$$

The statistical error is then given by:

$$\begin{aligned}\sigma_A &= \sqrt{\left(\frac{2N_-}{(N_+ + N_-)^2}\sqrt{N_+^{data} + N_+^{bkg}}\right)^2 + \left(\frac{2N_+}{(N_+ + N_-)^2}\sqrt{N_-^{data} + N_-^{bkg}}\right)^2} \\ &= \frac{2}{(N_+ + N_-)^2}\sqrt{N_-^2(N_+^{data} + N_+^{bkg}) + N_+^2(N_-^{data} + N_-^{bkg})}\end{aligned}$$

With the measured values of the data the statistical error of our measurement is :

$$\sigma_A = 12.1\%$$

This statistical error is in good agreement with the result of the pseudo experiments. The width of the Gaussian of figure 8.6, which corresponds to the statistical error, is $\sigma = 13.1\,\%$. We adapt the latter value as final statistical uncertainty of the measurement.

8.4.2 Systematic Errors

Since we use the same sample and the same reconstruction and selection algorithm as for the helicity measurement we consider the same sources of systematic uncertainties. The determination of these errors are done also with pseudo experiments. The procedure is described in section 8.3 in detail. Except for the background estimation we will modify in this procedure the distribution which is used to model the $t\bar{t}$ signal. Uncertainties of the background estimation can arise from two different sources, the estimation of the background rate and of the shape of the background modeling. To deal with the uncertainty of background rate we add and subtract respectively one sigma of the estimated rate ($\mu_{W+b\bar{b}+2q} = 6.2 \pm 1.2$ and $\mu_{W+4q} = 4.1 \pm 0.9$). To deal with the modeling of the shape we make two sets of pseudo experiments, where all background events are drawn from only one template. The systematic uncertainty is then given by the difference between the unmodified and the modified value.
The results are shown in table 8.2. The main sources of the systematic uncertainty are the top quark mass, the jet energy scale and the tuning of the initial and final state radiation. The total systematic uncertainty is then calculated by adding all single sources in quadrature. We get +2.553 % and -2.566 %, which is smaller than the statistical error.

The result of our first measurement of the charge asymmetry in $t\bar{t}$ production is $A = -3.5 \pm 13.1(\text{stat.}) \pm 2.6(\text{syst.})\%$, which is in good agreement with the Standard Model prediction.

Source	A	ΔA
Standard sample	-0.646 %	
Monte Carlo generator		
Herwig	-0.267 %	+0.379 %
Parton density function		
MRST72	-0.390 %	+0.256 %
MRST75	-1.378 %	-0.732 %
Initial and final state radiation		
less ISR	-1.374 %	-0.728 %
more ISR	-2.549 %	-1.903 %
less FSR	-1.351 %	-0.705 %
more FSR	0.667 %	+1.313 %
Jet energy scale		
$-\sigma$	-1.897 %	-1.251 %
$+\sigma$	-1.775 %	-1.129 %
Background estimation		
- rate	-0.716 %	-0.070 %
+ rate	-0.572 %	+0.074 %
only $W + 4q$	-0.242 %	+0.404 %
only $W + b\bar{b} + 2q$	-1.245 %	-0.599 %
Top quark mass		
$m_{top} = 178$ GeV/c^2	-0.267 %	
$m_{top} = 175$ GeV/c^2	0.331 %	+0.598 %
$m_{top} = 172.5$ GeV/c^2	1.834 %	+2.101 %
Total		+2.553 %
		-2.566 %

Table 8.2: Summary of systematic uncertainties, the total error is calculated by adding all single sources in quadrature.

Chapter 9

Summary and Outlook

In this thesis, I have studied top-antitop quark pair production and the decay of top quarks. The used dataset corresponds to an integrated luminosity of 319 ± 19 pb^{-1} of data. The data are taken during Run II, which started in 2001, with the Collider Detector at Fermilab (CDF) in proton-antiproton collisions with a center-of-mass energy of 1.96 TeV and contains 79 top-antitop quark pair candidates.

I have studied the polarization of W bosons in top quark decays and the charge asymmetry in the production of top-antitop quark pairs. A precise measurement of the W boson polarization is important because of the intimate relationship between the longitudinal W boson and the electroweak symmetry breaking mechanism in the Standard Model. Furthermore a direct measurement of the weak-current chirality from the top quark decay is necessary to validate the $V - A$ structure of the weak interaction predicted by the Standard Model. The Standard Model gives a prediction for the fraction of longitudinal W bosons of $F_0 = \frac{\frac{1}{2}(m_t/M_W)^2}{1+\frac{1}{2}(m_t/M_W)^2} = 70.2 \pm 0.012\%$ for a top quark mass of 174.2 GeV/c^2. Right-handed W bosons are suppressed by a factor of 10^{-5} in the Standard Model.
The measurement of the forward-backward charge asymmetry is a test of perturbative QCD at next-to-leading order and improves the understanding of the production mechanism. The theoretical prediction for the Tevatron gives a value of 6.7 ± 0.9 %.

Once produced, the top quark decays into a W boson and a b quark. The W boson decays afterwards either into lepton and neutrino or into a light quark-antiquark pair. To analyse the W boson helicity we select events where the W boson decays leptonically, because the lepton is necessary to calculate the corresponding angle. To calculate the charge asymmetry, complete fourvectors of both top quarks are required. They can only be calculated if the second W

boson decays hadronically. The signature of the events of interest is therefore, an isolated lepton, from the leptonically decaying W boson, two b quark jets, from both top quark decays and two light quark jets, from the hadronically decaying W boson.

In the first part, the complete partonic top-antitop quark process is reconstructed and resolutions of the reconstruction are given. To get the partonic process the lepton, jets and missing transverse energy have to combined to W bosons and top quarks. A typical four jet event leads to 24 different hypotheses for one event. I have introduced a new selection procedure to deal with this ambiguities. The selected solution and the best possible solution are in good agreement considering the complete sample. The resolutions of the reconstructed masses are of the order. The hadronically decaying W boson can be reconstructed with a resolution of ~ 9 GeV/c^2. The mass of the hadronically decaying top quark with ~ 10 GeV/c^2 and the mass of leptonically decaying top quark with ~ 25 GeV/c^2. To get a "clean" sample a estimation of the expected background is given.

To determine the helicity fractions of the W boson the angle between the lepton in the W boson rest frame and the W boson in the top quark rest frame is considered. The extraction is done using a maximum likelihood method. The longitudinally polarized fraction is found to be $F_0 = 81.3\,^{+11.4}_{-12.4}\,(\text{stat.})\,^{+4.7}_{-3.7}(\text{sys.})\%$, which is consistent with the Standard Model prediction of $F_0 = 70.2\% \pm 0.012$. The lower limit of F_0 for this result is $F_0 > 59.9\%$ @ 95% C.L. The result of the test of right-handed polarized W bosons is $F_+ = 4.0\,^{+7.2}_{-4.0}\%$ (stat.) $^{+2.6}_{-1.5}$ (syst.), which is also consistent with the Standard Model where no right-handed W bosons are allowed. The upper limit of F_+ for this result is $F_+ < 17.4\%$ @ 95% C.L. The result for both measurements as well as the limits are at the moment the world best values. The recently published result for Run II of CDF are $F_0 = 0.74^{+0.22}_{-0.34}$ and $F_+ < 0.27$ @ 95%CL [67] and for DØ are $F_+ < 0.25$ @ 95%CL [68].

The charge asymmetry can be calculated using the difference between the top quark rapidities times the charge of the lepton. This variable is Lorentz invariant and can therefore measure approximately the asymmetry in the top antitop quark rest frame. The result is $A = -3.5 \pm 13.1(\text{stat.}) \pm 2.6$ (sys.) %. This is the first measurement of this effect.

As Run II of the Tevatron continues, CDF will collect significantly larger amounts of data. We run different set of pseudo-experiments to give predictions of the statistical error, see table 9.1. The number of $t\bar{t}$ events are extrapolated from the numbers of the current dataset. With 2 fb^{-1} of data ~ 500 candidates will pass the selection criteria. This number can be even higher because of an improved b-jet identifying or taking higher acceptance region for the leptons into account. With 500 $t\bar{t}$ candidates the statistical uncertainty will be ~ 5

$\int \mathcal{L}dt$ (fb^{-1})	Num $t\bar{t}$ candidates	Statistical Uncert.
0.32	79	$\sim 13\%$
1	~ 250	$\sim 7\%$
2	~ 500	$\sim 5\%$

Table 9.1: Expected systematic uncertainty for different integrated luminosities.

% and reaches the same order as the systematic uncertainty. The systematic uncertainty will also benefit from the higher statistics. Further on the analyses itself can be improved. With improving the resolution it will be possible to fit the longitudinal and right-handed fraction simultaneously.

Appendix A

Data samples

A.1 Online Trigger

Data used in this analyse use one trigger path for central electrons, `ELECTRON_CENTRAL_18` and two trigger path for the muons. The `MUON_CMUP18` trigger path utilizes information from both the CMU and the CMP detector systems. Muons found in the CMX detector are in the `MUON_CMX18` trigger path. We give the required triggers for each level.

A.1.1 ELECTRON_CENTRAL_18

- `L1_CEM8_PT8`
  - $\geq$ one deposition of energy in the Central calorimeter with $E_T > 8$ GeV, Hadronic to Electromagnetic energy ratio (HAD/EM)< 0.125
  - one COT track found having $P_T > 8.34$ GeV/c
- `L2_CEM16_PT8`
  - $\geq$ one deposit of energy in the Central calorimeter with $E_T > 16$ GeV, HAD/EM < 0.125.
  - $|\eta| < 1.317$, is placed on the cluster centroid (seed), guaranteeing the cluster be located in the central portion of the calorimeter.
  - Requires a match between tracks found in the COT at Level 1 to the cluster within a window of ϕ, as determined by multiple scattering interactions in the detector
  - Track $P_T > 8.34$ GeV/c
- `L3_ELECTRON_CENTRAL_18`

  - Uses primary interaction location as found by the track matched to the cluster to recalculate the cluster E_T.
  - Cluster $E_T > 18$ GeV
  - Track $P_T > 9.00$ GeV/c
  - Level 3 also adds a cut on the lateral shower profile (Lshr) of the cluster. This quantity describes how well the energy deposit in the calorimeter matches one coming from an ideal electron.

A.1.2 MUON_CMUP18

- `L1_CMUP6_PT4`
  - Muon stub in the CMU detector having $P_T > 6$ GeV/c.
  - Track in the COT with $P_T > 4.09$ GeV/c.
  - Require an additional stub in the CMP detector.
  - Matching is done at Level 1 between the stubs and the COT track, within a window of a few degrees
- `L2_TRK8_L1_CMUP6_PT4`
  - $\geq$ COT track ranging between ϕ of 0 to 180 degrees.
  - COT track $P_T > 8$ GeV/c.
- `L3_MUON_CMUP_18`
  - Match between tracks and the CMU and CMUP stubs, allowing a window in $r - \Delta\phi$ of less than 20 cm for the CMU stub, 10 cm for the CMP stub

A.1.3 MUON_CMX18

- `L1_CMX6_PT8_CSX`
  - Muon stub in the CMX detector having $P_T > 6$ GeV/c.
  - Require hits in the CSX detector.
  - Require a track in the COT passing through at least 4 layers of the COT detector.
  - COT Track $P_T > 8.34$ GeV/c.
- `L2_AUTO_L1_CMX6_PT8_CSX`

  - The Level 2 trigger requirement is an auto accept trigger, meaning that no additional manipulating of data occurs at this level.

- `MUON_CMX18`
  - Tracks matched to the CMX stub in a window of $r - \Delta\phi$ of less than 10 cm.
  - COT track $P_T > 18$ GeV.

A.2 Good Run List

In this section we present all runs which are marked good and used for the analysis.

141544	141572	141576	141577	141597	141598	141618	141619	141621
141660	141984	141989	142106	142107	142108	142109	142110	142111
142168	142170	142177	142202	144574	144575	144576	144578	144624
144628	144673	144674	144694	144696	144713	144714	144883	144884
145005	145006	145032	145033	145034	145035	145036	145044	145045
145532	145608	145651	145654	146850	146851	146920	147165	147804
147805	147806	147830	147832	147834	147835	147836	147837	147843
147865	147866	147869	148152	148153	148154	148157	148291	148293
148375	148648	148649	148674	148774	148775	148824	148825	148846
148852	148856	148857	148858	148908	148916	148950	148951	148953
149052	149053	149055	149056	149058	149059	149264	149354	149355
149386	149387	149481	149492	149493	149663	149677	149678	149680
149681	149682	149685	150010	150063	150066	150067	150070	150079
150080	150086	150087	150088	150108	150109	150110	150112	150113
150117	150118	150139	150140	150141	150145	150149	150287	150288
150289	150291	150340	150395	150415	150416	150418	150419	150420
150421	150422	150427	150428	150432	150433	150435	150443	150444
150799	150801	150802	150803	150805	150819	150820	150821	150823
150853	151434	151435	151436	151449	151476	151477	151483	151509
151513	151514	151515	151555	151556	151557	151628	151641	151683
151688	151810	151811	151841	151842	151843	151844	151845	151868
151869	151870	151871	151872	151873	151902	151903	151906	151907
151911	151917	151918	151919	151920	151922	151971	151974	151978
152170	152266	152267	152270	152271	152274	152459	152464	152504
152507	152510	152514	152516	152517	152518	152520	152554	152555
152556	152559	152579	152598	152599	152600	152601	152602	152615
152616	152669	152674	152675	152680	152743	152745	152746	152747
152752	152772	152773	152809	152810	152811	152949	152953	152954
153061	153068	153074	153075	153076	153087	153091	153266	153268
153271	153325	153327	153343	153344	153345	153372	153373	153374

153389	153411	153412	153416	153447	153460	153557	153618	153620
153660	153661	153662	153693	153694	153697	153718	153738	153739
154021	154028	154029	154030	154118	154122	154126	154175	154176
154180	154208	154449	154451	154452	154453	154518	154653	154654
154675	154681	155113	155114	155115	155116	155121	155129	155130
155141	155145	155146	155148	155150	155299	155301	155304	155312
155313	155318	155320	155324	155343	155344	155345	155346	155347
155364	155365	155368	155392	155393	155394	155409	155677	155678
155711	155712	155714	155742	155743	155744	155746	155747	155763
155764	155767	155768	155770	155793	155794	155795	155796	155818
155820	155821	155895	155918	155919	155920	155923	155996	155997
156006	156007	156081	156082	156083	156084	156087	156088	156089
156098	156100	156103	156112	156116	156117	156118	156369	156372
156401	156452	156457	156458	156460	156464	156484	156487	159603
160092	160151	160152	160153	160157	160175	160230	160301	160302
160303	160312	160314	160346	160359	160403	160405	160406	160407
160408	160410	160412	160414	160437	160440	160441	160533	160534
160541	160591	160592	160594	160596	160599	160601	160659	160663
160796	160802	160823	160886	160887	160890	160891	160987	160988
160989	161011	161013	161029	161031	161044	161170	161171	161324
161327	161330	161379	161408	161409	161411	161414	161415	161441
161552	161555	161633	161634	161638	161678	161713	161714	161718
161722	161754	161756	161757	161758	161760	161761	161762	161763
161778	161779	161780	161781	161783	161784	161786	161787	161788
161789	161790	161791	161792	161795	161817	161818	161820	161821
161823	161825	161826	161827	161829	161830	162130	162174	162175
162178	162238	162241	162252	162300	162301	162307	162310	162312
162396	162399	162423	162453	162454	162462	162479	162480	162481
162498	162519	162520	162521	162631	162663	162664	162685	162686
162820	162825	162836	162837	162838	162839	162855	162856	162857
162937	162982	162986	163009	163011	163012	163025	163026	163035
163064	163113	163130	163136	163148	163385	163390	163394	163430
163431	163462	163463	163464	163474	163508	163510	163511	163512
163513	163515	163519	163526	163527	163960	164107	164109	164110

164128	164200	164235	164252	164257	164259	164261	164274	164303
164304	164305	164306	164307	164308	164352	164354	164386	164451
164509	164510	164511	164512	164517	164555	164625	164819	164820
164822	164916	164952	164958	164963	164989	165062	165063	165064
165087	165120	165121	165122	165199	165200	165201	165204	165207
165267	165269	165271	165297	165313	165314	165356	165357	165364
165365	165388	165412	165435	165436	165439	165470	165523	165836
165839	165869	165871	165873	165902	165906	165941	165944	165949
166007	166008	166037	166038	166063	166073	166227	166251	166325
166328	166367	166369	166371	166373	166374	166403	166406	166407
166472	166479	166482	166525	166529	166567	166614	166615	166653
166654	166655	166656	166657	166661	166662	166714	166715	166717
166770	166771	166772	166774	166776	166779	166783	166805	166927
166935	167023	167025	167053	167058	167059	167061	167138	167139
167186	167259	167261	167266	167290	167297	167299	167325	167445
167506	167541	167551	167563	167565	167588	167623	167629	167631
167634	167635	167715	167717	167824	167849	167856	167865	167866
167954	167955	167956	167977	167996	167997	167998	168000	168001
168087	168089	168092	168559	168561	168563	168568	168599	168600
168601	168603	168605	168640	168766	168767	168770	168774	168775
168820	168822	168823	168889	175066	175078	175079	175090	175092
175095	175096	175143	175146	175147	175148	175150	175155	175195
175196	175283	175288	175289	175292	176651	176655	176695	176696
177214	177217	177301	177304	177313	177314	177315	177316	177337
177339	177340	177342	177345	177363	177364	177366	177370	177371
177384	177411	177412	177414	177415	177416	177417	177418	177478
177480	177485	177486	177487	177488	177490	177491	177624	177625
177628	177633	177793	177797	177798	177799	177800	177927	177932
177937	177938	177941	178015	178063	178064	178065	178066	178067
178068	178070	178071	178072	178073	178074	178076	178077	178080
178119	178120	178145	178146	178151	178154	178155	178156	178164
178165	178255	178256	178258	178260	178261	178262	178280	178295
178297	178298	178301	178303	178304	178305	178307	178310	178339
178389	178390	178391	178397	178400	178402	178405	178409	178432

178433	178434	178435	178437	178438	178440	178448	178450	178513
178536	178537	178539	178540	178546	178547	178602	178677	178683
178684	178735	178738	178741	178743	178744	178757	178758	178759
178761	178785	178816	178852	178853	178854	178855	178862	178881
178882	178886	178887	178888	178889	178921	179018	179019	179021
179037	179039	179040	179042	179043	179054	179055	179056	182843
182873	182874	183055	183057	183058	183077	183078	183079	183094
183097	183124	183125	183126	183129	183130	183139	183142	183165
183207	183209	183491	183492	183530	183553	183557	183561	183617
183619	183631	183633	183695	183696	183702	183752	183759	183760
183761	183783	183785	183861	183863	183864	183865	183913	183960
183961	183963	183965	183971	184012	184015	184059	184060	184062
184064	184067	184068	184069	184071	184072	184073	184078	184079
184081	184370	184377	184380	184414	184419	184424	184444	184445
184450	184453	184456	184459	184463	184464	184492	184495	184519
184729	184730	184731	184732	184733	184738	184762	184763	184765
184778	184779	184780	184782	184800	184801	184802	184832	184835
184868	184957	185009	185017	185018	185037	185040	185072	185075
185082	185172	185176	185201	185220	185223	185248	185249	185250
185259	185260	185262	185277	185280	185281	185331	185332	185349
185351	185374	185375	185376	185377	185379	185381	185383	185384
185386	185516	185517	185518	185521	185542	185545	185594	185595
185634	185637	185640	185643	185644	185721	185727	185728	185777
185782	185847	185848	185849	185962	185968	185971	185973	186039
186041	186048	186049	186084	186087	186088	186090	186091	186092
186145	186302	186306	186308	186316	186321	186573	186575	186586
186591	186598							

Table A.1: Good Run List

A.3 $t\bar{t}$ candidates

run	event	nj	t	$p_{T,lep}$	$\not\!\!E_T$	$p_{T,jet1}$	$p_{T,jet2}$	$p_{T,jet3}$	$p_{T,jet4}$	$\cos\theta^*$	$\Delta y \cdot q$
—CEM electrons—											
177314	2950396	4	1	24.28	77.39	81.15	63.77	40.43	27.34	-0.7915	-0.9394
177345	3135596	4	1	56.98	59.39	100.7	23.63	62.54	49.39	-0.4965	-1.791
178258	782935	4	1	26.15	82.5	43.37	70.26	82.49	24.28	-0.611	-0.7947
160153	1270879	4	1	91.97	80.38	26.12	63.51	107.7	38.55	0.3964	0.2159
153694	1694029	4	2	31.85	28.38	139.7	74.81	47.55	33.74	-0.3622	-0.01143
153738	205803	4	2	31.71	98.3	58.67	119.5	33.61	26.51	-0.4304	0.1666
153738	2083102	4	1	22.14	70.63	121.4	34.48	80.12	69.09	-0.7817	0.891
154175	1630925	4	1	29.94	144.1	25.34	27.58	141.4	40.27	-0.5714	-0.6821
155320	480816	4	1	93.2	43.86	30.58	64.22	43.14	25.26	0.09409	0.1779
155919	2689969	4	1	51.15	58.86	33.74	99.66	58.65	26.2	0.0172	-0.2443
156457	13182	4	1	33.07	76.34	39.82	44.27	72.36	26.31	-0.3343	-0.8202
160230	805211	4	2	64.59	108.9	27.39	30.17	116.7	71.6	0.03436	0.5441
160441	3910866	4	1	110.7	75.91	59.56	101.5	98.9	55.58	0.6553	-0.08221
160594	290458	4	1	91.64	34.61	50.14	63.51	40.84	33.29	0.8679	-0.5016
161013	111162	5	1	75.48	110.4	30.2	130.3	110	24.3	-0.2406	-0.2486
161414	68227	5	1	51.4	74.97	35.32	85.8	108.3	32.04	0.009264	0.005203
161633	1571961	4	1	48.19	43.34	69.06	23.83	111.7	34.68	-0.1205	0.5362
161792	391660	4	1	45.08	70.26	38.76	33.74	54.55	52.67	-0.08571	-0.102
162423	261933	4	1	73.58	22.41	25.05	50.21	38.72	39.69	0.9439	0.08225
178677	4378990	4	1	34.35	77.27	79.61	115	75.01	28.19	-0.5519	0.6695
162986	1538897	5	2	55.82	77.14	54.58	41.48	132.2	41.06	-0.2661	1.018
164110	954852	4	2	28.64	47.92	41.71	58.46	57.52	44.19	-0.6587	-0.04742
163519	1262057	5	1	20.13	73.09	25.82	88.62	56.4	28.77	-0.8419	-0.223
164274	1449940	4	1	59.58	17.48	59.47	26.51	46.34	45.27	0.7431	1.551
178761	1716435	5	1	56.22	72.27	106.6	72.47	75.82	65.85	-0.1355	-0.6948
164819	1242550	4	1	146.1	68.16	29.54	33.61	146.5	60.69	0.3098	-0.005451
165314	236898	4	1	71.39	51.54	36.38	86.02	89.9	32.47	0.457	-1.14
166614	804529	4	2	113.6	46.99	63.82	32.13	114.6	59.49	0.4642	0.1549
166653	1499964	4	2	91.93	56.05	27.34	89.81	81.02	50.52	0.5255	-1.411
166715	357810	4	1	45.71	39.66	32.98	44.31	31.79	34.94	0.3612	0.342
166717	3530653	4	1	38.01	47.25	74.88	25.46	51.87	28.83	0.2832	-1.38
167053	12401969	4	1	93.54	7.785	70.48	58.95	37.88	37.67	0.4406	-1.206
167551	7969376	5	1	57.81	81.32	39.3	33.42	62.3	26.81	-0.2558	-1.114
168563	2395692	4	1	31.25	60.27	41.12	35.61	76.38	69.05	-0.5059	0.6384
183631	31445	4	1	36.59	25.04	31.79	35.91	43.81	34.71	0.2819	0.3257
183209	1059754	4	1	21.32	29.34	65.84	23.44	93.94	25.33	0.7094	0.05459
183752	3562502	4	1	45.87	86.62	42.85	62.75	58.75	44.44	-0.08066	0.04265
184453	19917	4	1	24.51	116.5	37.89	191.5	53.83	39.74	-0.7104	-0.2424
184519	377410	5	1	93.9	49.45	39.11	53.71	72.61	32.1	0.05751	1.44
184782	2170277	4	1	47.71	99.58	55.32	62.06	82.34	24.39	-0.4183	0.6374
184419	291129	4	1	97.22	43.29	56.67	77.76	67.22	35.96	0.2578	-0.47
185075	4388549	4	1	98.99	28.08	55.96	42.6	76.75	72.32	0.8997	-0.2105

run	event	nj	t	$p_{T,lep}$	$\not\!\!E_T$	$p_{T,jet1}$	$p_{T,jet2}$	$p_{T,jet3}$	$p_{T,jet4}$	$\cos\theta^*$	$\Delta y \cdot q$
185349	57399	4	2	88.41	16.35	83.79	81.6	69.2	36.75	0.5331	-0.8996
185332	1622825	4	1	32.02	35.49	88.96	30.37	195.3	36.28	0.7762	2.615
185777	5392044	4	1	35.21	32.78	44.4	48.12	51.18	36.97	0.2928	-0.7013
186145	9795252	4	1	68.46	21.9	37.27	45.87	102.4	36.71	0.5749	-0.5357
—CMUP muons—											
186087	17361	4	2	43.89	51.04	40.96	69.27	47.77	43.01	-0.3947	-0.4183
178855	5504617	4	2	37.5	49.69	121.7	44.56	75.03	59.67	-0.2171	0.7935
145036	245760	4	1	28.18	66.49	29.13	114.3	79.17	26.54	-0.6342	0.1376
152266	3554	4	1	32.28	40.89	24.52	56.37	76.8	27.49	-0.4211	0.4573
153693	799494	4	2	51.45	39.71	118.5	65.98	80.19	46.92	-0.7746	0.8588
155409	1291806	7	1	40.26	72.55	152.8	84.1	133.2	26.81	-0.1472	-0.6415
160437	280173	4	1	40.47	28.29	71.13	81.34	61.34	26.82	0.6241	-1.356
161788	361577	4	2	37.74	63.73	142.6	78.61	113.2	65.38	0.3985	-0.02289
162837	921871	4	1	57.5	37.37	50.27	51.4	56.3	50.93	0.5401	-0.265
163012	2249546	4	1	75.89	25.12	105.3	35.6	68.71	40.87	0.2423	-0.8801
178120	86683	4	1	31.91	11.16	81.71	66.56	63	33.27	-0.6366	1.663
166567	11615607	4	1	39.98	50.15	94.38	41.95	92.92	51.37	0.09265	0.8168
166529	4938	4	1	41.43	41.95	71.21	36.13	36.34	33.81	0.1097	-0.5471
166779	3652540	5	1	29.59	124.1	54.62	166.5	95	25.5	-0.586	0.903
166717	2288892	4	2	85.89	61.33	64.38	44.06	81.86	67.27	0.2433	0.4402
166805	2534588	4	1	53.51	50.94	45.41	147.4	38.02	27.87	0.6793	-0.9229
167551	3626393	5	3	26.92	38.9	23.68	90.42	38.66	33.86	-0.6574	1.105
168889	1456443	4	1	52.72	38.16	51.31	59.12	56.99	43.5	0.5468	-0.7646
183126	45329	5	1	68.72	152.5	44.1	39.5	142.7	28.24	-0.1886	-0.622
185248	8569330	4	2	71.38	21.63	51.5	87.59	54.03	42.61	0.2575	-0.785
185377	5133539	5	2	62.41	41.63	92.04	61.53	44.61	40.86	0.3816	0.123
185379	300012	5	1	29.37	19.33	99.91	35.84	105.5	24.66	-0.5918	-0.6807
185332	4430084	4	1	85.05	56.04	54.33	115.3	74.71	29.84	-0.1101	0.1289
185518	330101	4	1	146.1	21.65	29.68	56.92	98.44	55.56	0.4751	0.1586
185848	7195410	5	1	35.72	51.77	109.5	28.74	34.37	34.91	-0.9726	0.2723
—CMX muons—											
186145	4971965	5	1	103	34.88	31.1	34.95	37.3	37.38	0.98	0.9625
184832	12978334	4	1	33.91	56.83	49.52	44.78	54.41	54.43	-0.4432	0.3319
178785	1428968	4	1	57.12	64.28	45.25	83.63	50.09	41.96	-0.09399	0.1688
154654	6534372	4	1	39.27	40.05	131.6	63.23	70.35	26.56	-0.275	-0.1074
162837	1447297	5	1	78.51	38.57	63.6	83.89	53.27	34.82	0.8309	-0.01698
166367	516271	4	2	51.37	34.11	31.02	37.43	75.62	24.82	-0.08472	-0.1394
167139	1191211	4	2	32.45	62.87	49.21	73.69	51.88	32.43	-0.2983	0.4959

Table A.2: List of $t\bar{t}$ candidates. "nj" denotes number of tight jets, "t" number of secondary vertex tags among the tight jets.

Appendix B

Reconstruction

B.1 Calculation of the neutrino p_z solutions

The sum of the four-vectors have to be the same of that of the W-boson:

$$\mathbf{P}_e + \mathbf{P}_\nu = \mathbf{P}_W$$

Squaring this equation:

$$(\mathbf{P}_e + \mathbf{P}_\nu)^2 = M_W^2$$

With $\mathbf{P}_e^2 \equiv M_e^2 \approx 0$ and $\mathbf{P}_\nu^2 \equiv M_\nu^2 = 0$

$$2\mathbf{P}_e\mathbf{P}_\nu = M_W^2$$

$$\Longrightarrow \quad E_e E_\nu - \vec{P}_e\vec{P}_\nu = \frac{M_W^2}{2}$$

Calculating $\vec{P}_e\vec{P}_\nu$:

$$\begin{aligned}
\vec{P}_e\vec{P}_\nu &= \begin{pmatrix} P_{x,e} \\ P_{y,e} \\ P_{z,e} \end{pmatrix} \begin{pmatrix} P_{x,\nu} \\ P_{y,\nu} \\ P_{z,\nu} \end{pmatrix} \\
&= \begin{pmatrix} P_{T,e}\cos\varphi_e \\ P_{T,e}\sin\varphi_e \\ P_{z,e} \end{pmatrix} \begin{pmatrix} P_{T,\nu}\cos\varphi_\nu \\ P_{T,\nu}\cos\varphi_\nu \\ P_{z,\nu} \end{pmatrix} \\
&= (\cos\varphi_e\cos\varphi_\nu + \sin\varphi_e\sin\varphi_\nu)\, P_{T,e}P_{T,\nu} + P_{z,e}P_{z,\nu} \\
&= \cos(\Delta\varphi)P_{T,e}P_{T,\nu} + P_{z,e}P_{z,\nu}
\end{aligned}$$

This provides:

$$\begin{aligned}
E_e E_\nu &= \cos(\Delta\varphi) P_{T,e} P_{T,\nu} + Pz, e P_{z,\nu} + \frac{M_W^2}{2} \\
E_e \sqrt{P_{T,\nu}^2 + P_{z,\nu}^2} &= \underbrace{\frac{M_W^2}{2} + \cos(\Delta\varphi) P_{T,e} P_{T,\nu}}_{\mu} + P_{z,e} P_{z,\nu} \\
E_e^2 \left(P_{T,\nu}^2 + P_{z,\nu}^2\right) &= \mu^2 + 2\mu P_{z,e} P_{z,\nu} + P_{z,e}^2 P_{z,\nu}^2 \\
P_{z,\nu}^2 \left(E_e^2 - P_{z,e}^2\right) &- 2\mu P_{z,e} P_{z,\nu} + \left(E_e^2 P_{T,\nu}^2 - \mu^2\right) = 0
\end{aligned}$$

$$P_{z,\nu}^{\pm} = \frac{\mu P_{z,e}}{E_e^2 - P_{z,e}^2} \pm \sqrt{\frac{\left(\mu P_{z,e}\right)^2}{\left(E_e^2 - P_{z,e}^2\right)^2} - \frac{E_e^2 P_{T,\nu}^2 - \mu^2}{E_e^2 - P_{z,e}^2}}$$

Bibliography

[1] F. Abe *et al.*, *Phys. Rev. Lett.* **74** (1995) 2626.

[2] S. Abachi *et al.*, *Phys. Rev. Lett.* **74** (1995) 2632.

[3] S.L. Glashow, *Nucl. Phys.* **22** (1961) 579;
S. Weinberg, *Phys. Rev. Lett.* **19** (1967) 1264;
A. Salem in *Elementary Particle Theory : Relativistic Groups and Analyticity*, ed. N. Svartholm (Almquist and Wiksell, Stockholm 1968) p.367

[4] S. Eidelmann *et. al.*, *Physics Letters* **B592** (2004) 1.

[5] E. Noether, Kgl. Ges. d. Wiss. Nachrichten. Math.-phys. Klasse Göttingen (1918) S. 235

[6] P.W.Higgs, *Physics Lett.* **12** (1964) 252.

[7] M. Cacciari, *et al.*, hep-ph/0303085.
N. Kidonakis and R. Vogt, *Phys. Rev.* **D68** (2003) 114014

[8] J. H. Kühn and G. Rodrigo, *Phys. Rev. Lett.* **81** (1998) 49.

[9] F. A. Berends, K. J. F. Gaemers and R. Gastmans, *Nucl. Phys.* **B63** (1973) 381.
F. A. Berends, R. Kleiss, S. Jadach and Z. Was *Acta Phys. Polon.* **B14** (1983) 413.

[10] M. Beneke *et al.*, hep-ph/0003033.

[11] M.Kobayashi and T.Maskawa, *Prog. Theor. Phys.* **49** (1973) 652.

[12] G. L. Kane, G. A. Ladinsky and C. P. Yuan, *Phys. Rev.* **D45** (1992) 124.

[13] P. H. Garbincius, hep-ex/0406013.

[14] D .Amidei, Ed., "CDF Upgrade Technical Design Report", CDF Internal Note Number 3777

[15] D. Bortoletto *et al.*, *Nucl. Instr. and Meth. A* **386** (1997) 87.

[16] A. Sill *et al.*, *Nucl. Instr. and Meth. A* **447** (2000) 1.

[17] T. Affolder *et al.*, *Nucl. Instr. and Meth. A* **42586** (2004) 249.

[18] L. Balka *et al.*, *Nucl. Instr. and Meth. A* **267** (1988) 272.

[19] S. Bertolucci *et al.*, *Nucl. Instr. and Meth. A* **267** (1988) 301.

[20] Y. Seiya *et al.*, *Nucl. Instr. and Meth. A* **480** (2002) 524.

[21] A. Artikov *et al.*, *Nucl. Instr. and Meth. A* **538** (2005) 358

[22] M. Albrow, "CDF Run II Trigger Table and Dataset plan", CDF Internal Note Number 4718

[23] B. Ashmanskas *et al.*, *Nucl. Instr. and Meth. A* **518** (2004) 532.

[24] G. Gomez-Ceballos *et al.*, *Nucl. Instr. and Meth. A* **518** (2004) 522.

[25] W. Wagner, H. Stadie, T. Arisawa, K. Ikado, K. Maeshima, H. Wenzel and G. Veramendi, FERMILAB-CONF-02-269-E

[26] R. Brun and F. Rademakers, Proceedings AIHENP'96 Workshop, Lausanne, Sep. 1996, *Nucl. Inst. & Meth. in Phys. Res. A* **389** (1997) 81-86.

[27] W. Badgett, H. Frisch, R. St. Denis, T. Vaiciulis,"The Good Run List", CDF Internal Note Number 5613

[28] D. Acosta *et al.*, *Nucl. Instr. and Meth. A* **461** (2001) 540.

[29] D. Acosta *et al.*, *Phys. Rev. Lett.* **D71** (2005) hep-ex/0410041

[30] HERWIG 6.5, G. Corcella, I.G. Knowles, G. Marchesini, S. Moretti, K. Odagiri, P. Richardson, M.H. Seymour and B.R. Webber, *JHEP 0101:010* (2001), hep-ph/0011363, hep-ph/0210213.

[31] T.Sjöstrand,*Computer Physics Commun.* **135** (2001) 238, LU TP 00-30, hep-ph/0010017.

[32] ALPGEN, a generator for hard multiparton processes in hadronic collisions, M.L. Mangano, M. Moretti, F. Piccinini, R. Pittau, A. Polosa, *JHEP 0307:001* (2003) , hep-ph/0206293

[33] R. Brun, F. Bruyant, M. Maire, A. C. McPherson and P. Zanarini, CERN-DD/EE/84-1

[34] E. Gerchtein and M. Paulini, eConf **C0303241** (2003) TUMT005

[35] S. D'Auria *et al.*, "Run-Dependent MC Production for Summer 2004", CDF Internal Note Number 7055

[36] E. Sexton-Kennedy and P. Murat, eConf **C0303241** (2003) THJT001, physics/0306112.

[37] Evelyn J. Thomson *et al.*, "Top and Electroweak Event Classification Module for CDF Run II", CDF Internal Note Number 5947

[38] Evelyn J. Thomson *et al.*, "TopNtuple : a public analysis module for the Top Group for CDF Run II", CDF Internal Note Number 6737

[39] M. Erdmann *et al.*, Proceedings of the conference on Computing in High Energy and Nuclear Physics, (2003), IEKP-KA/2003-14, physics/0306085

[40] H1 Collaboration, internal software manual

[41] ALEPH Collaboration, ALPHA internal note ALEPH 99-087 SOFTWR 99-001

[42] F. Abe *et al.*, *Phys. Rev. Lett.* **80** (1998) 2767.

[43] E. Gamma *et al.*, "Design Patterns", Addison Wesley, ISBN 0-201-63361-2 (1994)

[44] http://www-ekp.physik.uni-karlsruhe.de/∼pax

[45] B. Stroustrup, "The C++ Programming Language", Addison Wesley, ISBN 0-201-88954-2 (1997)

[46] C. Hill, J. Incandela, and C. Mills, "Electron Identification in Offline Release 5.3", CDF Internal Note Number 7309

[47] Victoria Martin, "High pt muons, recommended cuts and efficiencies for release 5.3.1", CDF Internal Note Number 7031

[48] M. Tecchio, A. Varganov, B. Jayatilaka, D .Amidei, Y .Takeuchi, R .Tsuchiya, D .Whiteson, V .Boisvert, "Top Dilepton Cross Section Measurement using the GEN5 DIL Selection", CDF Internal Note Number 7851

[49] J-F. Arguin *et al.*, "Generic Jet Corrections for Run II data", CDF Internal Note Number 6280

[50] A. A. Bhatti, K. Hatakeyama, "Realtive jet energy corrections using missing E_T projection fraction and dijet balancing", CDF Internal Note Number 6854

[51] J-F. Arguin, B. Heinemann, "Underlying Event Corrections for Run II", CDF Internal Note Number 6239

[52] "SecVtx Optimization for the 2003 Winter Conferences", CDF Interal Note Number 6242.

[53] "Efficiency of SecVtx B-Tag Used for the 2003 Sommer Conferences", CDF Interal Note Number 6543.

[54] J. G. da Costa and S. Rappoccio, "SecVtx Tag Rate Matrices for 5.3.3_nt", CDF Internal Note Number 7326.

[55] D. Acosta *et al.*, "Introduction to Run II Jet Probability", CDF Internal Note Number 6315

[56] "Kinematic Fit Method for Top Candidates", CDF Internal Note Number 2200;
"Updated Measurement of the Top Quark Mass in the Lepton + Jets Channel", CDF Internal Note Number 6845.

[57] "Revisiting the Top-Specific Jet Energy Corrections", CDF Internal Note Number 6404.

[58] J. S. Miller, D. Amidei, "Preliminary Method 2 Backgrounds For Top Par Production in Lepton Plus Jets Events with SecVtx using 318.5 pb^{-1} of $p\bar{p}$", CDF Internal Note Number 7486.

[59] G. Unal, "$W + b\bar{b}$ and $W + c\bar{c}$ Background in the Top SVX Analysis", CDF Internal Note Number 3389.

[60] G. Unal, "Background summary for Top SVX Analysis", CDF Internal Note Number 3513.

[61] The Electroweak Muon Channel Working Group, "Measurements of W, Z, Cross Sections in the Muon Channel and Their Ratio R, Using CDF Run II Data", CDF Internal Note Number 6711.

[62] J. M. Campbell and R. K. Ellis *Phys. Rev. D* **65**, 113007 (2002).

[63] J-F. Arguin *et al.*, "Systematic Uncertainties Associated with Jet Corrections for Winter 2003 Conferences", CDF Internal Note Number 6419

[64] R. D. Peccei, S. Peris and X. Zhang *Nucl. Phys.* **B349** (1991) 305-322.

[65] V. Blobel and E. Lohrmann, "Statistische und numerische Methoden der Datenanalyse", ISBN 3-519-03243-0, B.G. Teubner

[66] F. James and M. Roos, *Comput. Phys. Commun.* **10** (1975) 343.

[67] A. Abulencia *et al.*, hep-ex/0511023.

[68] V. M. Abazov *et al.*, *Phys. Rev.* **D72** (2005) 011104

Acknowledgments

This thesis would not have been possible without the advice, help and support of many people. It is impossible to name them all. Those who are not mentioned are certainly not forgotten. Special thanks go to:

- Prof. Dr. Thomas Müller: for giving me the opportunity to do my Ph.D thesis in the field of top quark physics.
- Prof Dr. Günther Quast: for co-supervising this thesis.
- Prof. Dr. Martin Erdmann: for being a never-ending source of new ideas and inspiration. Many things would not have been started without his advice and the fruitful discussions with him.
- Dr. Wolfgang Wagner: for a lot of small as well as big hints and support essential for the achievement of this thesis.
- Dr. Jeannine Wagner: for helping to design my plots, reading very carefully this thesis and a lot of fruitful discussions.
- Joachim Heuser: for the carefully reading of my thesis and desperately trying to improve my poor English.
- Yves Kemp, Thorsten Walter,Matthias Kirsch, Adonis Papaikonomou, Jan Lück: For the harmonic atmosphere in our office as well was the numerous discussions around physics and other important things.
- EKP Admin Team: for keeping the Computer cluster running.
- All the other members and former members for the helpful and nice atmosphere.
- To the Landesgraduiertenförderung Baden-Würtemberg and the "Graduiertenkolleg Hochenergie und Teilchenastrophysik" for supporting my work by a graduate scholarship.
- To my parents and grand parents: for never objecting to my choices.
- To Isabell: for your patience, support and love.